Capillary-Driven Shape Evolution in Solid-State Micro- and Nano-Scale Systems

by

Rachel Victoria Zucker

S.B., Materials Science and Engineering
S.B., Earth, Atmospheric, and Planetary Sciences
Massachusetts Institute of Technology, 2009

Submitted to the Department of Materials Science and Engineering
in partial fulfillment of the requirements for the degree of

Doctor of Philosophy

at the

MASSACHUSETTS INSTITUTE OF TECHNOLOGY

June 2015

Author .....
Department of Materials Science and Engineering
April 13, 2015

Certified by .....
W. Craig Carter
POSCO Professor of Materials Science and Engineering
Thesis Supervisor

Certified by .....
Carl V. Thompson
Stavros Salapatas Professor of Materials Science and Engineering
Thesis Supervisor

Accepted by .....
Donald R. Sadoway
Chair, Department Committee on Graduate Students

Capillary-Driven Shape Evolution in Solid-State Micro- and Nano-Scale Systems

by

Rachel Victoria Zucker

Submitted to the Department of Materials Science and Engineering
on April 13, 2015, in partial fulfillment of the
requirements for the degree of
Doctor of Philosophy

Abstract

Thin films are the fundamental building blocks of many micro- and nano-scale devices. However, their high surface-area-to-volume ratio makes them unstable due to excess surface free energy. Capillarity drives a process known as dewetting, during which holes form, the film edges retract, and a thickened rim of material accumulates at the edges. Various shape instabilities can occur on the film edge, resulting in complicated morphologies and break-up of the film into isolated particles. Dewetting occurs in the solid state by surface self-diffusion.

In this work, a variety of models are presented to gain insights into the mechanisms that control the shape evolution of thin films. A combination of thermodynamic study, stability analyses, analytical models, explicit interface-tracking simulations, and phase-field simulations reveal the underlying driving forces and mass flows, explain observed morphologies and instabilities, and offer insights into how to manipulate the final structure. These pathways to control dewetting are applicable in two areas: to design micro- and nano-scale devices that are resistant to thermal degradation, and to use dewetting as a new patterning method to generate stable, complex, small-scale geometries.

Thesis Supervisor: W. Craig Carter
Title: POSCO Professor of Materials Science and Engineering

Thesis Supervisor: Carl V. Thompson
Title: Stavros Salapatas Professor of Materials Science and Engineering

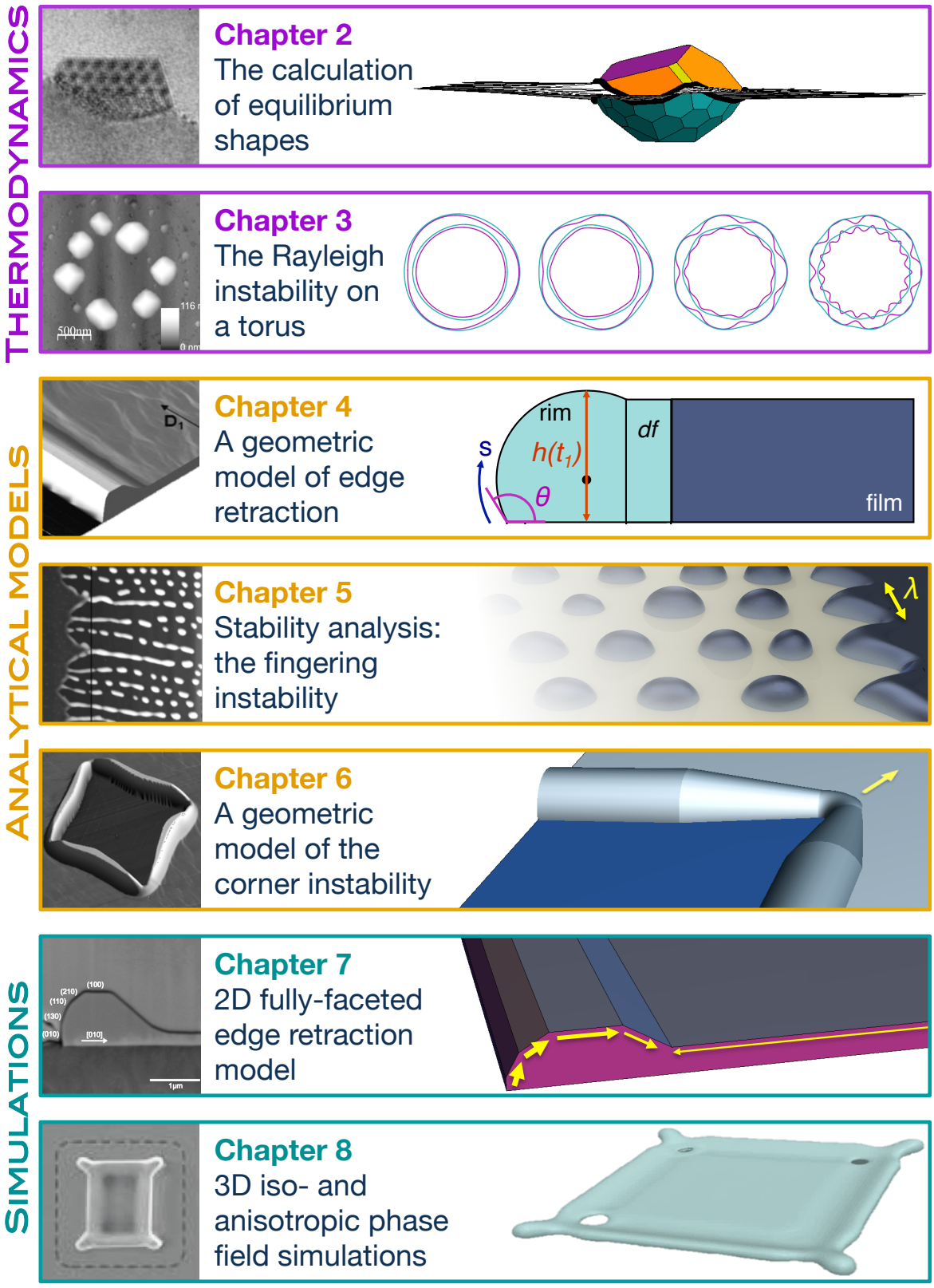

Figure 0-1: The structure of this thesis is illustrated. The experimental images at the left of each box are from references [22, 1, 89, 47, 95, 34, 90].

Extended Abstract

Excess free surface energy exerts a driving force on materials known as capillarity. If transport mechanisms are active, solids can undergo shape changes to minimize their surface energy. Surface diffusion is usually the fastest capillary-driven kinetic mechanism in solids.

Substrate-supported thin films are the basic components of most micro- and nano-scale devices. However, their high surface-area-to-volume ratios equate to large capillary forces. Shape evolution by capillary-driven surface diffusion in thin films is known as "dewetting." Dewetting is a well-known thermal degradation mechanism, but it is also gaining popularity as a patterning method.

Dewetting microstructures are distinctive, characterized by holes forming in the film, retracting edges, and a rim of material accumulating at the edges. The film undergoes either periodic pinch-off, which deposits strips of material that further break up due to a Rayleigh instability, or a shape instability, which leads to cellular or dendritic morphologies that ultimately break up into isolated particles. Prior to this work, only the simplest two shape evolution modes were understood: periodic pinch-off in isotropic materials [75, 85], and the Rayleigh instability for isotropic materials [67, 49].

In this thesis, the shape evolution modes that determine dewetting microstructures are explained and characterized. It is organized by the techniques used, which are (1) classical, thermodynamic approaches, (2) analytical models of dewetting that rely on geometric simplifications, and (3) simulations that attempt to capture the full phenomenology. The sub-structure of this work is described in more detail below, and visualized in the graphical abstract, Figure 0-1.

1. **Thermodynamics**

   The calculation and display of equilibrium shapes

   The equilibrium geometry of the thin film/substrate system is the end-state of dewetting. There are two constructions available to compute equilibrium geometries: the Wulff construction for isolated particles, and the Winterbottom construction for particles attached to a rigid substrate. However, these are tedious to execute. In Chapter 2, a fast, user-friendly, open-source software tool is

introduced to calculate and display equilibrium shapes. A new algorithm was developed to accelerate the computation. In addition, a new convexification method, the "double-Winterbottom" construction, is introduced to calculate the equilibrium geometry of a particle when the substrate mobility is not zero, as is often the case. This new class of equilibrium geometry is studied, and the double-Winterbottom method is implemented within the software tool. This work was published in the *Journal of Materials Science* [94].

The Rayleigh instability on a torus

The Rayleigh instability refers to the surface energy minimization-drive break-up of a cylinder of material into isolated particles. The Rayleigh instability also acts during dewetting, assisting in the break-up of strips of material. However, the strips generated by dewetting are not always straight. In Chapter 3, an exact treatment of the Rayleigh instability on a curved strip of material, *i.e.*, a torus, is provided. The curvature is found to have a stabilizing effect. The strip's radius of curvature must be at least four times greater than its cross-sectional radius to undergo a Rayleigh instability. When the strip evolves by surface diffusion, long-wavelength perturbations decay, in contrast to the result for a straight cylinder. A torus is found to be susceptible to an additional mode of instability, the "shrinking" instability, in which the in-plane radius decreases uniformly to reach a spherical morphology without breaking apart. The two instabilities may act simultaneously, and which one happens first depends on the aspect ratio of the torus.

2. Analytical models

A geometric model of edge retraction

The distance a film edge has retracted with time is usually fitted to a power law. However, recent numerical simulations [85, 96] have suggested that edge retraction does not follow a power-law. In Chapter 4, a simple, geometric model of edge retraction is presented that reproduces the simulation time scalings analytically. The model shows that initially, retraction is linear with time, and at late times, it approaches a power-law with $t^{2/5}$ scaling. The transition time from linear to $2/5$

power-law scaling is calculated as a function of contact angle. The time scalings are explained by the shape of the rim in the short and long time limits, and this model describes isotropic and anisotropic films equally well.

Stability analysis: the fingering instability

The edges of retracting thin films often undergo a shape instability. An initially-straight edge can develop finger-like projections and deposit a trail of particles behind each finger as it retracts. The "fingering instability" presents a simple means for producing nanoparticle arrays, but the cause of the instability and the factors that determine the finger spacing are unknown. In Chapter 5, a linear stability analysis on the film edge reveals the underlying cause of the instability. It is driven not by a Rayleigh-like or Mullins-Sekerka-like instability, as previously thought, but by the "divergent retraction" instability: fluctuations in rim height lead to varying retraction rates along the film edge, which grow into fingers. The analysis predicts that perturbations must have a sufficiently-large wavelength to lead to instability, and arbitrarily-long wavelength perturbations can grow. Therefore, a wide range of finger spacings are possible.

A model of the corner instability

If a film is patterned with a pre-existing polygonal hole, or if the film is anisotropic and holes are naturally polygonal, an additional shape instability is possible. The corners of holes are known to retract with constant velocity, while the edges retract at a decreasing rate [18]. This results in star-shaped holes, often with a dendritic morphology. In Chapter 6, the underlying cause of the "corner instability" is revealed using a geometric model of retraction on polygonal holes. The perimeter increase of the hole occurs entirely at the corners, and the need to lengthen the rim consumes the volume that would otherwise go into building the rim height. The rim at the corner tip reaches a stable equilibrium height, while the edges of the hole retract as usual, without interacting with the corner. The corner and edge rim height and retraction distances predicted by this simple model agree well with experiments.

3. Simulations

A 2D model of fully-faceted edge retraction

The profile of a retracting film edge has been modeled and studied before for isotropic [75, 85] and weakly-anisotropic [27] materials. In these cases, the film edge develops a thickening rim, followed by a thinning valley. However, experiments show that strongly-anisotropic materials do not have a valley. In Chapter 7, a model is introduced to simulate fully-faceted edge retraction. Simulations reproduce the observation that there is no valley, but visualizing the mass flows reveals slow thinning of the entire film, suggesting that the bulk of the film acts as a valley. The simulations also show that diffusivity anisotropy plays a dominant role in determining the rate of edge retraction. This work was published in *Comptes Redus Physique* [96].

A phase field simulation method for dewetting

The intermediate geometries during dewetting are usually quite complicated. Up until now, no method has been available that can simulate dewetting in 3D in a reasonable amount of time. In Chapter 8, a phase field model of dewetting, for arbitrary anisotropy, is developed and demonstrated. The phase field approach easily handles topological changes (such as hole formation and pinch-off), and the corresponding code is a finite element method including parallelization, time adaptivity, adaptive grids, implicit stabilizing terms, and a regularization scheme for handling strong anisotropy. The boundary conditions in the case of anisotropy are presented and implemented. Several test cases are shown in two and three dimensions with isotropic, weakly-anisotropic, and strongly-anisotropic surface properties.

There are five mechanisms of film break-up during dewetting: hole formation, edge retraction and pinch-off, the fingering instability, the Rayleigh instability, and the corner instability. This document contains significant advances in the understanding of four of these mechanisms (the exception is hole formation, which cannot be explained by capillarity alone [55]). Future work includes testing the predictions of a linear edge retraction rate at early times, the

wavelength dependance for fingering and Rayleigh instabilities, and the equilibrium corner height following a corner instability, with experiments and phase field simulations.

Acknowledgments

This thesis was made possible by the commitment and generosity of countless people. Here, I wish to thank a few that have made a particularly large difference towards the occasion of completing this document, and the chapter of my life that accompanies it.

My mentor, Craig Carter, has shaped who I am as a scientist, and as a person. While I have yet to produce any work that meets his standards, they have become my standards too, and it gives me something to aspire to. Contrary to my expectations, this impossibly high bar is a source of joy, inspiration, and freshness, and it will keep me learning and growing for the rest of my life. I cannot recall doing any research with Craig, but I have nevertheless enjoyed our blunderous search for beauty in the natural world. His careful guidance has been one of the finest gifts I have ever received. I will always be indebted to him.

Carl Thompson led me to a problem that I love. His enthusiasm for discovery is infectious and absolutely delightful. To me, Carl is the quintessential materials scientist, and support from such a giant in the field gives me confidence and pride in my work. I am extremely grateful to Carl for his guidance and support.

I am indebted to Chris Schuh for his relentless encouragement. He has always pushed me to aim higher and think big. I believe in myself as much as I do now because of Chris. I also thank Jeff Grossman, who has been incredibly supportive throughout my graduate work. I am privileged to benefit from his thoughtful guidance and advice.

I have had the good fortune to find some truly exceptional collaborators. Dominique Chatain, Serge Hagege, and Uli Dahmen had a major impact on the direction of my work, and contributed to the chapter on equilibrium shapes. Alan Gye-Hyun Kim did an astonishing amount of experimental work on dewetting, and his findings underpin many of the discussions in this document. He played a particularly large role in the chapter on the corner instability. Rainer Backofen, Marco Salvalaglio, Roberto Bergamaschini, Francesco Montalentini, and Axel Voigt put in an immense amount of work in the development of the phase field code and donated many hours of computation time, and Chapter 8 would not have been possible without them. It has been, and will continue to be, a pleasure to work with these fine people.

I also owe thanks to Tim Grove, who was my first mentor at MIT. His ratty t-shirts

shattered my stereotypes of professors, and he had the patience to show an 18-year-old kid what a privilege and joy it is to be a scientist. He started me on a path that has brought me a lot of joy.

The people at PICS, and more broadly in MACAN, have become my academic community, and my friends. I draw inspiration from the discussions I have had with everyone in this amazing group. Wanting to stay a part of that academic family is the strongest draw for me to stay in science.

Germany became my second home while I was a graduate student. I am grateful to Tina and Gerhard for hosting me, and to everyone in the group for making me feel welcome. I am especially thankful for Alex, for his generosity with his time, for his boundless patience to discuss and review my work, and for making me a better, more whole person.

MIT is my spiritual home. It buzzes and hums with the spastic movements of robots and nerds, and simultaneously feels like a temple, full of monks silently, patiently searching for nirvana. MIT is a state of mind, and while it is not customary to thank ideas, I can thank some of the people that made it much more palatable. Many faculty in the materials science and EAPS departments had a big impact on me, academically and personally, and I thank each and every one of my instructors for their time and efforts. The DMSE office - namely because of Angelita Mireles, Elissa Haverty, and Amy Shea - is my happy place on campus, and I am so grateful to them for always taking care of me. Kathy Fitzgerald, Jennifer Patten, and Maria Tsafoulias were incredibly generous in offering administrative support, and I am so glad their doors were always open. My friends Alan, Matt, David, Nancy, Sema, Tim, Claudia, Wenhao, Billy, Deepak, Red, Chelsea, Jennie, Andi, Olivia, Christian, David, Alison, Adrianne, Noah, Chris, Sam, and Randy always made everything better, and carried me through it all. And to say that Becky is a rock in troubled water in an understatement. She is a metric by which all others can measure their sanity, and always a source of comfort.

David Paul is a true Mensch, and I mean that in the rarest and noblest sense. His sense of humor is contagious, and he has become one of my dearest and most valued friends. My time as a graduate student would be hollow without our weekly lunches.

Finally, what would I be without my family. The Zuckers offer some of the finest academic

training around. Surviving a dinner conversation with that lot is intellectual jiu-jitzu. In stark contrast, my mother taught me how to think deeply, slowly, and carefully. I cannot thank her enough for sharing this dying art, and for always, always being on my side. My father is my longest-serving teacher. He taught me the scientific method with his gentle guidance and endless patience for the question "dad, why...?" Aaron is my sparring partner, and the only person that can reliably make me laugh so hard I cry. Lisa has a staggering social intelligence and insightfulness that I am only just beginning to learn from, and Joe has taught me all I know about ethics. I love you all, and my huge, ridiculous family is my most prized “possession.” I count my lucky stars every day, and every person in my family is one of them.

Contents

List of Figures

List of Tables

Chapter 1

Introduction

1.1 The capillary force

Surface tension, or capillarity, is familiar when dealing with liquids. The capillary force holds drops of liquid together, creates the meniscus line in a container, and is responsible for "capillary action;" that is, the ability of a liquid to climb up a narrow channel, even in opposition to external forces like gravity. Capillarity acts on solids as well. At macroscopic length scales, there are few visible effects of surface tension in solids. However, at the micro- and nano-scales, capillarity can be the largest driving force acting on a system and dominate its dynamics.

Capillarity is chemical in origin. It can be explained two ways: either as a pressure, or as an excess free energy. As a pressure, it originates from the attractive bonds between atoms or molecules in a condensed phase. For example, water molecules interact via hydrogen bonds, which holds a water or ice droplet together. The water molecules in the center have neighboring molecules in all directions, so the net force is zero. However, the water molecules on the surface only have neighbors on one side, generating a pressure that compresses the droplet. As an energy, it originates from the unsatisfied bonds of the surface molecules. For example, consider a material that has minimum energy when it has twelve nearest-neighbors, such as an FCC crystal. At the surface, only six nearest-neighbor bonds are possible. The six remaining unsatisfied bonds increase the free energy of the surface atom. Therefore, one might expect the surface energy density of this material to be six times

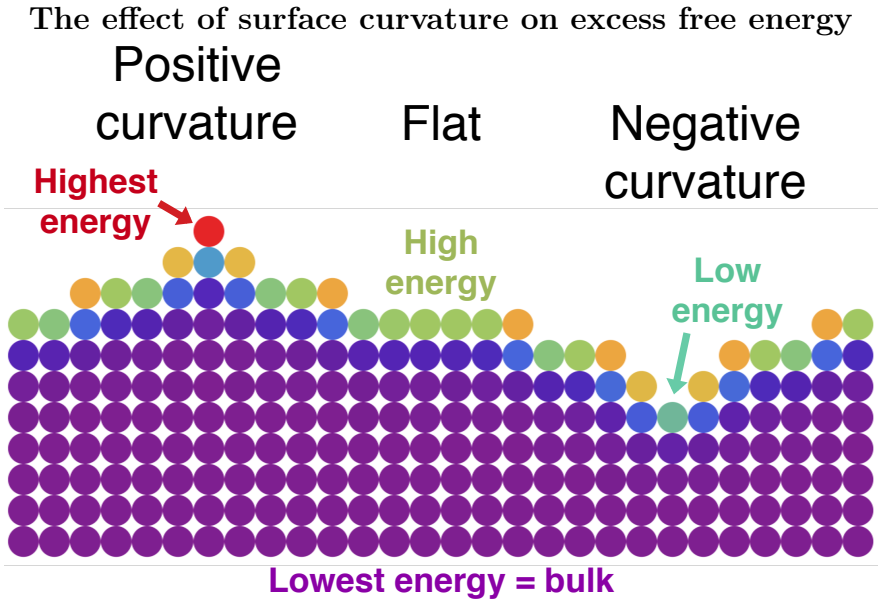

Figure 1-1: A schematic shows the effect of curvature on excess surface free energy. Atoms are shaded by their energy, using a Lennard-Jones pair potential. An atom in the bulk of this material has 8 bonds. An atom at the surface has less than 8 bonds, but the number depends on the surface curvature.

the bond energy, divided by the surface area per atom (the square of the bond length). This bond-breaking estimation of the surface energy density is crude, but it gives a decent approximation (*e.g.*, [81]).

1.2 Thermodynamics of Interfaces

The bond-breaking explanation of capillarity is useful for understanding its dependance on surface curvature. If a normally 8-coordinated material is cut along a plane, the average number of unsatisfied bonds is exactly 3, as shown in Figure 1-1. However, if the surface of the material is corrugated, the average number of unsatisfied bonds varies. For an atom sitting on top of a hill, there are more than 3 unsatisfied bonds. For an atom sitting in a valley, the number of unsatisfied bonds is less than 3.

Consider the change in energy of the system in Figure 1-1 upon adding an atom to the surface. The change in energy will depend on where the atom is placed. If the change in energy upon adding an atom to an infinite, flat surface is defined to be zero, then the energy will increase if the atom is placed on top of a hill, and decrease if it is placed in a valley. This

is the reason that the chemical potential of a surface is proportional to the mean curvature, K. For capillarity, the chemical potential along a surface, μ, relative to an infinite, flat surface, is [32]

$$\mu = \gamma K \Omega, \tag{1.1}$$

where γ is the surface energy density of the material, and Ω is the atomic volume. Because a pure material is being considered, the chemical potential refers to single species and μ can be related to the local vapor pressure. The mean curvature K is a geometric property defined as $K = 1/2(K_1 + K_2)$, where K_1 and K_2 are the principal curvatures of the surface. If r_1 and r_2 are the principal radii of curvature on the surface, then $K = 1/2(1/r_1 + 1/r_2)$. Mean curvature is a measure of how quickly the surface area A changes if the interface moves and sweeps through some volume V: $K = dA/dV$.

The total energy of an interface is $\int_A \gamma dA$, where A is the total interfacial area, dA is a surface element, and γ is the surface energy density of the material. In the isotropic case, γ is independent of the surface orientation, so it can be moved outside the integral, and the total energy is γA. If the material is anisotropic, γ is a function of surface orientation, and must remain inside the integrand.

Anisotropic materials have a surface energy density that depends on the interface orientation, $\gamma(\boldsymbol{n})$, where $\boldsymbol{n}$ is the surface normal. In the extreme case of a fully-faceted material, the isotropic definition of chemical potential becomes meaningless because the facets have zero mean curvature, except at the corners, where the mean curvature is undefined. The chemical potential is instead written in terms of the more general weighted mean curvature, or WMC, κ^γ [77]:

$$\mu = \kappa^\gamma \Omega. \tag{1.2}$$

The physical meaning of chemical potential can be used to obtain an expression for WMC. The chemical potential for a pure material is the change in total energy upon the addition of material, dE/dN, where N is the number of atoms. dE/dN is equal to $\Omega\, dE/dV$. Figure 1-2 shows dE/dV for three cases of a fully-faceted geometry. The additional volume is shaded light blue, and the change in length of facets on the shape are highlighted. The change in total surface energy, divided by the volume added, is the WMC, dE/dV.

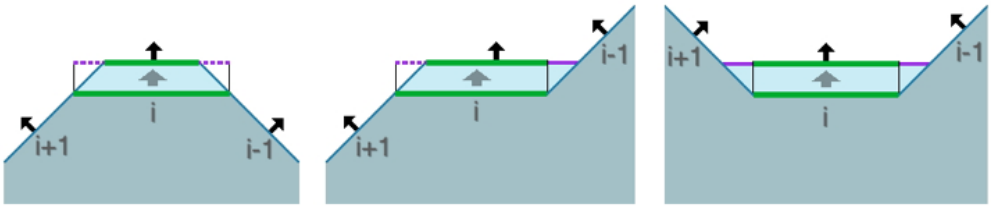

Figure 1-2: The change in length caused by moving a facet outwards along its normal, for three types of facet. Facets are labeled in gray, and their normal vectors are drawn in black. (a) A regular facet, which has positive WMC (weighted-mean curvature) and $\sigma = 1$. Outward motion causes the total length of the facet to decrease. (b) A neutral facet, with zero WMC and $\sigma = 0$. Outward motion causes no net change in the length of the facet. (c) An inverse facet, which has negative WMC and $\sigma = -1$. Outward motion causes the total length of the facet to increase. (Figure after [77].)

In the isotropic limit, WMC reduces to the surface energy times mean curvature, γK. For fully-faceted 2D geometries, it can be shown that the WMC of the i^{th} facet on a polygon is [77]

$$\kappa_i^{\gamma} = \frac{\sigma \Lambda_i}{L_i} \tag{1.3}$$

where σ_i is 1 if the facet is regular, 0 if the facet is neutral, and -1 if the facet is inverse (see Figure 1-2 for explanations of regular, neutral, and inverse), L_i is the length of the facet, and Λ_i is a geometric factor, given by

$$\Lambda_i = \frac{\gamma_{i+1} - \boldsymbol{n}_i \cdot \boldsymbol{n}_{i+1}\gamma_i}{\sqrt{1 - (\boldsymbol{n}_i \cdot \boldsymbol{n}_{i+1})^2}} + \frac{\gamma_{i-1} - \boldsymbol{n}_i \cdot \boldsymbol{n}_{i-1}\gamma_i}{\sqrt{1 - (\boldsymbol{n}_i \cdot \boldsymbol{n}_{i-1})^2}}, \tag{1.4}$$

where $i+1$ indicates the next facet, $i-1$ is the previous facet, and $\boldsymbol{n}_i$ is the normal vector of the facet [77]. This expression can be calculated from Figure 1-2. The geometric factor is also identical to the length of the facet with the same orientation on the equilibrium shape [77].

1.3 Equilibirum shapes

1.3.1 Isolated particles: the Wulff construction

When the only contribution to excess free energy is interfacial energy and the volume is fixed, the equilibrium shape of an isolated particle in a homogeneous environment is the Wulff

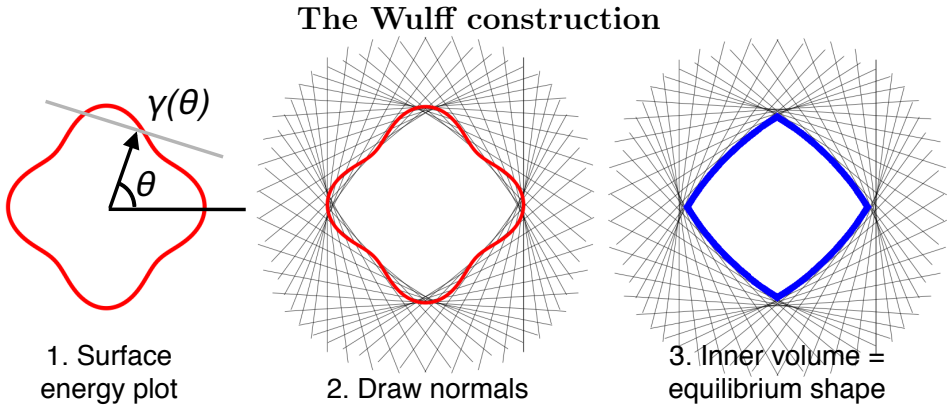

Figure 1-3: The Wulff construction is demonstrated for a two-dimensional material. The Wulff construction begins with a plot of $\boldsymbol{n}\,\gamma(\boldsymbol{n})$ for all $\boldsymbol{n}$ on the unit sphere, where $\boldsymbol{n}$ is the normal vector to a surface, and $\gamma(\boldsymbol{n})$ is the interfacial energy of that surface. For all orientations, a plane perpendicular to $\boldsymbol{n}$ is drawn a distance $\gamma(\boldsymbol{n})$ from the origin. All points on the far side of the plane are discarded. The remaining volume is the equilibrium shape, or Wulff shape.

shape [86]. For isotropic materials, the Wulff shape is a sphere because this minimizes the total area. For anisotropic materials, there is a competition between two effects: a sphere has the minimum area, but a polyhedron with facets corresponding to the lowest energy orientations avoids the higher energy orientations. The equilibrium shape is a compromise between these two extremes.

The equilibrium shape can be found using the Wulff construction [86] (Figure 1-3). The Wulff construction is performed on the interfacial energy density $\overrightarrow{\gamma}(\hat{n}) \equiv |\overrightarrow{\gamma}(\hat{n})|\hat{n} = \hat{n}\gamma(\hat{n})$, where $\overrightarrow{\gamma}$ is a vector function of all possible interface orientations $\hat{n}$ and $\gamma(\hat{n})$ (*n.b.*, with no vector notation) is the magnitude of $\overrightarrow{\gamma}$ in the direction $\hat{n}$. An orientation, $\hat{n}$, may not be a stable interface orientation: stability is determined by whether it is removed by the Wulff construction.

To generate the Wulff shape, one begins with the plot of $\hat{n}\gamma(\hat{n})$. For each orientation $\hat{n}_i$, a plane perpendicular to $\hat{n}\gamma(\hat{n})$ is drawn. This perpendicular plane divides space, and all points on the far side of the plane are discarded. After this exclusion procedure is repeated for all orientations, the remaining volume is the Wulff shape, $\mathcal{W}$. The Wulff construction can be stated concisely as $\mathcal{W} = \{\overrightarrow{p} \in \gamma\text{-space} | \overrightarrow{p} \cdot \hat{n} \leq \gamma(\hat{n})\}$, where $\overrightarrow{p}$ are points in $\mathcal{W}$-space. Because the shapes in γ-space (*i.e.*, the space in which the γ-plot is drawn—where coordinates have units of energy/area) and real space are the same, the Wulff construction

can be written in real space as $\mathcal{W} = \{\overrightarrow{x} \in \Re^3 | \overrightarrow{p} \cdot \hat{n} \leq \gamma(\hat{n})\}$ with an additional constraint on the particle's volume $V_{\text{particle}} = \int d^3\overrightarrow{x}$. The Wulff shape is always convex, and if facets are present, all facets have $\sigma = 1$. The chemical potential is uniform at equilibrium, so WMC is constant on the Wulff shape.

There is an analogy between unstable interfacial orientations and the unstable chemical compositions in a miscibility gap [10]. The Wulff construction is a convexification of $\hat{n}\gamma(\hat{n})$ ($|\hat{n}| = 1$) which results in the removal of unstable orientations from the final shape, just as the common-tangent construction is a convexification of the molar free energy $G(X_1, X_2, \ldots X_n)$ ($X_1 + X_2 + \ldots X_n = 1$) which removes unstable compositions from the phase diagram. When a material phase separates into two distinct compositions, it does so because a mixture of the two phases has lower energy than the original composition. When an orientation separates into a collection of two or more orientations, *e.g.* sharp "hills-and-valleys" or "pyramids", it does so because the total energy per projected surface area is less than that of the orientation. Such unstable orientations do not appear on the Wulff shape—they disband into $\mathcal{W}$-edges for "hill-and-valley" morphologies, and disband into $\mathcal{W}$-corners for pyramid morphologies.

To continue the analogy to phase diagrams, the familiar phase-diagram is a representation of the stable compositions $(X_1, X_2, \ldots, X_N)$, and $\mathcal{W}$ is the orientation-diagram for a physical, tangible, shape [12]. When $\hat{n}\gamma(\hat{n})$ has sufficiently strong anisotropy, $\mathcal{W}$ is composed of planar facets, which are analogous to line-compounds. Whereas line-compounds occur at special stoichiometries, the facets appear at all crystallographically-equivalent special orientations. Smooth or partially-faceted $\mathcal{W}$ occur for weaker anisotropy; these also have phase diagram analogies.

1.3.2 Particles Attached to a Planar Substrate: The Winterbottom Construction

The Wulff construction only applies to isolated particles in homogeneous environments. However, in many contexts of practical importance (*e.g.*, solid-state dewetting, catalysis, micropatterned surfaces, pores in a sintered body), a particle can be attached to one or more interfaces. The equilibrium shape must minimize the sum of each total interfacial

energy while maintaining other constraints, such as particle volume and connectivity of the interfaces. The simplest example is a deformable particle with a fixed volume that abuts a non-deformable (rigid) planar interface (*e.g.*, a liquid drop on an inert solid planar surface). In addition to the interfacial energy between the particle and its environment in the absence of the substrate (γ_{PV}, where V refers to the environment, which is often a vapor phase), there are two additional interfacial energies: the interface where the substrate abuts the particle (γ_{SP}) and where the substrate is not in contact with the particle (γ_{SV}). The isotropic particle case is familiar: minimization produces a spherical cap that intersects the substrate with a uniform wetting angle, θ, for the particle on the substrate, with

$$\theta = \cos^{-1} \frac{\gamma_{SV} - \gamma_{SP}}{\gamma_{PV}}. \tag{1.5}$$

Equation 1.5 is known as the Young equation, and can be interpreted as a force balance or as a boundary condition that derives from global energy minimization—these interpretations are not independent [14]. The Young Equation is independent of particle size (in the absence of other defect energies), but the curvature of the spherical cap is determined by the particle volume. Considering the geometry of the shape in $\mathcal{W}$-space, the center of the spherical gamma surface for the particle/exterior interface (with radius γ_{PV}) sits a distance $(\gamma_{SV} - \gamma_{SP})$ above the substrate. If $(\gamma_{SV} - \gamma_{SP})$ is negative, then most of the sphere is discarded, and only a small cap remains. This is the Winterbottom construction for an isotropic particle [83].

The Young equation is helpful in determining the equilibrium shape of an isotropic particle, but it is not obvious how it pertains to a general anisotropic particle. Winterbottom showed that the $\gamma = 0$ point will be a distance $(\gamma_{SV} - \gamma_{SP})$ above the substrate not only for isotropic particles, but for a particle with a general Wulff shape [83]. Additionally, the selection of the $\gamma = 0$ point is known to be arbitrary [46]. An example of the Winterbottom construction with various $(\gamma_{SV} - \gamma_{SP})$ values is shown in Figure 1-4. The case when $(\gamma_{SV} - \gamma_{SP})$ is positive is often referred to as "bad wetting," while the case when $(\gamma_{SV} - \gamma_{SP})$ is negative is "good wetting" [41].

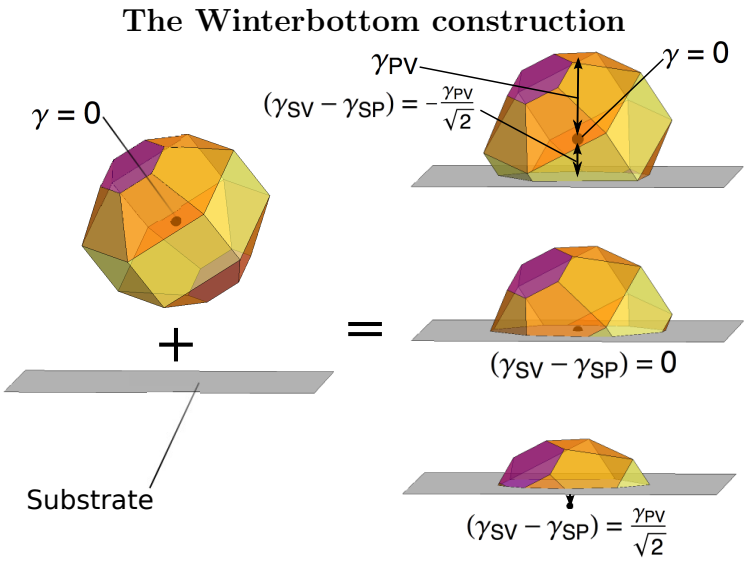

Figure 1-4: Left: the Winterbottom construction begins with the Wulff shape of a particle and $(\gamma_{SV} - \gamma_{SP})$. Right: the distance between the $\gamma = 0$ point in the Wulff shape and the substrate surface is equal to $(\gamma_{SV} - \gamma_{SP})$. Top: the equivalent wetting angle, θ, is 135°. Middle: 90°. Bottom: 45°.

1.4 Capillarity far from equilibrium

For a body of material that is not in the equilibrium shape, there will be a difference in chemical potential across its surface. If a kinetic mechanism is available, the gradient in chemical potential will drive mass to flow from high to low WMC positions. The shape will evolve towards the equilibrium shape by a pathway determined by the fastest kinetic process available.

It is necessary to identify the dominant (fastest) transport mechanism to describe the shape evolution. In a solid, there are four possible kinetic pathways: volume diffusion, surface diffusion, evaporation-condensation, and viscous flow. All of these are thermally-activated, so shape changes due to capillarity are measurable only at homologous temperatures above about 0.5 [32]. Herring showed that capillarity does not drive viscous flow in crystalline materials, so viscous flow can be eliminated (though it is possible in amorphous materials) [33]. For most materials, surface diffusion is orders of magnitude faster than volume diffusion, so volume diffusion can be eliminated as well. Finally, Mullins calculated that surface diffusion dominates over evaporation-condensation for crystalline materials with moderate or low vapor pressures [54]. This prediction has been verified experimentally, as the kinetics

of capillary-driven shape changes in crystalline materials which do not evaporate away over the course of annealing are consistent only with surface diffusion [78].

In the rare case that evaporation-condensation is the dominant mechanism, the mathematical description is much simpler than for surface diffusion, and it can be studied fairly easily [54, 15]. However, the simpler mathematics means that the morphological evolution is simple as well [15]. The rich morphological variety resulting from motion by surface diffusion (discussed in Section 1.4.3) makes it a much more exciting topic for investigation.

1.4.1 The kinetics of capillary-driven surface diffusion

To describe the motion of a two-dimensional surface, the arc length s is used to define the position on the surface. The normal vector, $\boldsymbol{n}(s,t)$, gives the orientation of the surface as a function of position and time. By convention, the normal vector points outwards, away from the material. The speed of outward motion of the interface parallel to the surface normal, V_n, as a function of time and position, gives the complete evolution.

Mullins developed an expression for $V_n(s,t)$ for isotropic materials undergoing capillary-driven surface diffusion [54]. His derivation began with the chemical potential ($\mu(s,t) = K(s,t)\gamma\Omega$), discussed in Section 1.2. The flux of surface atoms in response to curvature gradients is given by Fick's first law:

$$J(s,t) = -\frac{D_s \nu}{kT} \nabla_s \mu(s,t) = -\frac{D_s \gamma \Omega \nu}{kT} \nabla_s K(s,t), \tag{1.6}$$

where D_s is the surface self-diffusivity, ν is the surface concentration of mobile atoms, k is Boltzmann's constant, T is temperature, and ∇_s is the Laplace-Beltrami operator, *i.e.*, the gradient operator restricted to the surface profile [54]. Physically, Fick's first law states that when a gradient in potential is present, material tends to flow down that gradient to lower the total energy.

If the flux is locally divergent, then mass is leaving that location and the surface height is decreasing. Likewise, if the flux is convergent, the surface height is increasing, and it has a positive velocity along its normal. Thus, the surface velocity along its normal, $V_n(s,t)$, is

minus the divergence of the flux:

$$V_n(s,t) = \frac{D_s \gamma \Omega^2 \nu}{kT} \nabla_s^2 K(s,t), \tag{1.7}$$

where the extra factor of Ω is included to convert the units to a velocity [54]. This governing equation can be generalized to include anisotropy [93, 15]. The result is much less readable, but the derivation is the same.

The material constants in Equation 1.7 can be collected into a single material property, $B = (D_s \gamma \Omega^2 \nu)/(kT)$. The governing equation can be non-dimensionalized using B (units of length^4/time) and a characteristic length scale L:

$$v_n(s,t) = \nabla_s^2 \kappa(s,t), \tag{1.8}$$

where v_n is the dimensionless normal velocity, $v_n = V_n L^4/B$, and κ is the dimensionless mean curvature, $\kappa = KL$.

1.4.2 Thin films

Although capillary forces affect material of all shapes and sizes, in this work, special attention is given to solid thin films. This is for two reasons: first, thin films are the basic building blocks of most micro- and nano-scale devices, so they are of technological relevance, and second, thin films have large aspect ratios (width/thickness), so they are especially unstable with respect to capillarity. Large aspect ratios mean large surface-area-to-volume ratios, so the excess surface energy is high, thus the capillary driving forces are high.

We define a "thin film" as any material body supported by a substrate with a characteristic thickness L. The shape of the thin film in the plane of the substrate may be simple or quite complicated, *e.g.* as a result of patterning with lithography. The presence of the substrate has a profound effect on the shape evolution because it provides an additional constraint (*i.e.*, maintaining contact with the substrate).

The process of capillary-driven shape evolution in thin films is called "dewetting." The end state of dewetting is an array of isolated particles, each having the equilibrium shape. De-

pending on the materials and starting geometry, the particles may be randomly-distributed, or ordered. Nanoparticle and quantum dot arrays are in demand for a variety of applications, and dewetting provides a simple method to make them. Dewetting has been used to generate particle arrays for optical and magnetic devices [3, 65], sensors [50, 3], catalysis [19, 64, 57], nanowire growth [70, 21, 92, 20], and memory devices [17, 65]. These applications motivate investigations to understand how to control the particle arrangements produced by dewetting.

The intermediate stages of dewetting include a huge variety of morphologies. An example of incomplete dewetting is reproduced from Ye *et al.* [90] in Figure 1-5. When anisotropic films are patterned via lithography and then dewetted, reproducible, complex structures with sub-lithographic feature sizes are produced. Possible features include isolated particles, wire-like lines of material, which may be interconnected, and unaffected film. Devices with components made by partial dewetting should be much more thermally stable than equivalent devices made by conventional methods. This is because the components are already partially equilibrated, so the driving force for motion is dramatically lower.

1.4.3 Dewetting phenomenology

Dewetting is a well-known phenomenon, and it has been studied extensively [78]. Dewetting has four main morphological features: edge retraction, the growth of rims, hole formation, and break-up into islands of material.

Dewetting is mostly localized at film edges. This is because the gradients in surface curvature, and therefore driving forces, are largest near the edge. Edges bound the as-deposited film, or they can be the result of post-deposition patterning, or they can form spontaneously when a film is heated and holes form by natural processes. As an example of the latter, grain boundary grooves in polycrystalline films can extend through the entire thickness of the film and nucleate holes [38, 74].

Once edges are present, they will retract to reduce the film's surface area. Retraction is facilitated by a mass flux from the receding triple line (the intersection of the film/vapor, vapor/substrate, and substrate/film interfaces) to the advancing side of the rim [96]. An edge with an initially-square profile will evolve toward a shape with uniform WMC and

Experiments showing incomplete dewetting morphologies

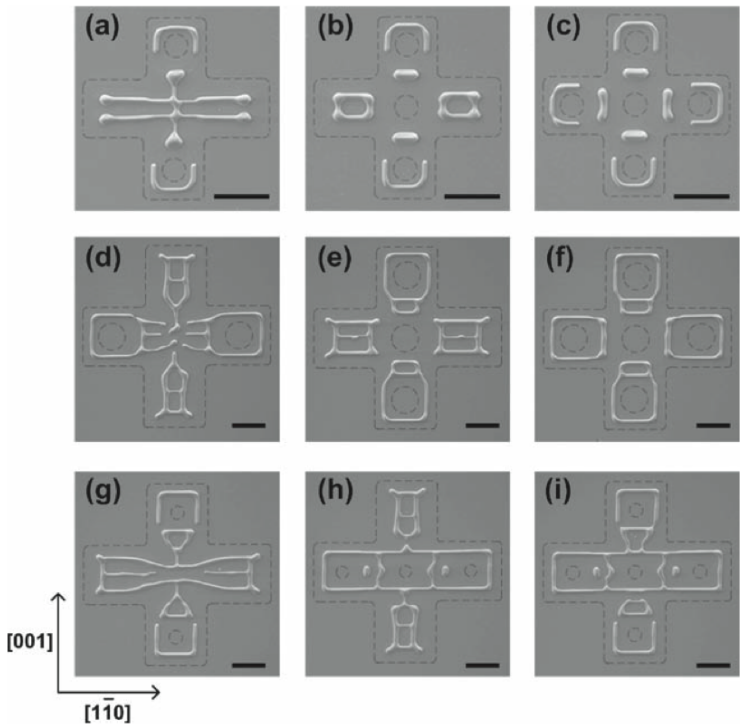

Figure 1-5: This figure shows a variety of starting geometries (dashed lines) and the corresponding incomplete dewetting morphology. This image is reproduced from Ye *et al.* [90]. The view is top-down, dark gray is the substrate, and light gray is the film material. Each subfigure corresponds to a unique starting condition, and the resulting film pattern is reproducible. The black scale bar is 10 micrometers.

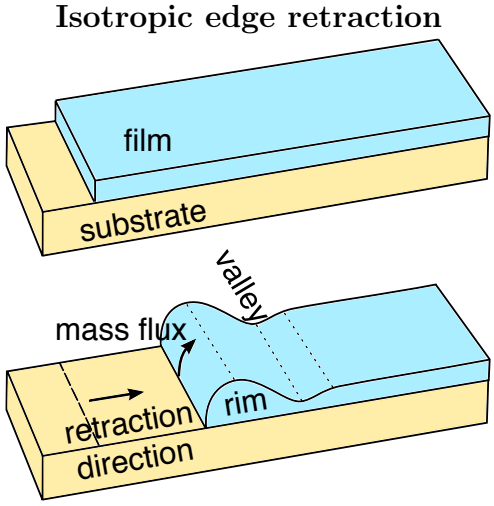

Figure 1-6: During isotropic dewetting, the initially-flat film forms the equilibrium contact angle with the substrate, the corner rounds, and the triple line retracts. Mass accumulation at the film edge generates a rim, and a valley follows.

forms the equilibrium contact angle at the triple line [75, 85]. A thickened rim develops on the edge due to mass accumulation, as shown in Figure 1-6. The thickening rim also lowers the WMC, so the edge retraction rate decreases with time.

As a film edge retracts, a valley may form ahead of the moving rim [75, 85, 27]. Relative to the bulk film height, the valley is roughly an order of magnitude smaller in depth than the rim is tall [75, 85]. As the rim grows, the valley deepens. In no other process interferes, the valley eventually touches the substrate, pinching-off a strip of material, and the cycle begins again with quick adjustment to the equilibrium contact angle, formation of a new rim, and ultimately another pinch-off event [85]. The cyclic formation of valleys and pinch-off has been seen experimentally [88].

However, pinch-off is not always observed. The "fingering instability" may instead dominate the dewetting morphology (see Figure 1-7). This instability is observed in both polycrystalline [37, 38, 53] and single-crystal films [24, 29, 47], and is characterized by growing variations in triple line position and rim height, which eventually develop into an array of protruding fingers. The fingers may undergo a Rayleigh instability [67], as shown on the right in Figure 1-7, and deposit a trail of isolated particles. The spacing and width of the fingers primarily determines the spacing of particles produced via dewetting. Knowledge of the parameters which govern the length scale of break-up can therefore be used to control

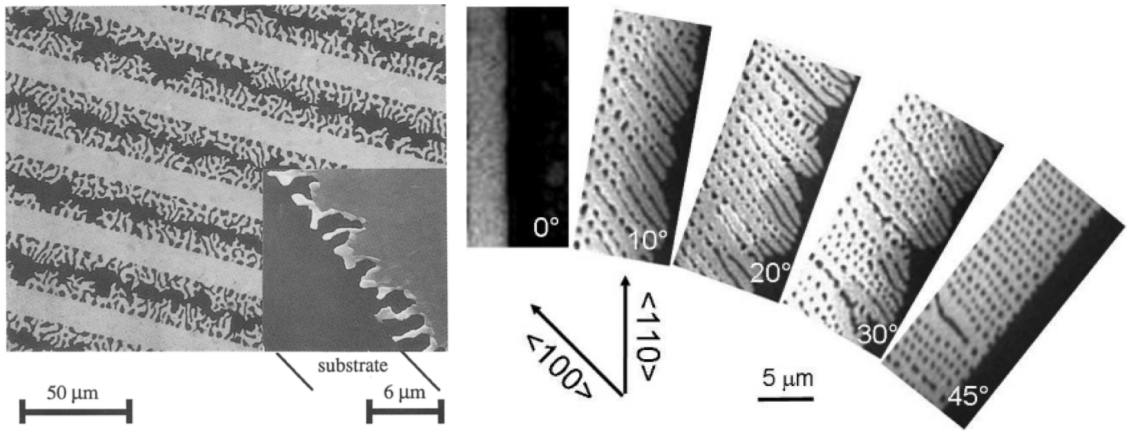

Figure 1-7: Fingering instabilities in polycrystalline Au (left) and single-crystal Si (right) are shown. The images are reproduced from Jiran & Thompson [38] and Leroy *et al.* [47].

structures resulting from via dewetting.

Anisotropic single-crystal films exhibit additional features. They are strongly affected by the crystallographic alignment of the film [24, 89, 60, 76, 29], and edges with different in-plane crystallographic orientations retract at different rates [89, 8]. If the equilibrium shape is composed of flat facets connected by rounded corners, numerical simulations give a rim-and-valley film edge profile [27]. However, when the equilibrium shape is composed exclusively of flat facets with sharp corners, no valley is expected [43]. An absence of valleys is observed for fully-faceted single-crystal Si films [27, 8], Au-Fe films [43], and for some edge orientations in Ni films [34].

Strongly-anisotropic films have edges which are composed of facets. These edges have minimum retraction rates. If a film is patterned with an edge that is not kinetically-stable, it may decompose into stable facets and develop a "staircase" morphology [89]. This break-up is referred to as a "faceting instability."

Strongly-anisotropic films develop polygonal holes bounded by kinetically-stable facets. After the initial stages of growth, the corners are observed to retract faster than the centers of the edges. This is typically referred to as the "corner instability," and leads to dendritic or star-shaped holes [88, 89, 63, 60, 7, 76, 29, 18, 8], as shown in Figure 1-8. Kinetic Monte Carlo simulations of dewetting in single-crystal structures also exhibit corner instabilities [61, 8].

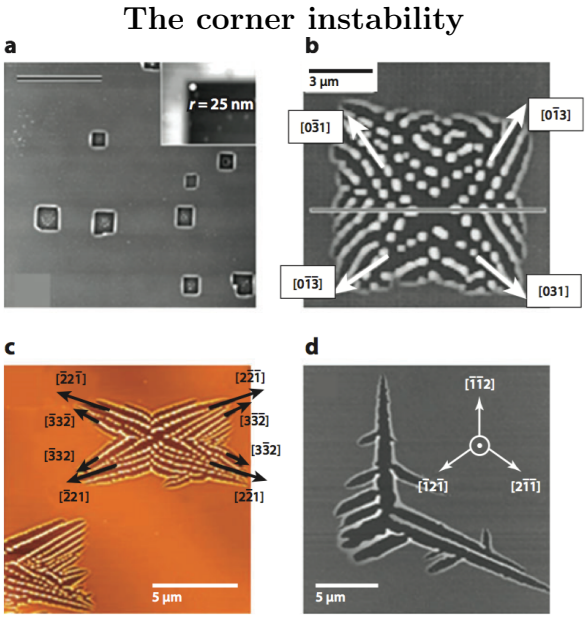

Figure 1-8: Corner instabilities in various materials are shown. The figure is reproduced from the review by Thompson [78], and the sub-figures are from references [76, 60, 29, 7].

1.5 Scope of this work

Although much of the relevant thermodynamic and kinetic framework to describe dewetting has already been developed, many of the mechanisms which govern dewetting remain unknown. Some of the outstanding fundamental questions in capillary-driven surface diffusion are presented in the following chapters, and resolved using advancements in thermodynamic theory (chapters 2 & 3), the development of new analytical models (chapters 4-6), and the development and application of new simulation techniques (chapters 7 & 8). The last chapter discusses broader conclusions about dewetting that can be drawn from this work.

Chapter 2

The Calculation and Display of Interfacial-Energy Minimizing Shapes

2.1 Introduction

To study capillary-driven shape changes, it is essential to know the equilibrium configuration of the system. The equilibrium state defines the direction of evolution. The Wulff construction and Winterbottom construction, introduced in Chapter 1, are approaches to compute the equilibrium shape. However, these constructions are tedious. Having a software tool to do the computation would be advantageous during investigations of dewetting.

There is an additional equilibrium configuration which is relevant in capillary-driven motion. If the substrate is deformable, rather than rigid, a constraint on the interface shape is removed. "Deformable" does not refer to the mechanism by which the system achieves equilibrium, but to the freedom to take the shape which satisfies the energy minimization. For the deformable substrate case, there is no previously known construction.

In this chapter, we present a fast, conceptually simple, analytical method for finding equilibrium morphologies and energies of particles on deformable boundaries, and discuss the possible morphologies and their consequences for microstructures. In addition, a public-domain software suite, Wulffmaker, is developed to enable fast and easy display of equilibrium shapes. A discussion of allowed and non-physical morphologies is aided by these computational tools, and their utility for interpreting real data is demonstrated.

2.1.1 A rigorous approach to finding the equilibrium shape

The equilibrium thermodynamics of interfaces has been formulated by Cahn [9]. He presents a general method of expressing measurable interfacial properties in terms of derivatives of the free energy with respect to the system's independent variables. Cahn's formulation parallels that of Gibbs in that it begins with the interface's differential contribution to the total system energy: γdA. The interfacial tension is a function of the system's independent variables (for example, $\gamma(T, P, \mu_i, \ldots)$ and this choice of independent system variables T, P, μ_i is used below). In elementary treatments, γ does not depend on total interfacial area, A.

The equilibrium values of each phase's entropy, volume, and composition are completely determined by the potentials (T, P, μ_i), and their values within each phase are determined by a convexity condition on the total free energy. This condition applies when there are no constraints on inter-phase exchange of such extensive quantities. However, if the volume of one phase is fixed, a pressure difference develops at the interface of the constrained phase—for isotropic fluid/fluid interfaces, this produces an interface of constant mean curvature. This homogeneous constant mean curvature is a result of minimization and appears as a force balance. A concrete example follows: consider an isolated soap bubble with a fixed volume. Total energy minimization results in a spherical bubble and the pressure difference is $2\gamma/R$. If the soap bubble is in contact with a rigid surface, minimization produces a uniform mean curvature *and* a boundary condition on the dihedral angle at contact [14].

The interface adopts a local composition, entropy density, and volume which are internal quantities—that is, they are completely determined by the system's (μ_i, T, P). For a fluid/fluid interface, its area is also an internal variable which is determined by minimization. For solid/fluid and solid/solid interfaces, additional variables arise. When atoms are prevented from moving from the bulk to the interface, a surface stress occurs. Surface stress is addressed by Weissmüller [82]. When one of the phases is crystalline (or a liquid crystal), γdA generalizes to $\overrightarrow{\xi}\, d\overrightarrow{A}$ where $d\overrightarrow{A}$ includes variation of the interfacial area $|\overrightarrow{A}|$ and the variation of the local surface normal $\hat{n}$ ($\overrightarrow{A} = |\overrightarrow{A}|\hat{n}$). In this case, the capillarity vector, $\overrightarrow{\xi}(p, T, \mu_i, \hat{n})$, depends on orientation, which is an "internal" interfacial variable.

While Cahn's formal derivation utilizing $\overrightarrow{\xi}$ is general and rigorous, when γ is known,

the system's internal geometry is often easier to compute by convexification of γ. This convexification produces the well-known Wulff construction, which always has uniform weighted mean curvature as indicated by minimization with a volume constraint [77]. Convexification is also the proof for the Winterbottom construction [41], and it is the method used in the following sections to demonstrate the "double-Winterbottom" construction for deformable interfaces.

2.1.2 Isolated Particles in Homogeneous Environments: Wulff Shapes

The Wulff construction can become cumbersome in three dimensions because the number of computations necessary grows with the cube of the number of $\hat{n}$'s included. Roosen, McCormack, and Carter developed the public domain software `Wulffman` for the general calculation of Wulff shapes [68]. Their method relies on techniques from computational geometry that are dramatically faster than the Wulff construction. Although `Wulffman` is powerful, fast, and versatile, it has not been supported since 2002 and only runs on Linux operating systems. This paper introduces new software, Wulffmaker, that is distributed as Wolfram *Mathematica* code and as a .cdf, and runs on all platforms. Wolfram now distributes a free visualizer for interactive Computable-Document-Format (cdf) files.

For anisotropic particles, there is distinction between the geometrical contact angle between the particle and the substrate, α, and the equivalent wetting angle, θ, which appears in the Young equation. α is determined by the facets available on the Wulff shape and their inclinations with respect to the substrate, and can only take on discrete values for a fully-faceted particle. α is a local property because it also varies along the triple line as different facets of the Wulff shape are traversed. On the other hand, θ can take any value between 0° and 180°, and encapsulates information about the relative magnitudes of the three interface energies present. θ is defined via the Young equation (see Section 1.3). The appropriate definition of each γ term that determines θ is clear for isotropic particles, but the equivalent γ_{PV} (*i.e.*, considering its multiple values and arbitrary crystallographic orientation) is ambiguous in the case of anisotropic particles. This ambiguity is resolved in the discussion, below.

2.1.3 Particles Attached to Deformable Interfaces

Particles often nucleate at pre-existing defects to eliminate some of the associated defect energy. It is quite common to observe a minor phase in a multiphase system, such as precipitate particles in an alloy, attaching to grain boundaries in the major phase. In this case, the equilibrium shape is more complicated because the particle can distort the boundary and the triple line is not confined to a plane. A similar case occurs when particles of a distinct phase are deposited on a soft substrate, such as when a patterned thin film is annealed at a temperature high enough to allow diffusion in the substrate. The particles can become partially submerged in the substrate to create substrate-particle interface at the expense of particle-environment interface (*e.g.*, [16]). These two cases are examples of particles attached to deformable boundaries, and represent morphologies that occur in technological applications.

To date, no simple method has be demonstrated to find the equilibrium shape of such particles. A Winterbottom-like truncation construction was demonstrated by Cahn and Hoffmann for isotropic or symmetric and twinned particles, but they did not address a means to solve for general geometries [13]. The truncation method was proven in two dimensions [45], and has been applied in two dimensions by overlaying the appropriate Wulff shapes to explain particle morphology [39]. However, the truncation method has not been discussed nor proven in three dimensions. Siem and coworkers presented a general numerical method to find these shapes, but its implementation is impractical and offers little insight into the nature of these geometries [72, 73].

The global stability of a particle attached to an interface is determined by the energy of the wetting particle compared to the energy of the particle in bulk. Methods to calculate the energy of such particles would enable an anisotropic model of heterogeneous nucleation, as well provide insight into Zener pinning for anisotropic particles.

2.2 Methods: The Wulffmaker Software Suite and the Double-Winterbottom Method

In order to calculate equilibrium shapes, software tools were developed to quickly and easily generate Wulff shapes, Winterbottom shapes, and the shapes of particles attached to deformable interfaces, which we call double-Winterbottom shapes. New, fast computational methods to generate Wulff and Winterbottom shapes are developed and implemented in Wulffmaker. A general method for the construction of double-Winterbottom shapes is needed, so a new algorithm was developed and implemented in the Wulffmaker suite. These tools run in Wolfram *Mathematica* 8 or later versions, and are platform-independent. Wulffmaker also runs in Wolfram CDF Player, which is free and available for download: <http://www.wolfram.com/cdf-player/>. The code for these software tools and installation instructions are available online at <pruffle.mit.edu/wulffmaker>.

2.2.1 Wulffmaker for Wulff and Winterbottom Shapes

Wulffmaker employs a new algorithm to quickly generate Wulff shapes. When $\mathcal{W}$ is completely faceted, the computation becomes discrete and finite. In this case, the normal vectors for each facet, $\hat{n}_i$, and their corresponding interface energies, γ_i, are used to construct the Wulff shape (Figure 2-1a). The set of $\hat{n}\gamma(\hat{n})$ from which $\mathcal{W}$ is computed has repeated values (*i.e.*, $\gamma_i(\hat{n}_i) = \gamma_j(\hat{n}_j) = \ldots = \gamma_m(\hat{n}_m)$) when symmetry requires equivalence of several directions (*i.e.*, $\hat{n}_i \sim \hat{n}_j \sim \ldots \sim \hat{n}_m$ where $\overrightarrow{a} \sim \overrightarrow{b}$ implies that there is a symmetry operation that maps $\overrightarrow{a}$ to $\overrightarrow{b}$). The user interface is greatly simplified by utilizing this symmetry so that only one normal and one γ need be specified for all equivalent facets. However, the code computes $\mathcal{W}$ by using all of the $\hat{n}\gamma(\hat{n})$. Symmetrically-equivalent $\hat{n}\gamma(\hat{n})$ are generated by applying each symmetry operation allowed for the specified point group by the following process on the initial set of generating $\{\hat{n}_i\gamma(\hat{n}_i)\}$:

1. Iteratively apply each symmetry operation to each member of the set
2. Add the results of each above operation to the set
3. Remove any redundant elements of the set

4. Repeat 1-3 until the set stops changing.

The result of such an operation is shown in Figure 2-1(b).

Some of the generated $\{\hat{n}_i\gamma(\hat{n}_i)\}$ may have such high energy that they do not appear on the Wulff shape. The Wulff construction requires that the projection of any vector $\overrightarrow{x}_i$ from the origin to the surface of $\mathcal{W}$ onto any other such vector $\overrightarrow{x}_j$ is shorter than $\overrightarrow{x}_j$. Therefore, if the projection of a gamma vector $\hat{n}_i\gamma(\hat{n}_i)$ onto another gamma vector $\hat{n}_j\gamma(\hat{n}_j)$ is longer than $\hat{n}_j\gamma(\hat{n}_j)$ itself, then $\hat{n}_i\gamma(\hat{n}_i)$ does not appear on the Wulff shape, and it can be eliminated from the remainder of the calculation. Additionally, if $\hat{n}_i\gamma(\hat{n}_i)$ is eliminated, then all symmetrically-equivalent gamma vectors must also be eliminated. Therefore, only one member of each set of symmetrically-equivalent vectors undergoes the projection test against all other gamma vectors, and if it fails even once, the entire set of symmetric equivalents are eliminated. The result of this rapid elimination procedure is shown in Figure 2-1(c).

The elimination procedure provides the final list of gamma vectors that correspond to facets on the Wulff shape. Each gamma vector defines a facet plane with $\hat{n}_i$ and a distance to the origin γ_i. The vertices defining $\mathcal{W}$ are where three facet planes intersect, and the edges of $\mathcal{W}$ are where two facet planes intersect. Therefore, $\mathcal{W}$ can be found by calculating all of the points where three facets on the Wulff shape intersect, and selecting only those that fall on the surface of $\mathcal{W}$ (using the same elimination procedure as above). The vertices on the surface are always generated by adjacent, or nearest-neighbor, gamma vectors. The nearest neighbor metric is defined by the projection of other $\hat{n}\gamma(\hat{n})$ onto the vector in question. To reduce the number of vertices that must be calculated, a list of nearby gamma vectors is assembled for each $\hat{n}_i\gamma(\hat{n}_i)$. The intersection points of each facet plane i with its neighbors are calculated and tagged with the identities of the three facet planes that generated it. All of the intersection points generated from two example facet planes are shown in Figure 2-1(d).

The elimination procedure applied to remove $\hat{n}\gamma(\hat{n})$'s that are too large also works for the elimination of intersection points that do not appear on the surface of $\mathcal{W}$. Each intersection point is projected onto the nearby gamma vectors, and if the projection is longer than the gamma vector, that point is eliminated. The remaining points define the Wulff shape, as shown in Figure 2-1(e).

After the vertices are computed for each facet, they are reordered by sorting with respect to right-handed rotation about the normal. The result is a list of the vertices that define the edges of each facet on the Wulff shape, which are plotted in Figure 2-1(f).

The user interface for Wulffmaker is shown in Figure 2-2. There are several variants of Wulffmaker, including a version that makes it easy to introduce many hundreds or thousands of facets with equal interface energy, which approximates an isotropic interface which may be included as part of $\mathcal{W}$. Another variant displays the total interface area of each facet type to aid in the interpretation of experimental observations. All crystallographic symmetries are available, along with the 32 point groups. The viewing direction, or "zone axis," can be typed in, or the user can click and drag the figure to the desired orientation. The interface energies can be specified by typing in values, and the $\triangleright$ button on the interface energy sliders can be pressed to animate through the range of interface energies. Wulffmaker typically solves and renders Wulff shapes in a fraction of a second on (circa 2010) laptops, which makes it also appropriate for live demonstrations or as a teaching tool. Because the tool is written with Wolfram *Mathematica*, modifications to the source code are relatively easy and allow for customization, including custom graphing options, custom non-crystallographic symmetries, and adding features.

The Winterbottom variant of Wulffmaker includes controls for the orientation of a substrate, a slider for $(\gamma_{SV} - \gamma_{SP})$, and additional plotting options. There is also an option to "show data", which produces a print-out below the figure of the equivalent wetting angle θ, the value of γ_{PV}, the volume of the Winterbottom shape, the total energy of the system, and the contact area between the particle and substrate.

2.2.2 Double-Winterbottom Construction

The Winterbottom construction applies for particles sitting on a non-deformable substrate. However, in many cases, such as a particle attached to a grain boundary or a particle supported by a soft substrate, the Winterbottom construction does not apply. A new method is needed to calculate equilibrium shapes on deformable boundaries.

Consider a particle, P, attached to a boundary between phase A and phase B. The AB interface is taken to be isotropic, and the PA and PB interfaces may be anisotropic. The

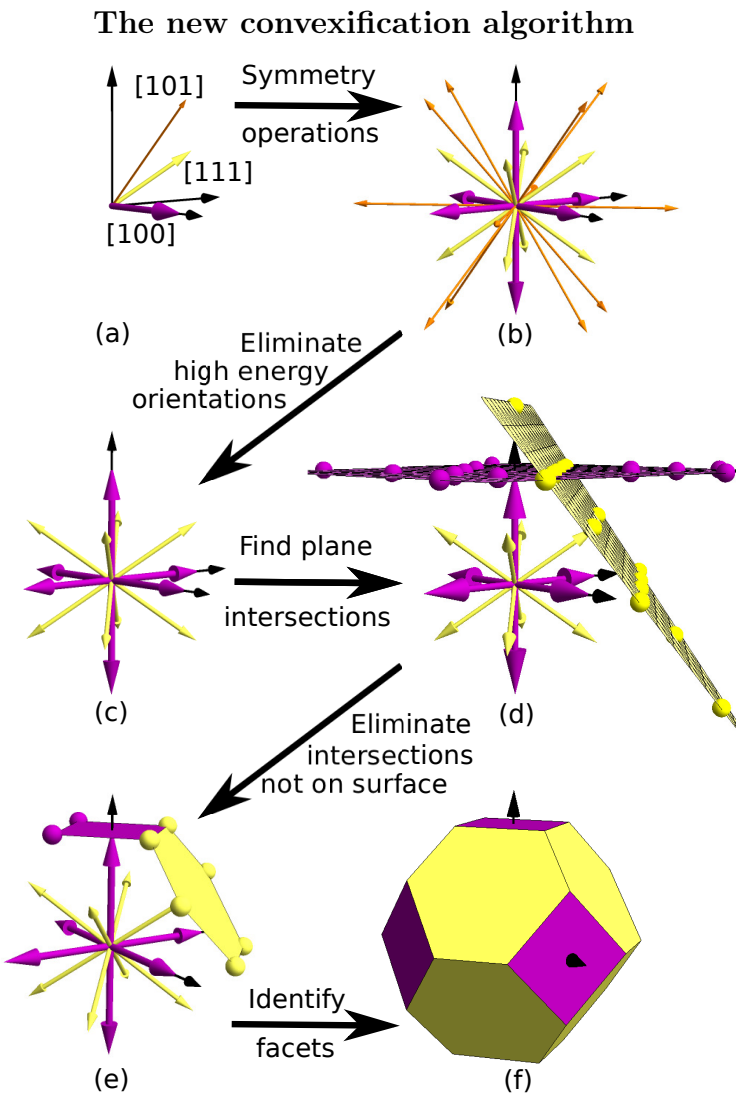

Figure 2-1: The method developed for finding Wulff shapes is depicted. (a) The user specifies the symmetry and the $\hat{n}_i\gamma(\hat{n}_i)$ vectors. In this case, $\hat{n}_1 = [100]$, $\gamma_1 = 1$, $\hat{n}_2 = [111]$, $\gamma_2 = 0.9$, $\hat{n}_3 = [101]$, $\gamma_3 = 1.5$. These are the "generators" for all gamma vectors. (b) The symmetry operations allowed under the specified point group are repeatedly applied to generate all symmetrically-equivalent gamma vectors. (c) Each generator is projected onto every other gamma vector. If the projection of the generator is longer than the gamma vector it was projected onto, then that generator and all symmetrically-equivalent gamma vectors are eliminated. (d) Each gamma vector defines a facet plane with normal $\hat{n}_i$ and distance to the origin γ_i. Every point where three facet planes intersect is identified as a possible vertex location. For clarity, only the intersection points that fall onto two example facet planes are shown. (e) Each possible vertex is projected onto the nearby gamma vectors. If the projection of the possible vertex is longer than the gamma vector it was projected onto, then that vertex is eliminated. The surviving vertices define the facets on $\mathcal{W}$. (f) The surviving vertices are put in order so that connecting them successively defines the facets of the Wulff shape.

The Wulffmaker user interface

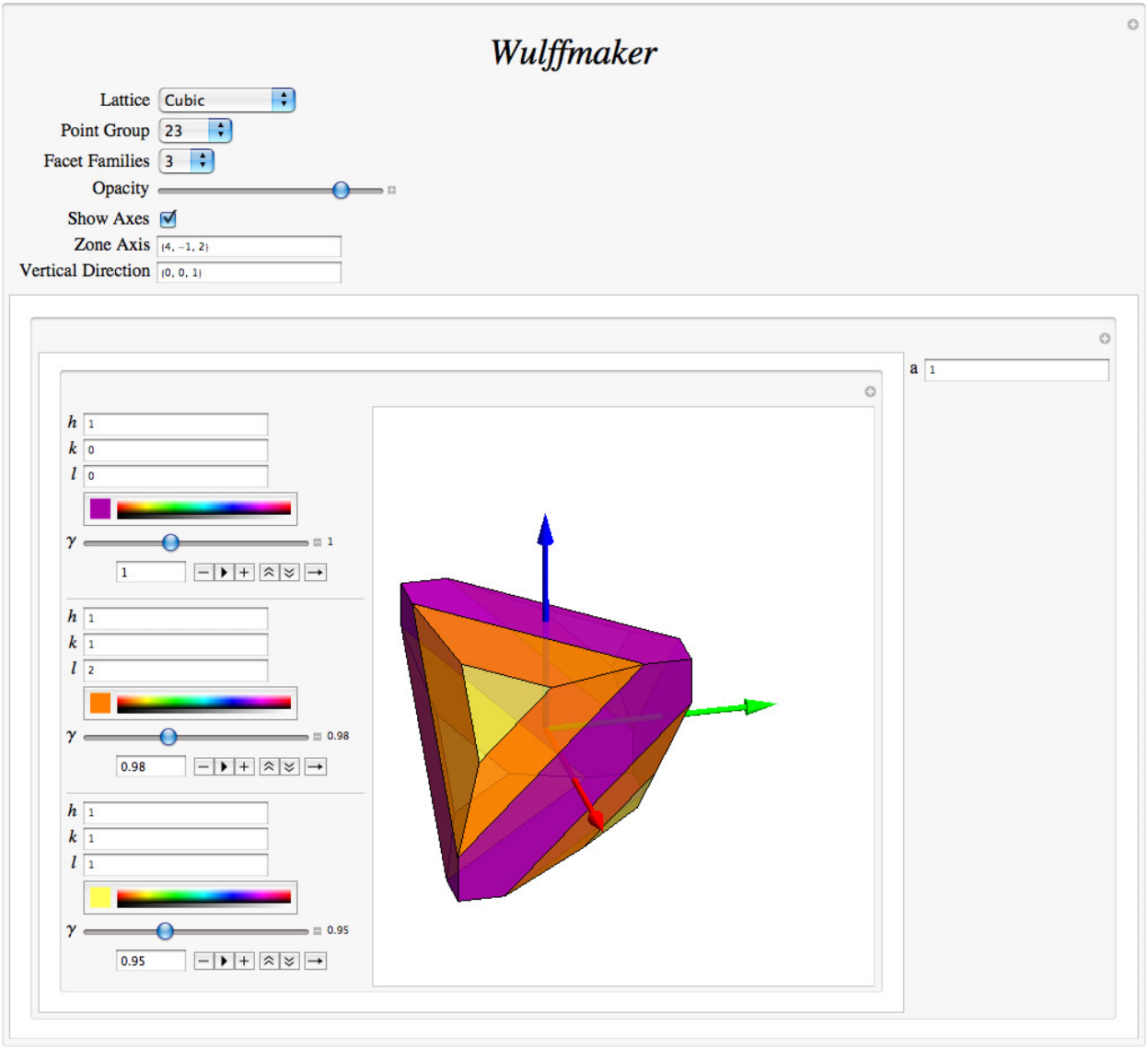

Figure 2-2: The basic user interface for Wulffmaker is shown. The lattice symmetry, point group, number of crystallographically-distinct facets to include, and plotting preferences are set at the top. The orientations of facets to include, as well as their surface energy and color, are selected at left. The magnitudes of the crystallographic axes and angles (if variable under the selected symmetry) are entered at right.

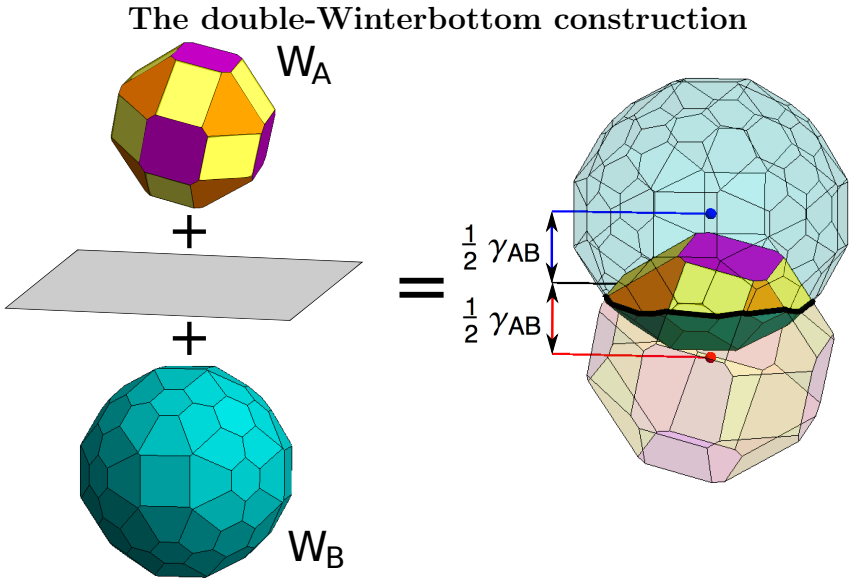

Figure 2-3: The double-Winterbottom method is demonstrated. Left: The Wulff shape of the particle in bulk A, $\mathcal{W}_A$, the Wulff shape of the particle in bulk B, $\mathcal{W}_B$, and an initially planar interface are shown. Right: The centers of each Wulff shape are displaced away from the interface by an amount $\frac{1}{2}\gamma_{AB}$. The $\gamma = 0$ point on each Wulff shape is shown with a dark point, and the triple line is indicated by the heavy black line.

triple line is not necessarily confined to the plane of the AB boundary. Let the Wulff shape of the particle in bulk A be $\mathcal{W}_A$, the Wulff shape in bulk B is $\mathcal{W}_B$.

To find the equilibrium shape of the particle, the Winterbottom method can be applied to each side of the interface. When calculating $(\gamma_{SV} - \gamma_{SP})$, there is no particle-substrate interface energy because the interface is eliminated within the particle (see Figure 2-3). Given that the Winterbottom method is applied to each side of the AB interface, the equivalent to substrate-environment interface energy becomes $\frac{1}{2}\gamma_{AB}$, so that summing the projected top- and bottom-side interface energies (described below) gives γ_{AB}. The particle shape can be found by displacing $\mathcal{W}_A$ below the interface by an amount $(\gamma_{SV}\text{-}\gamma_{SP}) = (\frac{1}{2}\gamma_{AB} - 0)$, and likewise displacing $\mathcal{W}_B$ above the interface by $\frac{1}{2}\gamma_{AB}$. The intersection of $\mathcal{W}_A$ and $\mathcal{W}_B$ after the displacement gives the equilibrium particle shape.

To demonstrate the validity of the double-Winterbottom method, we can compare the energy of facet i when P is in bulk versus when P is attached to the AB interface. The

interfacial free energy contributed by facet i when P is in bulk A is

$$E_i = \gamma_i A_i \tag{2.1}$$

where γ_i is the interface energy density of facet i, and A_i is the area of facet i. When P is attached to the AB interface, then the energetic contribution of facet i becomes

$$E_i = \gamma_i A_i - \frac{1}{2}\gamma_{AB} A_i^{proj}, \tag{2.2}$$

where A_i^{proj} is the projected area of facet i onto the AB boundary, because it replaces an amount A_i^{proj} of AB interface (see Figure 2-4). The factor of $\frac{1}{2}$ comes from the PB interface also projecting onto the AB interface, so the PA and PB interfaces must share the energetic benefit of removing AB interface. If the two halves did not equally share the energetic benefit, then one side of the particle would be lower energy than the other, and the particle will adjust its morphology to create more of the low energy interface at the expense of the high energy interface until the two are equal. The effective interface energy density of facet i is E_i/A_i, which is:

$$\frac{E_i}{A_i} = \gamma_{i,\text{eff}} = \gamma_i - \frac{A_i^{proj}}{2A_i}\gamma_{AB}. \tag{2.3}$$

Therefore, the equilibrium shape of the particle should be the one with the $\gamma = 0$ point on the AB interface, composed of the available facets from the PA interface above and PB interface below the AB boundary, except their interface energies are replaced by $\gamma_{i,\text{eff}}$. This is identical to the double-Winterbottom construction because if the $\gamma = 0$ points for $\mathcal{W}_A$ and $\mathcal{W}_B$ were re-defined to be at the same location on the AB interface (which has no effect on the Wulff shapes themselves [46]), geometry shows that the new distances to the facets will be $\gamma_{i,\text{eff}} = \gamma_i - \frac{1}{2}\gamma_{AB}\cos\beta$, where β is the angle between the normal to the AB interface and the normal to facet i (see Figure 2-4). Geometric consideration also reveals that $\frac{A_i^{proj}}{A_i} = \cos\beta$, so the two descriptions are equivalent.

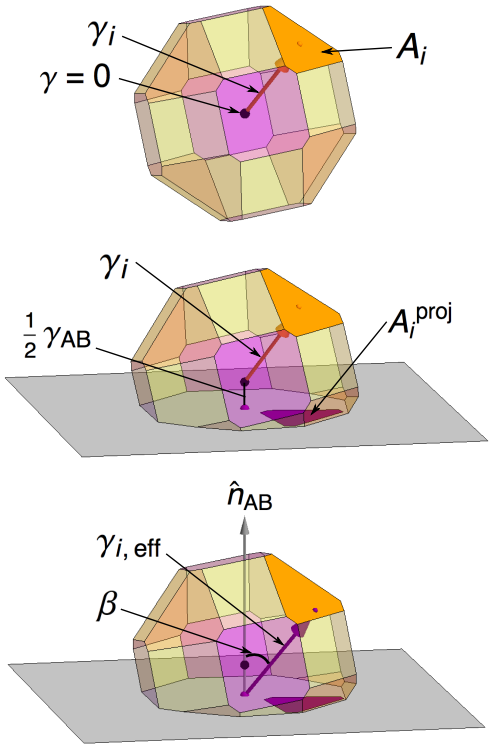

Figure 2-4: The double-Winterbottom method is compared with the energetic description of wetting, to show their equivalence. Top: the Wulff shape of a material is shown with the interface energy and area of facet i. Middle: Facet i has an interface energy of γ_i, but because it removes some AB interface with area A_i^{proj} (the projection of facet i onto the substrate is shown as a dark "shadow"), its effective interface energy becomes $\gamma_{i,\text{eff}} = \gamma_i - \frac{A_i^{proj}}{2A_i}\gamma_{AB}$. Bottom: The double-Winterbottom construction indicates that the $\gamma = 0$ point should be placed a distance $(\gamma_{SV} - \gamma_{SP}) = (\frac{1}{2}\gamma_{AB})$ above the AB interface, resulting in an effective surface energy of $\gamma_{i,\text{eff}} = \gamma_i - \frac{1}{2}\gamma_{AB}\cos\beta$. The position of facet i in the middle and bottom graphics is identical.

2.2.3 Wulffmaker for Double-Winterbottom Shapes

The Wulffmaker algorithm for calculating double-Winterbottom shapes uses the method described in Figure 2-1 to generate $\mathcal{W}_A$ and $\mathcal{W}_B$. Then, the Wulff shapes are rotated relative to the AB interface to satisfy the user-specified orientation relationships. The center of $\mathcal{W}_A$ is shifted along the interface normal by $-\frac{1}{2}\gamma_{AB}$, and $\mathcal{W}_B$ is shifted along the interface normal by $\frac{1}{2}\gamma_{AB}$, as indicated by the double-Winterbottom construction. The result is two overlapping shapes, as shown on the right in Figure 2-3. The Wulff shape-finding algorithm described in Section 2.2.1 is applied to the overlapping shape to select the union of $\mathcal{W}_A$ and $\mathcal{W}_B$ and to identify the triple line ABP position. Because the triple line may not be planar, there is additional AB-interface energy associated with satisfying the boundary conditions at the triple line.

The AB interface is assumed to be both deformable and isotropic, so the AB interface can distort such that it meets the particle at the triple line. It is assumed that far from the particle, the AB-interface approaches a plane. The equilibrium shape of the AB interface is found by discretizing it and allowing each mesh point to apply a tension on its neighboring mesh points equal to the interface tension of the AB boundary. With the mesh points on the triple line fixed, the model converges to the minimum energy configuration for the AB interface. The total area of the AB interface will be augmented by deviations from the plane, or "wrinkles," which arise from the interface being constrained to meet the triple line. The consequences of the presence of wrinkles are discussed in Section 2.3.3.

The ABP triple line will not generally fall near the original AB interface position when using the double-Winterbottom construction. For example, in Figure 2-3, the triple line is below the original interface. This occurs when the average interface energy on $\mathcal{W}_A$ is different from that of $\mathcal{W}_B$. To correct this offset, the entire particle is shifted by an amount equal to the mean normal displacement of the triple line from the AB interface so that it is in-plane with the interface. Physically, the triple line should align with the interface because an average displacement would create unnecessary AB interfacial area.

To analyze the stability of the particle, the total energy is computed as the sum of the energetic contributions from the part of the particle in contact with A, the part of the

particle in contact with B, the energy gain from replacing a portion of the AB interface with the particle, and the energy penalty from creating new AB interface area as wrinkles. Wulffmaker displays the total energy of a particle of equal volume if embedded within bulk A and bulk B for comparison with the total energy of the double-Winterbottom shape.

The user interface for generating double-Winterbottom shapes is similar to that for Wulff shapes, except there are additional controls for the additional degrees of freedom, including the particle's orientation with respect to the interface and interfacial energy of the AB interface, the orientation relationships between $\mathcal{W}_A$, $\mathcal{W}_B$, and the AB interface, and plotting options (such as opacity, how much of the discretized AB interface to display, whether to highlight the triple line, etc.). There is also an option to "show data," which reports a breakdown of energetic contributions to the overall double-Winterbottom shape energy, the total energies of $\mathcal{W}_A$ and $\mathcal{W}_B$, the equivalent wetting angles for each half, and the value of γ_{PA} and γ_{PB} used to find the equivalent wetting angles. The source code is included with the distribution, so with relatively simple changes, default values and elements of the calculation can be modified by the user.

2.3 Discussion

2.3.1 The Equivalent Wetting Angle

In equation 1.5, the contact or wetting angle θ is defined in terms of γ_{SP}, γ_{PV}, and γ_{SV}. It would clarify the description—and comparisons to the isotropic cases—of the Winterbottom and double-Winterbottom constructions if there were a convenient way to define θ in the general, anisotropic case. γ_{SP} is well-defined for the Winterbottom shape, and is zero for the double-Winterbottom shape. γ_{SV} is also defined for the Winterbottom case, and becomes $\frac{1}{2}\gamma_{AB}$ in the double-Winterbottom case. However, identifying a simple equivalent for γ_{PV} is non-trivial because the interface-mediated equilibrium-shape depends on the relative crystallographic orientation to the substrate/interface for the same unattached Wulff shape. For example, consider the case of a Wulff shape consisting only of (100)-type facets with $\gamma = 1$, so that $\mathcal{W}$ is a simple cube (see Figure 2-5). In the Winterbottom case, if the substrate

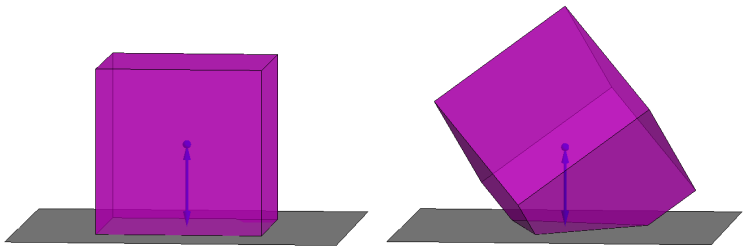

Figure 2-5: A cubic Wulff shape of fixed volume with $\gamma = 1$ is shown on a substrate with $(\gamma_{SV} - \gamma_{SP}) = 1$. Left: The *SP* interface is along a [100] facet, so the shape is not truncated at all, and has an equivalent wetting angle of 180°. Right: The *SP* interface is along a [111] orientation, and the corner on the Winterbottom shape is truncated. The equivalent wetting angle is 125.3°.

orientation is along a (100) direction, then complete dewetting of the substrate (the point at which the Wulff shape no longer intersects the substrate when shifted by $\gamma_{SV} - \gamma_{SP}$) occurs when $\gamma_{SV} - \gamma_{SP} = 1$. However, if the cube is oriented into a [111]-orientation with respect to the substrate, complete dewetting will not occur until $\gamma_{SV} - \gamma_{SP} = \sqrt{3}$. This orientation dependence can be accounted for by defining γ_{PV} to be the distance from the $\gamma = 0$ point to the surface of the Wulff shape along the direction parallel to the interface normal. Experimentally, γ_{PV} can be measured along a symmetrically-equivalent axis, or on an isolated particle in the same medium. Computationally, the value of γ_{PV} is found by extending all planes on the Wulff shape to intersect the vector parallel to the substrate/interface normal, and identifying the lowest intersection value. On a double-Winterbottom shape, each half of the particle has its own wetting angle, so in general, an equivalent wetting angle must be reported for each side.

2.3.2 Contact Area

By default, Winterbottom shapes are calculated with a constant volume. The effects of varying the wetting angle are shown in Figure 2-6. As θ approaches 0°, the particle approaches complete wetting of the interface, so the contact area between the particle and the substrate diverges. As θ approaches 180°, the contact area approaches that of the facet on the Wulff shape parallel to the substrate. In between, the contact area will change discontinuously when facets appear on the Winterbottom shape. The same general trend is observed for

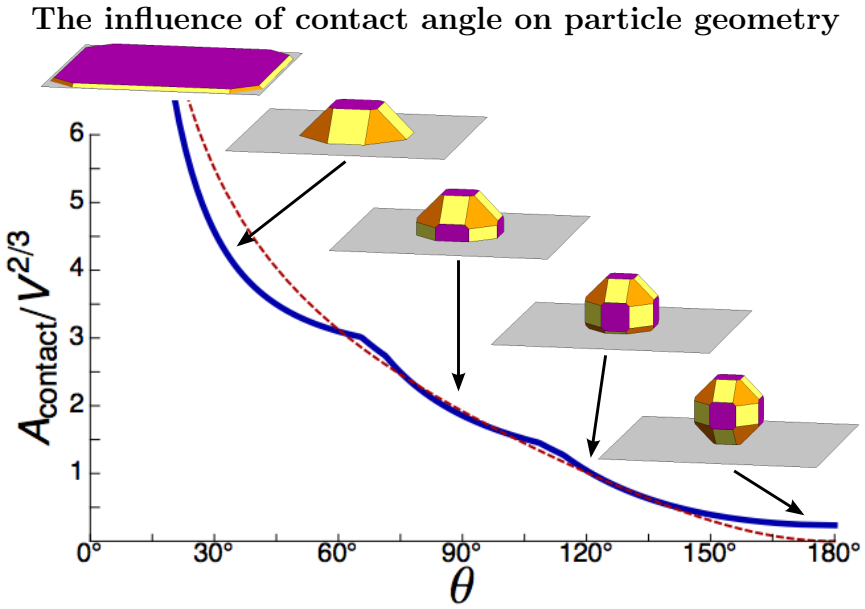

Figure 2-6: For a given Wulff shape and fixed particle volume, the contact area between the particle and the substrate decreases as the equivalent contact angle, θ, increases (thick line). The contact area for an isotropic (spherical) particle is shown for comparison (dashed line).

double-Winterbottom shapes (see Figure 2-8). Contact area versus particle volume can be used to estimate the equivalent wetting angle and constrain the relative interface energies.

In the case of double-Winterbottom shapes, the definition of contact area is slightly less well defined because there is no interface within the particle. To find the area of interface removed, Wulffmaker projects the position of the triple line onto the original plane of the interface, and takes the inscribed area to be the equivalent to contact area.

2.3.3 Wrinkles and the Limitations of Wulffmaker

Wulffmaker provides a first-order model of the equilibrium shape of a particle attached to a deformable interface. However, the non-planar nature of the triple line introduces some second order effects which can become significant under certain conditions. The main limitation is that Wulffmaker does not adjust the particle shape in response to wrinkles that form in the surrounding AB interface. The wrinkles create new interfacial area, and introduce an additional term in the energy minimization. When γ_{AB} is very small, then the triple line tends to take a more circuitous path and causes a lot of interfacial area to

be formed (see Figure 2-8), but the energetic contribution is typically negligible ($< 1\%$ of the total particle energy) as $\gamma_{AB} \to 0$. When γ_{AB} is large, then the double-Winterbottom construction results in near-planar triple lines, so the AB area created is small, and the energetic contribution is negligible. However, when:

1. one or both halves of the particle have facets that meet at sharp angles, where "sharp" means $\approx 90^\circ$ or larger,

2. the orientation relationship between $\mathcal{W}_A$ and $\mathcal{W}_B$ is such that the triple line is forced to traverse the sharp angles and dramatically deviate from planar, and

3. γ_{AB} is on the order of γ_{PA} and/or γ_{PB},

then the energetic contribution of the wrinkles can become as high as several percent of the total energy of the particle (see Figure 2-7). However, only few geometries can be devised that meet all 3 criteria, and few materials have Wulff shapes that could cause significant energetic contributions from the wrinkles. In the vast majority of cases tested, the energetic contribution from wrinkles does not exceed $\sim$2%. If the wrinkle contribution is deemed to be significant enough to materially alter the particle shape, the system could respond in numerous ways to this additional energetic contribution. The facets near the triple line may change shape to minimize deviations from the interface plane. Or, facets which normally do not occur on the Wulff shape may be stabilized by the presence of the AB interface, and new facets could appear. Wulffmaker includes a readout of the wrinkle energy (within the "show data" option) so the user can judge whether the contribution is negligible or not. However, because the effect of wrinkle energy is uncertain, Wulffmaker does not treat its inclusion in shape generation.

Another limitation of Wulffmaker is that the assumption that the AB interface is isotropic may not hold for some systems. Any anisotropy in the surrounding interface will cause the actual equilibrium particle shape to differ from the double-Winterbottom shape. Anisotropy in the AB interface would constrain the shape of the triple line, and may even force the particle towards a more Winterbottom-like shape, but with the added condition that the particle halves must somehow meet. This case is not treated by Wulffmaker.

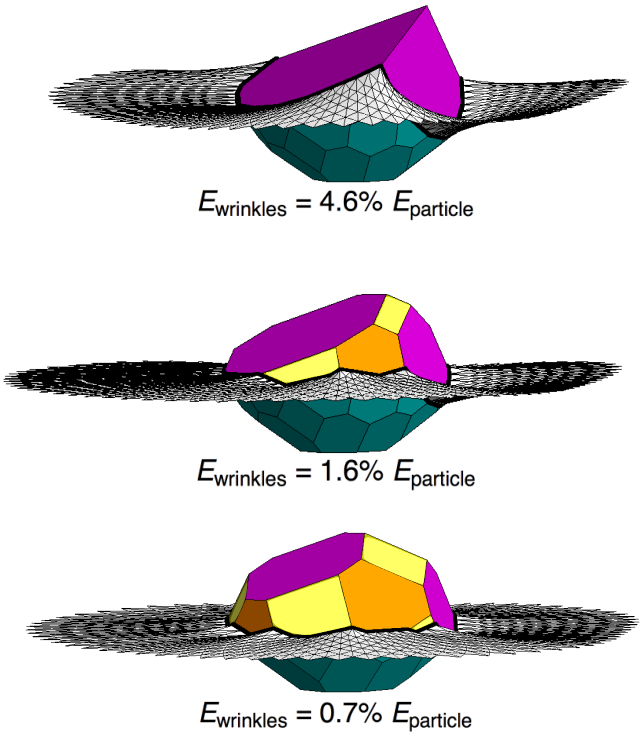

Figure 2-7: The conditions necessary for wrinkles to contribute significantly to the total energy of a particle are demonstrated. Top: only [100]-type facets are available, and the orientation relationship is such that the triple line must traverse sharp edges. Middle: small [110] and [111]-type facets "soften" the corners, and significantly reduce the energetic contribution from wrinkles. Bottom: the wrinkle area is negligible when the triple line is nearly contained within a plane. In all three pictures, the full extent of the calculated AB interface is not shown, for clarity.

When γ_{AB} is small, facets normal to the interface may appear on the equilibrium shape. If a facet from W_A is oriented identically to a facet on W_B, and they have the same γ value, then the triple line could traverse the common facet, rather than strictly follow edges between facets. In its current version, Wulffmaker cannot find the triple line location in this special case because it is difficult to determine where it will fall and what functional form it will take.

Another possible energetic contribution that is not accounted for is edge energy. It is conceivable that the presence of edges or corners introduces an energetic penalty beyond the interface energies of the adjacent facets. The Wulff construction does not address such a possibility, nor does any method discussed herein.

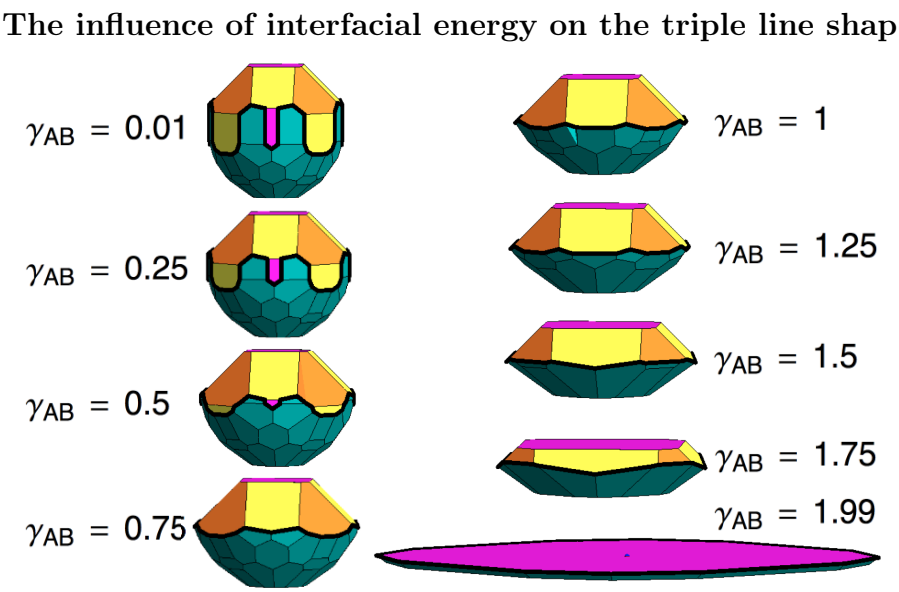

Figure 2-8: For a fixed orientation relationship and with all $\gamma_P = 1$ on the particle, γ_{AB} is varied. Top: as $\gamma_{AB} \to 0$, the triple line becomes very long because the interface only weakly affects the particle morphology. Bottom: as $\gamma_{AB} \to 2\gamma_P$, the particle approaches complete wetting of the interface. γ_{AB} is pulling very hard on the triple line, forcing it to fall into the plane of the AB interface.

2.3.4 Calculating interface energies from the equilibrium shape

Another application for Wulffmaker is an inverse method of finding relative interface energies given an experimental observation of the equilibrium shape of a particle. Measurements of angles between facets and their symmetry can be used to identify their relative orientations, and relative edge lengths can be used to constrain interface energies. Once all facet indices and orientation relationships are specified in the software, the interface energy sliders can be used to match the observed geometric parameters. There are versions within the Wulffmaker suite that include readouts of relative edge lengths. Alternatively, if the area fraction occupied by each facet type can be measured experimentally, the software can be used to match area fractions and therefore provide interface energies.

An example inverse solution is demonstrated in Figure 2-9. The micrograph from Dahmen *et al.* contains two single-crystal Pb particles attached to a 90° [110] Al grain boundary. Each particle has a fully-faceted half with $m\bar{3}m$ point symmetry, and the other half appears isotropic. The faceted halves are crystallographically aligned (topotactic) with their respective Al host as derived from the moiré patterns [22].

The Wulff shape for crystallographically-aligned Pb in Al is known to show the (100) and (111) facets with $\frac{\gamma_{100}}{\gamma_{111}} = 1.15$ [52]. This information was used to constrain the software fit. All that remains unknown are $\frac{\gamma_{GB}}{\gamma_{111}}$ and $\frac{\gamma_{PbAl}}{\gamma_{111}}$, where γ_{GB} is the interface energy of the Al grain boundary, and γ_{PbAl} is the interface energy of Pb in Al when it is not crystallographically aligned (isotropic side). To quantitatively extract interface energy values, some geometric measurement must be made. In the case of Figure 2-9, the viewing direction is known from TEM conditions to be [110], so that several facets are seen edge-on, and the 2D-projection geometry is sufficient to constrain the γ's.

The region of the grain boundary surrounding the top particle in Figure 2-9 is oriented about 25° relative to the grain boundary surrounding the lower particle, so a different γ_{GB} was found for each particle.

The relative lengths of the edge-on facets, the apparent contact angles, the apparent radius of curvature of the PB interface relative to particle volume, and the apparent particle widths were used as geometric constraints. Using these metrics, Wulffmaker obtains $\frac{\gamma_{GB}}{\gamma_{111}} \approx 0.85 \pm 0.1$ for the top grain, $\frac{\gamma_{GB}}{\gamma_{111}} \approx 1.22 \pm 0.1$ for the lower grain, and $\frac{\gamma_{PbAl}}{\gamma_{111}} \approx 1.27 \pm 0.1$.

2.3.5 Allowed and Non-Physical Morphologies

A series of double-Winterbottom shapes are shown in Figure 2-10, and present a summary of allowed morphologies. This example is a particular case that generates general morphological features. The example particle has cubic symmetry and is faceted on the A side of the interface with each ([111],[100],[110]) facet having $\gamma_{PA} = 1$. The PB-interface is a faceted approximation to a spherical patch. The A side is fixed with the equivalent wetting angle $\theta_{AP} = 60°$, and the interface energy on the B side is varied through the sequence of simulations (*e.g.*, $\theta_{PB} = 1°, \ldots, 72.7°$). In all cases, the discussion is focused on global minima for the energy of the system, but metastability is always possible. If the particle is at the global minimum when attached to the AB interface, local minima exist where the particle is embedded completely within bulk A or bulk B.

When γ_{PB} is close to γ_{PA} (≈ 1), the particle has a lenticular form. When γ_{PB} is less than $\frac{1}{2}\gamma_{AB}$, the particle will have a "hemispherical" morphology, similar to that in the top left of Figure 2-10. This morphology occurs because although complete wetting would lower

Comparison of real and modeled double-Wintrebottom particles

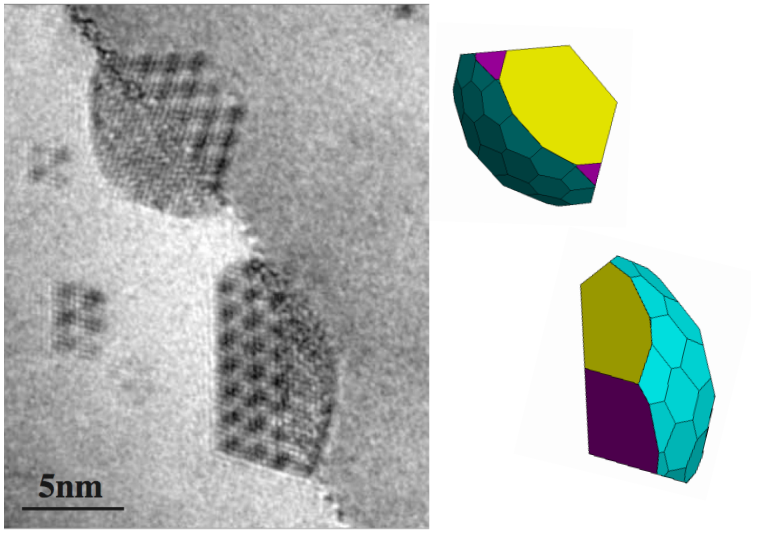

Figure 2-9: Left: A micrograph from Dahmen *et al.* shows two Pb particles attached to a grain boundary in Al. The top particle is topotactic with the Al grain on the right, and the lower particle is topotactic with the Al grain on the left. The interface between the particles and the non-topotactic grains are taken to be isotropic [22]. This figure is reprinted with permission from the original journal of publication. Right: Wulffmaker was used to fit the particle geometries to find $\frac{\gamma_{GB}}{\gamma_{111}}$ and $\frac{\gamma_{PbAl}}{\gamma_{111}}$, given that $\frac{\gamma_{100}}{\gamma_{111}} = 1.15$ for Pb/Al interfaces.

the energy on the B side of the AB interface, it would increase the energy on the A side. The PA interface holds the particle back and prevents complete wetting.

When γ_{PB} is very large, the penalty of having any PB interface is so great that the particle will have lower energy if entirely embedded within A. For the example shown, this occurs when $\gamma_{PB} > 1.68\gamma_{AB}$. Note that this wetting transition occurs well below the expected value of $2\gamma_{AB}$ for a Winterbottom-like geometry, where the $\mathcal{W}_{PA}$ is shifted relative to the AB interface, without consideration of the PB interface. This is because the particle is not truncated by a plane, but is truncated a curved interface, which has more interfacial area. The additional area from the curvature of the PB side of the interface creates additional energy, causing the wetting transition to occur at smaller γ_{PB}.

When $1.64 \leq \gamma_{PB} \leq 1.68$, the particle contains "overturned" facets on the A side (*i.e.*, their normal is directed towards the AB-interface). The overturned facets cancel any region of the PA-interface which projects onto them from above, thus any benefit of removing AB interface is negated. However, overturning allows the higher energy interface area to decrease. Overturned facets are possible because the balance of interface energies (Equation 1.5) can

be satisfied, but such shapes only occur when the particle is on the cusp of instability on the interface. Furthermore, the overturned facets are stable over a very small range of relative γ values because the associated energetic penalty quickly overwhelms the benefit of partially wetting the AB interface.

In summary, there are five regimes of relative γ values for double-Winterbottom particles:

1. When $\gamma_{PA} + \gamma_{PB}$ is less than γ_{AB}, the particle completely wets the interface.

2. When either γ_{PA} or γ_{PB} is less than $\frac{1}{2}\gamma_{AB}$ and $\gamma_{PA} + \gamma_{PB} > \gamma_{AB}$, then the particle takes on a "hemispherical" shape, with the flat surface on the high energy side, and the domed surface on the low energy side of the interface.

3. When γ_{PA} and γ_{PB} are of similar magnitude, the particle has a lenticular shape. This is true even when both γ_{PA} and γ_{PB} are very large compared to γ_{AB}.

4. When either γ_{PA} or γ_{PB} is large, overturned facets may occur on the low energy side. This only occurs when the energy of the particle on the interface is nearly equal to the energy of the particle if embedded within bulk of the lower energy environment.

5. When either γ_{PA} or γ_{PB} is so large that it overwhelms the energetic benefit of partially wetting the interface, the particle will have minimal energy when embedded completely in the bulk of the lower energy environment.

For a particle without an internal boundary (that is, a single crystal particle), the particle must be convex for two reasons. First, Wulff shapes are always convex to minimize interfacial area, and double-Winterbottom shapes are no different. Secondly, for particles attached to interfaces, it is not possible to have "dumbbell"-shaped particles, (*i.e.* particles which are non-convex near the triple line), because the balance of interface tensions at the triple line would require that the AB interfacial energy is negative, which is non-physical. For particles which do contain an internal boundary, *e.g.* a twin boundary, the Wulffmaker software suite can be used to generate their geometry by applying the Winterbottom construction to half of the particle with a known internal boundary energy, and then mirroring it across the interface.

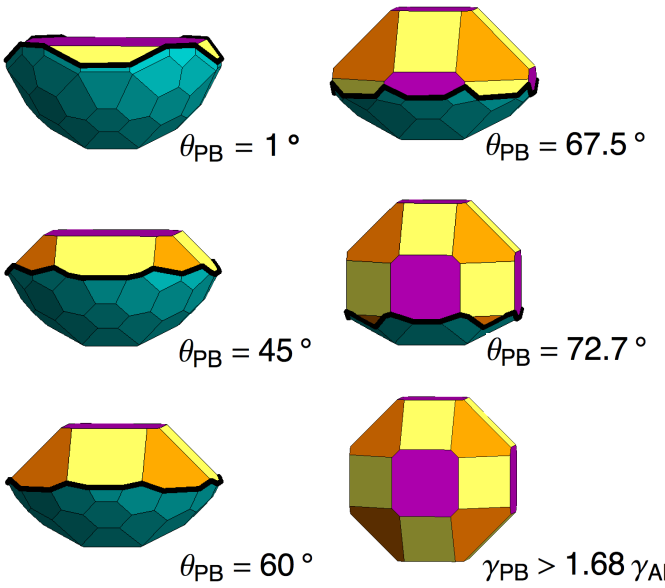

Figure 2-10: Example calculations are shown to describe the allowed morphologies of double-Winterbottom shapes. $\mathcal{W}_A$ is faceted with cubic symmetry, and $\mathcal{W}_B$ is isotropic. $\gamma_{AB} = \gamma_{PA} = 1$ for all facets on the PA interface, and γ_{PB} is varied. When $\gamma_{PB} < \frac{1}{2}\gamma_{AB}$ and $\gamma_{PB} + \gamma_{PA} > \gamma_{AB}$, the particle can minimize its total energy by assuming a hemispherical shape, as in the top left. When $\gamma_{PB} > 1.68\gamma_{AB}$, the particle is no longer globally stable on the interface, and is instead embedded in bulk A. Wetting no longer occurs when $\theta_{PB} > 72.7°$. Overturned facets (small triangular facets near the triple line) are visible on the $\theta_{PB} > 72.7°$ shape. For $\frac{1}{2}\gamma_{AB} < \gamma_{PB} < 1.68\gamma_{AB}$, the particle is stable when wetting the AB interface.

2.3.6 Consequences of Anisotropy on the Wetting of Interfaces

As discussed in the context of Winterbottom shapes, anisotropy greatly affects the stability range of particles on interfaces. For a given particle and substrate, (*i.e.* fixed $\gamma_{SV} - \gamma_{SP}$), the stability of a particle may vary with interface orientation, as shown in Figure 2-5. Double-Winterbottom shapes may attach to the interface, or dewet the interface and be completely embedded in the phase above the interface, or become completely embedded in the phase below the interface. This "choice" between globally- and locally-stable solutions and the appearance of unstable solutions, creates a richness of behavior for particles on soft interfaces demonstrated in Figure 2-10.

Even if $\mathcal{W}_A$, $\mathcal{W}_B$, their orientation relationship, and γ_{AB} are held constant, as the orientation of the AB interface is changed, the effective wetting angles vary and the energy of the particle varies (see Figure 2-11). It is possible for a particle to partially wet the interface for some orientations, and not wet the same interface for other orientations. Wulffmaker could thus be used to predict how much heterogeneous nucleation of a second phase to expect along grain boundaries as a function of orientation, or the distribution of nucleation sizes as a function of boundary orientation. This has implications not only for microstructure morphology, but also for microstructure development via Zener pinning. The critical nucleus will be smaller for particles nucleating in lower energy orientations, so they will be more numerous on a favorably-oriented interface. Additionally, the pinning force exerted by particles in a favorable orientation is stronger, resulting in a two-fold effect on grain boundary mobility. Even if the grain boundary itself is isotropic, the anisotropic particles that pin it will cause anisotropy in its mobility.

2.4 Conclusions

The double-Winterbottom construction determines equilibrium shapes of particles attached to deformable interfaces. This construction enables quantitative analysis of the stability of particles on deformable free interfaces and grain boundaries. Analysis of such particles in the general anisotropic case offers a new tool for the study of heterogeneous nucleation, Zener pining, and the study of devices made of isolated bodies on a substrate, such as electronic

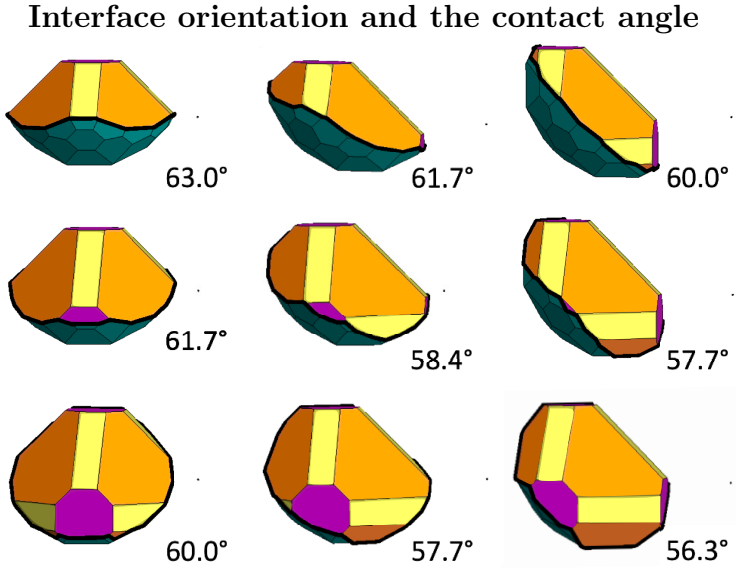

Figure 2-11: The dependence of contact angle on interface orientation is explored. $\mathcal{W}_A$, $\mathcal{W}_B$, their orientation relationship, and γ_{AB} are held constant, and only the interface orientation is changed. $\gamma_{AB} = \gamma_{PB} = 1$, $\gamma_{PA,[111]} = 0.9$, $\gamma_{PA,[100]} = 1.1$, and $\gamma_{PA,[110]} = 1$. The interface normal is tilted from [001] (top left) to [111] (bottom right), and the contact angle of the top half of the particle is shown with each image.

and optical devices.

Wulffmaker is a platform-independent software tool that enable fast, convenient calculation of Wulff, Winterbottom, and double-Winterbottom particle morphologies and associated energetic and geometric properties. This tool introduces a new computational method for finding shapes of minimal interface energy. It also helps to build intuition about the macroscopic properties of interfaces and their interactions, and aids in the quantitative measurement of interface energy densities, given a geometry. Properties such as the equivalent wetting angle, particle contact area, total energies, and distortions to the interface surrounding the particle are displayed by the software to enable further insight and analysis.

Chapter 3

The stability of a torus under capillary forces

3.1 Introduction

The stability of a cylinder under capillary forces is a well-known, classical problem. However, to our knowledge, the stability of a torus has never been reported. The case of a torus is of interest because it is closely-related to the "fingering instability," which occurs when a thin film dewets an underlying substrate. It has been suggested that the Rayleigh instability plays a role in driving the fingering instability [75, 40]. Knowledge of which wavelength perturbations should grow due to a Rayleigh instability can be used to determine what, if any, role a Rayleigh instability plays in the fingering process. However, knowledge of the Rayleigh instability on a cylinder is insufficent because thin film edges are often curved. The thickened rim on the edge of a circular island of thin film, or surrounding a growing hole, resembles a portion of a torus. The curved edge case is more common in dewetting experiments because thin films are finite in extent, evolving to an island geometry relatively quickly, and holes often form naturally. To interpret the fingering instability on curved film edges, it is necessary to understand the stability of a torus under capillary-driven surface tension.

3.1.1 Review of the Rayleigh instability on a cylinder

Under surface tension, a cylinder is a metastable shape. Determining whether such a cylinder will break-up into a spherical particles is a classical problem, first reported by Lord Rayleigh. His method for a stability analysis is as follows [67]:

1. Sinusoidally perturb the surface of the cylinder by replacing the radius r with $r_0(1 + \epsilon \cos kz)$, where r_0 is the mean radius, ϵ is the amplitude of the perturbation, k is the wavenumber of the perturbation, and z is the axial coordinate.

2. Find the surface area and volume of the perturbed cylinder as a function of r_0 and ϵ, to second-order accuracy in ϵ.

3. Apply volume conservation by equating the volume of an unperturbed cylinder of radius r_0 with the second order-accurate volume of the perturbed cylinder, and solve for r_0.

4. Determine whether the perturbation increases or decreases the total surface area of the cylinder. The sign of area change is the sign of the second-order term of the surface area, computed using the mean radius that enforces volume conservation, when expanded in ϵ. The value of k for which the surface area is unchanged is the critical wavenumber, k_{crit}.

His analysis yielded that k_{crit} is equal to 1. In other words, a sinusoidal perturbation of a wavelength longer than $2\pi r_0$ will reduce the total area of the cylinder. As the perturbation grows, the total area (and therefore total energy) decreases, ultimately breaking-up the cylinder into individual spheres.

To obtain which wavelength perturbation grows the fastest, Nichols and Mullins [58] calculated the perturbation growth rates when surface diffusion is the dominant transport mechanism. They obtained the result $\lambda_{fastest} = 2\sqrt{2}\pi r_0$.

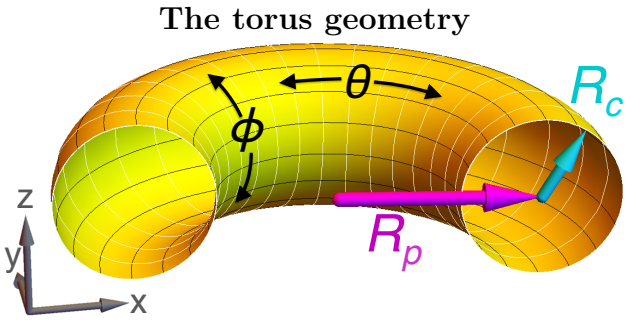

Figure 3-1: A cut-away view of a torus, $T(\theta, \phi, R_c, R_p)$, with θ, ϕ, R_c, and R_p defined on the image. The cartesian axes are shown in grey. R_c is the radius of the torus cross-section, and R_p is the radius of the torus in the xy-plane. The white mesh lines are curves with constant θ and $0 \leq \phi \leq 2\pi$, and the black mesh lines are curves with constant ϕ and $0 \leq \theta \leq 2\pi$. The image only shows half of the torus, $0 \leq \theta \leq \pi$.

3.2 The stability of a torus against capillary forces

3.2.1 Geometry

A torus is described by the parametric expression

$$T(\theta, \phi, R_c, R_p) = \Big((R_p + R_c \cos\phi) \cos\theta, (R_p + R_c \cos\phi) \sin\theta, R_c \sin\phi \Big), \tag{3.1}$$

with all parameters defined in Figure 3-1. In this chapter, lower-case r's refer to a variable, while upper-case R's refer to a particular, fixed value.

Four modes of sinusoidal perturbations were tested on the torus surface: perturb R_c in θ, perturb R_c in ϕ, perturb R_p in θ, and perturb R_p in ϕ. The stability analysis will only be shown in detail for the perturbation of R_c in θ, but the other three follow in the same fashion, the results of which are discussed in the subsequent subsection.

3.2.2 Possible perturbation wavenumbers

On a cylinder, there is no restriction on which wavenumbers are possible, because the geometry is not periodic. On a torus, only perturbations with an integer wavenumber $k = 1, 2, 3, ...$ fit exactly around the torus, in both the θ and ϕ directions.

However, non-integer k-values are not only possible, but probable. This is because perturbations usually originate at some point, and then propagate along the body if they grow,

rather than occurring everywhere simultaneously. Variations in the spacings between perturbation maxima would accommodate the mismatch if such a disturbance propagated all the way around the torus. As long as the spacings correspond to unstable wavelengths, the perturbations will continue to grow. Experimentally, it would be unsurprising to see multiple wavelength perturbations nucleate on the torus, with an intermediate spacing where they meet.

Perturbations with a k-value less than 1 are not possible on a torus. This is because a single wavelength cannot fit around the circumference of the torus, so it cannot be represented. The effect is similar to a Nyquist frequency: a perturbation with $k < 1$ is equivalent to some other perturbation with $k > 1$. For this reason, only results for $k \geq 1$ are considered. However, there is one exception: when $k = 0$, the torus is unchanged, so this mode is also possible.

3.2.3 Longitudinal perturbations

The torus is initially perturbed by replacing R_c in Equation 3.1 with $R_c(1 + \epsilon \cos k\theta)$, where ϵ is the perturbation amplitude and k is the wavenumber of the perturbation. The in-plane radius of the torus is held fixed at some value, R_p.

The surface area of the perturbed surface is

$$I = \sqrt{\frac{\partial T}{\partial \theta} \cdot \frac{\partial T}{\partial \phi}}, \tag{3.2}$$

$$A = \int_0^{2\pi} \int_0^{\frac{2\pi}{k}} \tilde{I} \; d\theta \; d\phi, \tag{3.3}$$

where I is the integrand to compute the surface area, A is the surface area over one wavelength, and $\tilde{I}$ is the Taylor series expansion of I to second order. This gives

$$A = \frac{4\pi^2 R_c R_p}{k} + \frac{\epsilon^2 k \pi^2 R_c^3}{\sqrt{R_p^2 - R_c^2}}. \tag{3.4}$$

The volume contained in one wavelength of the perturbation is found using the determinant of the Jacobian matrix. The components of the Jacobian matrix are $\frac{\partial T_i}{\partial j}$, where i is

the x, y, or z component of $\vec{T}$, and j is θ, ϕ, or r_c. If the perturbation in question was on r_p instead of r_c, then the derivatives in the Jacobian are with respect to θ, ϕ, and r_p. The determinant of the Jacobian for perturbations in r_c is $J = r_c(R_p + r_c \cos\phi)$. The volume of the perturbed torus segment is

$$V = \int_0^{R_c(1+\epsilon\cos k\theta)} \int_0^{2\pi} \int_0^{\frac{2\pi}{k}} J \; d\theta \; d\phi \; dr_c, \tag{3.5}$$

which evaluates to

$$V = \frac{2+\epsilon^2}{k}\pi^2 R_c^2 R_p. \tag{3.6}$$

The volume of the perturbed torus must equal the volume of the original torus. This puts a constraint on R_c. When V is set equal to a constant C and solved for R_c, it yields $R_c = \sqrt{C}/\left(\pi\sqrt{\frac{2+\epsilon^2}{k}R_p}\right)$. This value of R_c can be plugged into the expression for the surface area (Equation 3.4), and C is replaced with the volume of the unperturbed torus segment, $C = (1/k)2\pi^2 R_c^2 R_p$. This gives the surface area of the perturbed torus segment to be

$$A = 2\sqrt{2}\pi^2\left(2\sqrt{\frac{1}{(2+\epsilon^2)k^2}}R_c R_p + \frac{\epsilon^2 k R_c^3}{(2+\epsilon^2)\sqrt{(2+\epsilon^2)R_p^2 - 2R_c^2}}\right), \tag{3.7}$$

including the condition that the volume of this segment is equal to an unperturbed torus segment with the same value of R_p.

Equation 3.8 is equal to

$$A = \frac{4\pi^2}{k}R_c R_p + \left(\pi^2 R_c\Big(\frac{kR_c^2}{\sqrt{R_p^2 - R_c^2}} - \frac{R_p}{k}\Big)\right)\epsilon^2 + \mathcal{O}(\epsilon^3). \tag{3.8}$$

The sign of the second-order term determines whether the torus area increases or decreases due to the perturbation. The second-oder term is equal to zero when $k = R_c^{-1}(R_p^4 - R_c^2 R_p^2)^{1/4}$. Therefore, the critical wavelength for stability is

$$\lambda_{crit} = \frac{2\pi R_c R_p}{(R_p^4 - R_c^2 R_p^2)^{1/4}}. \tag{3.9}$$

This result is analogous to the classical Rayleigh result. In the limit $R_p \to \infty$, the critical

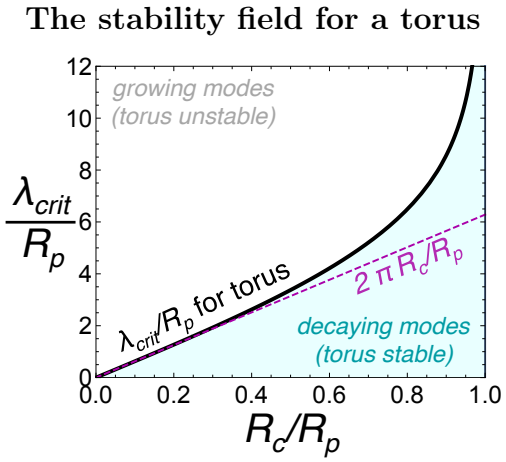

Figure 3-2: The critical perturbation wavelength for a torus (black curve) and for a cylinder (dashed magenta curve). The region below the stability curve (shaded cyan) corresponds to perturbations that decay away for a given value of R_c/R_p. In the limit that the torus approaches a cylinder (as $R_c/R_p \to 0$), the critical wavelength also approaches the cylinder behavior.

wavelength matches the classical result for a cylinder of radius R_c: $\lambda_{crit} = 2\pi R_c$. If λ_{crit} is re-written with $L_{crit} = \lambda_{crit}/R_p$, $r = R_c/R_p$, then

$$L_{crit} = \frac{2\pi r}{(1-r^2)^{1/4}}. \tag{3.10}$$

This format makes the comparison with the classical result clearer. A plot comparing the stability of a cylinder and a torus is provided in Figure 3-2.

3.2.4 Other perturbations

The same stability analysis can be performed for other perturbations. Perturbations in r_p always lead to increasing surface area, so the torus is stable against variations in the in-plane radius r_p.

If r_c is replaced by $R_c(1+\epsilon\cos k\phi)$, the torus takes on a "fluted" appearance. The second order term in the change of surface area is

$$(k^2-1)\pi^2 R_c R_p. \tag{3.11}$$

This indicates that the torus is stable against all perturbations with $k > 1$. The critical wavelength is $k = 1$. When $k = 0$, the torus surface is unchanged. Therefore, the torus its self is unstable. This result is unsurprising because the torus is an unstable surface under surface tension (unlike the cylinder, which is a metastable surface): the torus surface area can always decrease by decreasing R_p and commensurately increasing R_c to conserve volume. Thus, a torus is always driven to shrink and become a sphere.

There will be a competition between the Rayleigh instability and the "shrinking" instability. In some cases, the Rayleigh instability should outpace the shrinking rate of the torus. However, intuition suggests that for small torii, it would shrink away to a sphere before the Rayleigh instability has time to develop. It is not possible to derive the entire time evolution of the torus using a stability analysis; however, the magnitudes of the growth rates in each case can be computed to give some idea of which will dominate.

3.3 The fastest-growing perturbation on a torus

3.3.1 The Rayleigh instability

For perturbations of the same amplitude ϵ, the longer the wavelength, the larger the decrease in area of the torus. If mass transport is possible over long distances, such as via evaporation-condensation, then the longest-wavelength mode possible on a torus ($k = 1$ or, equivalently, $\lambda = 2\pi R_p$) will dominate the final shape, leaving a single sphere of material behind. However, for range-limited transport such as surface diffusion, the fastest-growing wavelength will be a compromise between the rate of mass transport and the driving force.

Find the surface of the torus after undergoing surface diffusion for a short time dt

The motion of a surface outward along its normal due to surface diffusion is given by Equation 1.8. The curvature of a parametric surface, $T(\theta, \phi)$, is given by

$$\kappa = \frac{EN - 2FM + GL}{2(EG - F^2)}, \tag{3.12}$$

where E, F, G, L, M, and N are the coefficients of the first and second fundamental forms:

$$E = \frac{\partial T}{\partial \theta} \cdot \frac{\partial T}{\partial \theta}, \tag{3.13}$$

$$F = \frac{\partial T}{\partial \theta} \cdot \frac{\partial T}{\partial \phi}, \tag{3.14}$$

$$G = \frac{\partial T}{\partial \phi} \cdot \frac{\partial T}{\partial \phi}, \tag{3.15}$$

$$L = \frac{\partial^2 T}{\partial \theta^2} \cdot \vec{n}, \tag{3.16}$$

$$M = \frac{\partial^2 T}{\partial \theta \partial \phi} \cdot \vec{n}, \tag{3.17}$$

$$N = \frac{\partial^2 T}{\partial \phi^2} \cdot \vec{n}, \tag{3.18}$$

and the normal vector to the surface, $\vec{n}$, is

$$\vec{n} = \frac{\frac{\partial T}{\partial \theta} \times \frac{\partial T}{\partial \phi}}{\| \frac{\partial T}{\partial \theta} \times \frac{\partial T}{\partial \phi} \|}. \tag{3.19}$$

The Laplace-Beltrami operator is found using a matrix containing the first fundamental forms:

$$A = \begin{pmatrix} E & F \\ F & G \end{pmatrix}, \tag{3.20}$$

$$\Delta_s = \frac{-1}{\sqrt{|\det A|}} \sum_{i,j=1}^{2} \frac{\partial}{\partial x_i} \Big((A^{-1})_{ij} \sqrt{|\det A|} \frac{\partial}{\partial x_j} \Big), \tag{3.21}$$

where x_1 is θ and x_2 is ϕ.

For an unperturbed torus, the expression $\Delta_s \kappa$ simplifies substantially:

$$\Delta_s \kappa = \frac{R_p \Big(R_p \cos\phi - R_c(-2 + \cos 2\phi) \Big)}{2(R_p + R_c \cos\phi)^5}. \tag{3.22}$$

For a sinusoidally-perturbed torus, the expression is cumbersome, and therefore not displayed here.

The surface of the torus, perturbed or otherwise, after undergoing surface diffusion for a

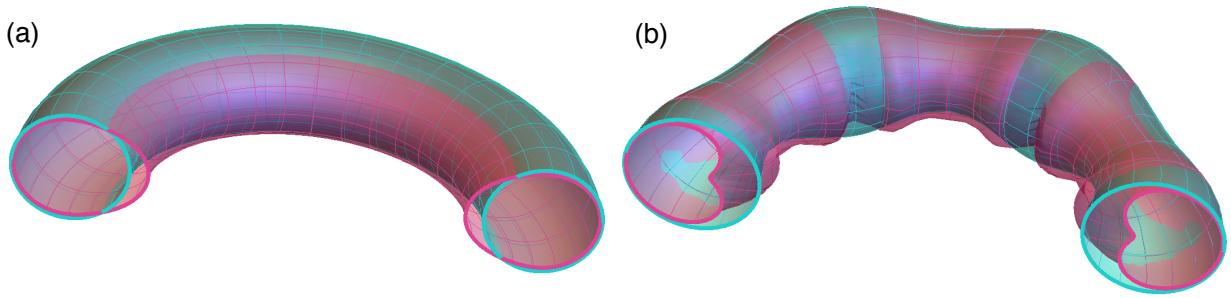

Figure 3-3: (a) an initially unperturbed torus with $R_c = 0.25$, $R_p = 1$, is shown in cyan. Only half of the torus is shown, for clarity. The effects of surface diffusion on the torus are shown in magenta. The amplitude of the shape change is exaggerated. (b) a torus with a sinusoidal perturbation of wavenumber $k = 6$ and amplitude $\epsilon = 0.2$ is shown in cyan. $R_c = 0.25$ and $R_p = 1$. The effects of surface diffusion on this surface are shown in magenta, with an exaggerated amplitude.

short time dt, becomes

$$T(\theta, \phi, dt) = T(\theta, \phi, 0) + (dt\, \Delta_s \kappa)\, \vec{n}, \tag{3.23}$$

where $T(\theta, \phi, 0)$ is the initial surface. The initial and final torii, for both the unperturbed and perturbed cases, are shown in Figure 3-3. To show how the torus evolves for different k values, top-down views are shown in Figure 3-4.

The perturbation growth rate

A schematic of a perturbed torus is shown in Figure 3-5. There are four points of interest on the surface. The velocity of the surface motion measured normal to the surface at these points, $v_{(\theta,\phi)} = (\Delta_s \kappa)\big|_{(\theta,\phi)}$, is used to measure the perturbation growth rate. Using the definitions provided in Figure 3-5, the Rayleigh perturbation growth rate is

$$\dot{\epsilon} = v_{(0,0)} + v_{(0,\pi)} - v_{(\pi/k,0)} - v_{(\pi/k,\pi)}. \tag{3.24}$$

Through non-dimensionalization, it can be found that $R_c^3 \dot{\epsilon}/\epsilon$ is only a function of R_p/R_c and k, and it does not depend on the amplitude ϵ, nor the characteristic length R_c. This version of the growth rate is shown in Figure 3-6 for different k values.

The places where the growth curves in Figure 3-6 cross the horizontal axis as the "critical"

Top-down views of perturbed torii with surface diffusion

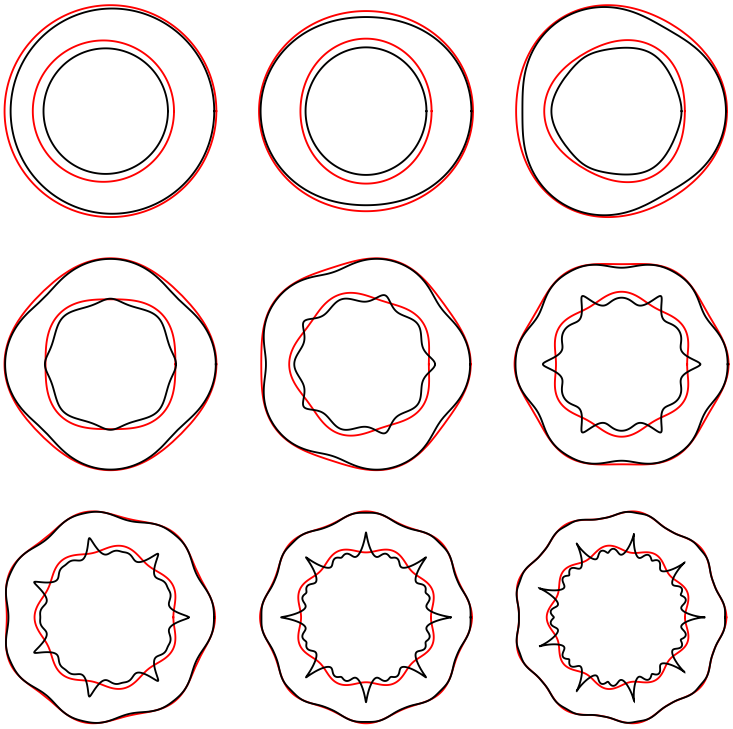

Figure 3-4: Perturbed torii are viewed top-down. The red curve is the original outline with $k = 1$ (top left) through 9 (bottom right), the torus parameters are $R_c = 0.2$ and $R_p = 1$, and the perturbation amplitude is $\epsilon = 0.2$. The black curve is the new surface after undergoing surface diffusion for a short time dt. The amplitude of the perturbation, dt, decreases with increasing k so the apparent amplitude of changes to the surface stays constant. For the $k = 1$ curve, $dt = 0.0045$, and for $k = 9$, $dt = 0.0003$.

The surface velocities used in the analysis

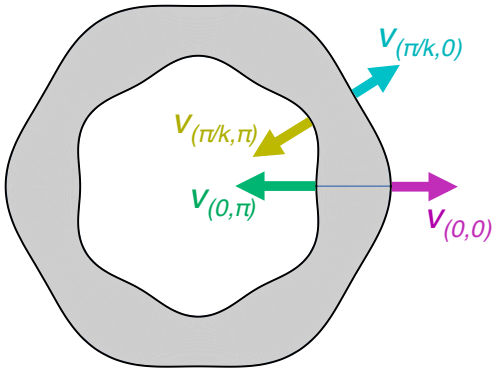

Figure 3-5: A top-down view of a perturbed torus is shown. The four arrows indicate the four surface velocities used to calculate the longitudinal perturbation growth rate. The subscript on the velocity denotes the coordinates of the point-of-interest on the surface, (θ, ϕ).

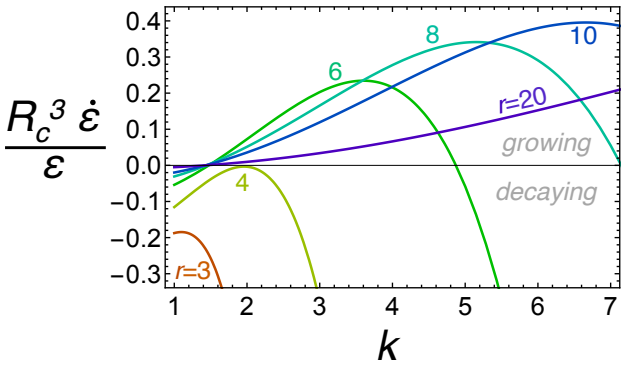

Figure 3-6: The growth rate of perturbations on a torus as a function of the wavenumber k is shown. Each curve is for a particular aspect ratio torus, $r = R_p/R_c$. These curves are independent of the amplitude ϵ and the magnitude of R_c or R_p. Torii with $r < 4.01$ have no growing perturbation modes, *i.e.*, they are stable against longitudinal perturbations.

wavenumbers, *i.e.*, perturbations which neither grow nor decay. The maximum of each curve is the fastest-growing perturbation. The wavenumber k is related to the wavelength λ by $\lambda = 2\pi/k$. The critical and fastest-growing wavelengths in the limit $\epsilon \to 0$ are plotted in Figure 3-7.

Figure 3-6 shows that for torii with an aspect-ratio greater than 4.01, there are two critical wavelengths (crossings of the x-axis). The lower critical wavelength behaves like the that of a cylinder, and is only slightly greater than $2\pi R_c$, as shown in Figure 3-7. The fastest-growing wavelength follows the lower critical wavelength behavior, again approaching the behavior of a cylinder. However, the upper critical wavelength is a property unique to the torus.

The $k = 1$ mode does not fall within the stability field for any torii, as shown in Figure 3-6. This means that a perturbation like that shown in the upper-left of Figure 3-4 will not grow under surface diffusion-limited kinetics. For torii with an aspect ratio less than 4.01, no perturbations grow, so these are completely stable against longitudinal perturbations, and will not undergo a Rayleigh instability.

If the perturbation amplitude ϵ has a finite value, a wider range of wavelengths are unstable. However, the difference between the $\epsilon \to 0$ map, shown in Figure 3-7, and the map for finite ϵ, is not significant unless $\epsilon > 0.1$. In the limit $\epsilon = 1$, the perturbations are so large that the torus is already broken up (*i.e.*, the cross-sectional radius of the torus is zero at the

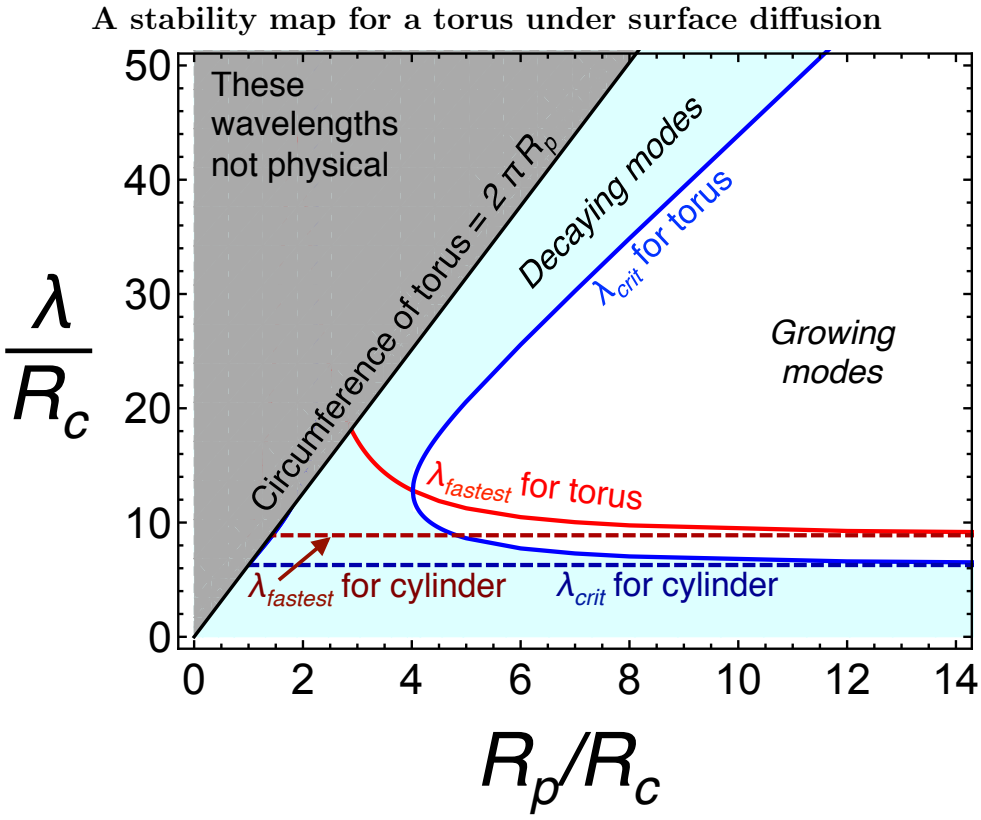

Figure 3-7: A stability map for a torus is shown. For a given perturbation of wavelength λ on a torus of aspect ratio $r = R_p/R_c$, the perturbation will grow if it falls in the white region of the map, and it decays if it falls in the shaded cyan part of the map. Wavelengths in the dark gray part of the map cannot fit at least one period on the torus, so they are not considered. The critical and fastest-growing wavelengths are shown for the torus, as well as for a cylinder.

minima). As ϵ approaches 1, the critical wavelength drops to 0, and above approximately $\epsilon = 0.5$, the $k = 1$ mode becomes unstable. In other words, any wavelength perturbation can grow if the amplitude is sufficiently large.

3.3.2 The shrinking instability

The rate at which a torus will shrink, *i.e.*, the rate of decrease of r_p, can be estimated using the unperturbed torus. This is because the unperturbed torus is already unstable, and because the perturbed torus exhibits complex three-dimensional shape changes, so it is difficult to choose a measure of the shrinking rate.

The difference between the surface-normal velocity measured at coordinates $(\theta, \phi) =$

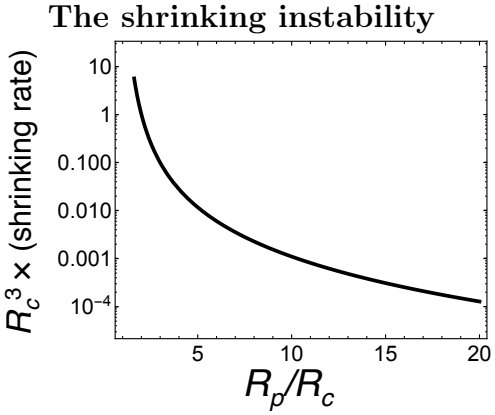

Figure 3-8: The total surface energy of a torus can always decrease by decreasing R_p and increasing R_c. Ultimately, it is driven to become a sphere. The rate at which R_p decreases is the shrinking rate, $\dot{r_p}$. This quantity is multiplied by R_c^3 so that it only depends on the ratio R_p/R_c, and it plotted on semi-log axes, above.

$(0, \pi)$ and the velocity at $(0, 0)$ (the positions of the green and pink arrows in Figure 3-5) on the unperturbed torus gives a measure of how fast r_p is decreasing. After simplification, this yields

$$\dot{r_p} = \frac{R_p(R_c^4 + 6R_c^2R_p^2 + R_p^4)}{(R_c - R_p)^4(R_c + R_p)^4}. \tag{3.25}$$

When $\dot{r_p}$ is multiple by R_c^3, the rate becomes independent of the specific values of R_c and R_p and only depends on the ratio R_p/R_c. This factor in needed because when the shrinking rate is non-dimensionalized, a factor of $1/L^3$ remains. R_c is chosen as the characteristic length, thus the multiplication removes the units. A dimensionless plot of the shrinking rate versus the R_p/R_c ratio is shown in Figure 3-8. The smaller R_p/R_c is initially, the faster the torus shrinks.

3.4 Conclusions

A perturbation analysis reveals that a torus with a high aspect ratio ($R_p >> R_c$) behaves much like a cylinder, being susceptible to break-up from longitudinal perturbations of sufficient wavelength. However, there is an upper limit to which wavelengths lead to instability, and the $\lambda = 2\pi R_p$ mode does not grow on torii. In addition, when R_p/R_c is less than 4.01, the torus is stabile against all perturbations.

Because the torus is an unstable geometry to begin with, it is subject to the "shrinking instability," where the torus moves towards a sphere by reducing R_p. The rate of shrinking increases dramatically as R_c approaches R_p.

Comparison of the Rayleigh and shrinking instabilities suggests that low aspect ratio (R_p/R_c value) torii shrink to become a single sphere, while higher aspect ratio torii undergo a Rayleigh instability first, and break-up into several spheres. Although it is not possible to say from this analysis at which aspect ratio the transition occurs, setting the growth rates of each instability equal to within an order of mangitude of each other and solving gives a transition of $R_p/R_c \approx 5 - 8$.

These results are applicable not only for an isolated body, but also for a ring of material undergoing dewetting. If the contact angle is 90°, then the symmetry of the ring resting on the substrate makes it identical to that of the isolated ring. The findings of this analysis could be verified using isotropic dewetting experiments.

The Rayleigh and shrinking instabilities on a torus provide a baseline for comparison with dewetting instabilities. The wavelength of the fastest-growing perturbation of a torus can be compared with the finger spacings on the edge of a growing hole or on a shrinking island of thin film to determine how much of a role the Rayleigh instability plays in the fingering morphology. If the wavelengths match, then the Rayleigh instability may be dominating the break-up. It also is clear from this analysis that if small islands or small holes have a dewetting shape instability, it is not related to Rayleigh break-up.

During dewetting, the shrinking instability should collapse small features into a single particle. The rate of collapse scales with $1/H^3$, where H is the film thickness, and the collapse rate is given by Figure 3-8.

Chapter 4

A 2D analytical model of dewetting

4.1 Introduction

One of the main features of dewetting is edge retraction. Although it has been shown that capillary-driven surface diffusion results in a thickened rim [75], it is not clear where mass is flowing, nor exactly how the retraction distance should scale with time. The time scaling is typically reported as a power-law, but there is mounting evidence that it is not so simple [96, 34, 85]. Having a reliable but simplified description of edge retraction would enable the development of models for more sophisticated phenomena, such as the corner and fingering instabilities.

Edge retraction was first recognized and studied by Brandon and Bradshaw [6]. They developed a simple model of hole growth with two key assumptions: the rim is a semi-circle, and all of the volume that has retracted away accumulates in the rim. The model predicts that the radius of a growing hole in a thin film will increase with time to the 2/5 power.

Experiments routinely agree with the 2/5 power-law time scaling at long retraction times [78, 34]. However, simulations show a more complicated picture. Kinetic Monte-Carlo simulations give a scaling with $t^{1/2}$ [8]. Numerical simulations of both isotropic and fully-faceted films initially retract linearly in time, and then the exponent in the power law gradually decreases, approaching 2/5 in the long-time limit [85, 96]. If edge retraction is not a simple power law, then the underlying cause of this scaling is unknown.

The B&B (Brandon and Bradshaw) model has two major limitations: it was developed

for a contact angle of 90° only, and the cross-section of the rim was taken to be a semi-circle. The first assumption limits the applicability of the model to different materials. The second assumption means that the model is only valid in the limit of long retraction times. Other phenomena such as pinch-off [85] or fingering instabilities [37] typically occur on thin film edges, which prevents the system from reaching the long-time limit of edge retraction in many cases.

In this chapter, an analytical model is presented, based on the B&B approach, which overcomes the limitations of the B&B model. The resulting model captures the transition from linear retraction to the 2/5 power-law behavior and offers an explanation for this phenomenology. The characteristic transition time from linear to 2/5 retraction and the retraction rate are also provided as a function of contact angle.

4.1.1 Basis for comparison: Brandon & Bradshaw's method applied to a straight edge

B&B developed their scaling law for a growing hole of radius r. Here, their method is repeated for an infinite, straight edge. This was done elsewhere [23], but there was an error in that analysis giving incorrect scaling. The straight-edge case will provide a basis for comparison with our model, discussed in the following sections. Their notation uses x as the rim height, r as the retraction distance, and d as the film thickness. However, we replace these with h as the rim height, x as the retraction distance, and H as the film thickness to be consistent with the coordinate system and definitions in our model.

The mass flux due to capillary forces is

$$J = -\frac{D_s}{kT}\frac{\partial \mu}{\partial s}\nu, \tag{4.1}$$

where D_s, k, and T are the diffusivity, Boltzmann's constant, and temperature, μ is the chemical potential, s is the arc length along the film surface with $s = 0$ at the triple line, and ν is the density of mobile atoms on the surface. For an isotropic surface, the chemical potential difference between the point at the triple line ($s = 0$) and for a flat film is estimated

as

$$\Delta\mu = -\Omega\gamma\frac{1}{h}, \tag{4.2}$$

where Ω is the atomic volume, γ is the surface energy density, and h is the rim height.

B&B assume that the arc width of the rim is $\Delta s = \pi h$; *i.e.*, the rim is a complete semi-circle in cross section. Assuming $\frac{\partial\mu}{\partial s} \approx \frac{\Delta\mu}{\Delta s}$, the flux can be approximated as

$$J = -\frac{D_s\Omega\gamma\nu}{kT\pi h^2}. \tag{4.3}$$

Consider a straight section of rim of length L. The total rate of transfer of material in this section, dV/dt, is $JL\Omega$. Therefore,

$$\frac{dV}{dt} = -\frac{D_s\Omega^2\gamma\nu L}{kT\pi h^2}. \tag{4.4}$$

Equation 4.4 is identical to B&B's Equation 11.

The cross-sectional area of the rim is approximately $\pi h^2/2$. The volume in this section of the rim is $L(\pi h^2/2)$. The volume of material that has been swept up due to retraction is LxH, where H is the film thickness and x is the retraction distance. Setting these two volumes equal gives a relationship between rim height h and retraction distance x:

$$\pi h^2 = 2Hx. \tag{4.5}$$

Substituting this relation into Equation 4.4 gives

$$\frac{dV}{dt} = -\frac{D_s\Omega^2\gamma\nu L}{kT2Hx}. \tag{4.6}$$

Equation 4.6 is analogous to B&B's Equation 13.

B&B assume that when viewed in cross-section, the area of material removed from the receding side of the rim and transferred to the advancing side is hdx, where dx is a small increment of retraction distance. The change in volume is therefore $dV = Lhdx$. Replacing

h using Equation 4.5 and dividing by dt yields

$$\frac{dV}{dt} = L\sqrt{\frac{2Hx}{\pi}}\frac{dx}{dt} \tag{4.7}$$

Equations 4.6 and 4.7 must be equal, so equating them and solving for dx/dt gives

$$\frac{dx}{dt} = \frac{D_s\Omega^2\gamma\nu}{2kTHx}\sqrt{\frac{\pi}{2fx}}. \tag{4.8}$$

Let $B = D_s\Omega^2\gamma\nu/(kT)$. Then

$$\frac{dx}{dt} = \frac{B\pi^{1/2}}{2^{3/2}H^{3/2}x^{3/2}}, \tag{4.9}$$

and integrating gives

$$x^{5/2} = \frac{5B\pi^{1/2}}{2^{5/2}H^{3/2}}t. \tag{4.10}$$

This differs from B&B's Equation 15 by a factor of $1/(2\sqrt{2})$, indicating that the radius of a hole should grow about 2.8 times faster than a straight edge should retract. Otherwise, the scalings are identical.

4.2 Model development

4.2.1 Geometry and assumptions

The following assumptions made in the B&B model are used in our model to simplify the rim geometry. The film is taken to be isotropic, and when cross-sectioned normal to the triple line, the rim profile is a circular arc which meets the substrate at the equilibrium contact angle θ. There is no valley on the film, and the discontinuity where the rim meets the film is artificial and therefore ignored in the analysis. It is also assumed that there is no mass flow between the flat film and the rim. The rim geometry is shown in Figure 4-1.

Two key differences from the B&B model are introduced: the allowance of any contact angle, and a more accurate treatment of the assumed geometry over time. While B&B take the cross-section of the rim to be a semi-circle, here it is treated as a circle that is cut along two perpendicular chords (see Figure 4-1). The horizontal cut determines the contact angle,

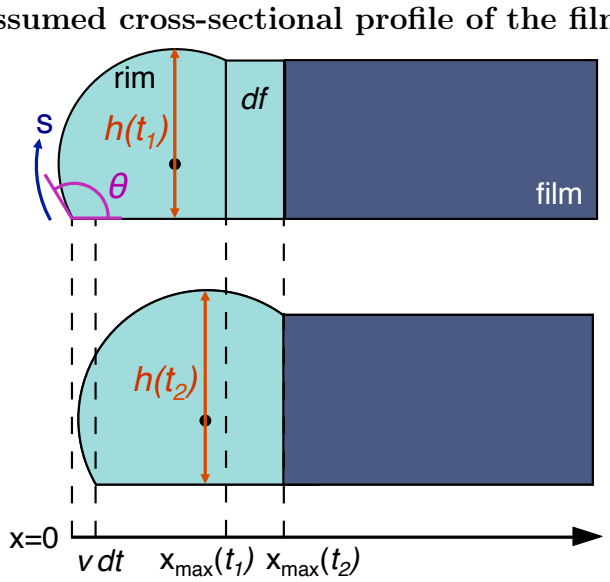

Figure 4-1: The cross-sectional profile of the edge of the film is shown at time $= t_1$ (top), and at time $= t_2 = t_1 + dt$ (bottom). Retraction proceeds at velocity v, which is a function of $h(t_1)$, for a short amount of time dt. The new film edge geometry can be found by assuming that the new rim area (light shading, bottom figure) is the sum of the old rim area plus the area df (light shading, top figure). The x-axis is drawn below the figures, and the positions used in the model are indicated. All length scales are normalized to the film thickness, and the contact angle θ and arc length coordinate s are shown on the top figure.

and the vertical cut ensures a match between the rim and bulk film, so that the rim and film volumes do not overlap. The vertical cut enforces volume conservation, which was lacking in B&B's model.

4.2.2 The retraction velocity as a function of rim height

All lengths in this analysis are normalized to the film thickness H so that all quantities are dimensionless. The height of the rim, h, is related to the rim's radius of curvature, r, and the contact angle, θ, by

$$r = \frac{h}{1 - \cos\theta}. \tag{4.11}$$

To compute the velocity of surface motion following Mullins [54] (see Section 1.4.1), the second derivative of curvature along the film profile is needed. However, the curvature along a circular arc is constant. To circumvent this issue, a finite-difference approximation is employed, similar to B&B's and Danielson's approach [6, 23]. The forward finite-difference

formula for a second derivative at the point $\kappa(s)|_{s=0}$, accurate to second order, is

$$\frac{\partial^2 \kappa}{\partial s^2} \approx \frac{\kappa(2\Delta s) - 2\kappa(\Delta s) + \kappa(0)}{\Delta s^2}, \tag{4.12}$$

where Δs represents a step size in the arc length coordinate. Δs is chosen to be the arc width of the rim,

$$\Delta s = r\Big(\theta + \arcsin \frac{x_{\max}(t_1) - r\sin\theta}{r}\Big), \tag{4.13}$$

and the value of $x_{\max}(t_1)$ is indicated in Figure 4-1. At the triple line, the curvature is equal to the curvature of the rim, $1/r$. At arc distance Δs and $2\Delta s$ from the triple line, the curvature is that of the flat film, 0. Substitution into Equation 1.8 using Equations 4.11 and 4.13, and projecting the normal motion into the plane of the substrate (*i.e.*, dividing by $\sin\theta$), yields

$$v_{retr} \approx \frac{\csc\theta(\cos\theta - 1)^3}{h^3(\theta + \arcsin\left(\frac{1}{h}\sin\left(\frac{\theta}{2}\right)\sqrt{2(h-1)(1+h+(h-1)\cos\theta)}\right))^2}. \tag{4.14}$$

4.2.3 The rim height as a function of time

The rim height at a future time, $h(t_2)$, is computed using conservation of mass within the rim. The old rim, with height $h(t_1)$, will incorporate material from the flat film with a cross-sectional area df, shown in Figure 4-1. This is the only way material is added to the rim. The cross-sectional area of the rim is found by integrating the curve that describes it from $x_{\min}$ to $x_{\max}$,

$$\mathrm{rim}(x) = \sqrt{r^2 - (r\sin\theta + x_{\min} - x)^2} - r\cos\theta, \tag{4.15}$$

where $x_{\min} = 0$ at time t_1 and $x_{\min} = v_{\mathrm{retr}}dt$ at time t_2. The additional volume in the rim where $x < x_{\min}$ if $\theta > 90°$ is also integrated and added. The area of flat film that is incorporated into the rim, df, is simply $(x_{\max}(t_2) - x_{\max}(t_1))$ (the film thickness is 1).

The cross-sectional area of the film is conserved, giving the equation

$$\text{rim area}(t = t_2) - \text{rim area}(t = t_1) - df = 0. \tag{4.16}$$

Upon substitution, this equation becomes transcendental, and cannot be used directly to solve for $h(t_2)$. Therefore, it is assumed that

$$h(t_2) = h(t_1) + \alpha v_{retr} dt, \tag{4.17}$$

where α is an unknown quantity. The left-hand side of Equation 4.16 can be linearized by expanding to first order in dt. The linearized equation is then solved for α, which describes the rim height as a function of time. The expression for α is lengthy, so it is not reproduced here. While α does depend on dt, the dependence is so weak that dt must be greater than about 10^7 to affect α by a percent. Therefore, dt is set to 1 inside α without loss of generality.

4.2.4 The retraction distance as a function of time

A differential equation for rim height $h(t)$ is given by

$$h'(t) = \alpha v_{retr}, \tag{4.18}$$

with the initial condition $h(0) = 1$. The solution to this equation does not have a closed form, but it can be integrated numerically without specialized algorithms. The numerical solution to $h(t)$ is substituted into Equation 4.14 and numerically integrated to yield the retraction distance of the film edge as a function of time. Using the built-in numerical differential equation solver and numerical integration function in *Mathematica 9* on a *ca.* 2011 laptop, the total time for the numerical work takes just a few seconds.

4.3 Discussion

The edge retraction distance versus time is shown in Figure 4-2. The guide lines show that initially, the slope of the curves is 1, and at late times, the slope is 2/5. On a log-log scale, these respectively correspond to the retraction distance being proportional to time t, and proportional to $t^{2/5}$. The constant of proportionality increases with contact angle. Also, the duration of the linear regime decreases with increasing contact angle. Considering the short

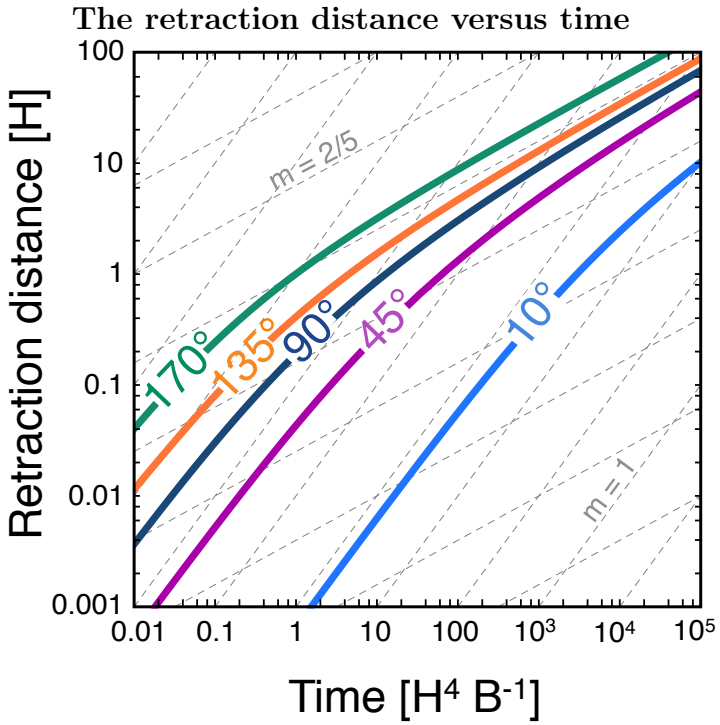

Figure 4-2: The retraction distance as a function of time is shown for various contact angles. The dashed gray lines are visual guides with slope $m = 2/5$ and slope $m = 1$. The distance and time are normalized using the film thickness H and material constant B.

and long time limits allows quantification of the constant of proportionality and the time it takes to transition from linear to power-law retraction.

4.3.1 Limiting behavior

The growth rate of the rim height is given by Equation 4.18. When the rim height is equal to the film height (time $\rightarrow 0$), the retraction velocity simplifies to $v_{\text{retr}} = -(\cos\theta - 1)^3/(\theta^2 \sin\theta)$. In this same limit, α goes to zero. Therefore, the rim initially does not grow in height, and the driving force for retraction is unchanged. However, the rim is incorporating mass, so it must be growing only in width. With constant driving force, the retraction distance is simply proportional to the total retraction time,

$$x(t \rightarrow 0) = -\frac{(\cos\theta - 1)^3}{\theta^2 \sin\theta} t. \tag{4.19}$$

In the limit of infinite time, the rim is very large, so $h >> 1$. The rim becomes a

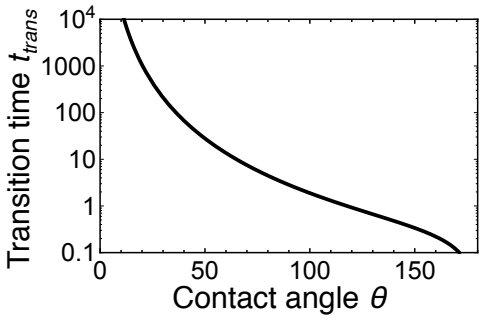

Figure 4-3: The time to transition from linear retraction to 2/5 power law retraction is shown as a function of contact angle. This curve corresponds to Equation 4.21. The time is normalized to H^4B^{-1}.

circular segment with cross-sectional area $\big(h/(1-\cos\theta)\big)^2\big(\theta-(1/2)\sin 2\theta\big)$. Setting the rim cross-sectional area equal to the swept-up film area, $1\times x$, gives an expression for the rim height h as a function of retraction distance x. With this geometry, the retraction velocity becomes $v_{\text{retr}} = -(\cos\theta-1)^3\csc\theta/(4h^3\theta^2)$. Replacing h with the expression for $h(x)$ yields $v_{\text{retr}} = \csc\theta(2\theta-\sin 2\theta)^{3/2}/(8\sqrt{2}\theta^2x^{3/2})$. Integration gives the final result that the retraction distance in the long time limit goes as $t^{2/5}$:

$$x(t\to\infty) = \frac{5^{2/5}}{2^{9/5}}\Big(t\frac{(2\theta-\sin 2\theta)^{3/2}}{\theta^2\sin\theta}\Big)^{2/5}. \tag{4.20}$$

This expression is analogous to the Brandon & Bradshaw result, but generalized for any contact angle, and with dimensionless units.

Finding the time when $x(t\to 0)$ equals $x(t\to\infty)$ gives an estimation of the transition time, t_{trans}, from linear to 2/5 power-law edge retraction. Setting Equations 4.19 and 4.20 equal yields

$$t_{\text{trans}} = (2\theta-\sin 2\theta)\frac{25^{1/3}\theta^2\sin\theta}{2^8\sin^{10}\left(\frac{\theta}{2}\right)}. \tag{4.21}$$

The transition time as a function of contact angle is plotted in Figure 4-3.

The retraction distance as a function of time is plotted for various contact angles in Figure 4-4. The dashed lines correspond to Equations 4.19 and 4.20, and show the extent to which the retraction curve deviates from the limiting behavior in the transition region. The black line is the transition time, Equation 4.21. For contact angles greater than about 10°,

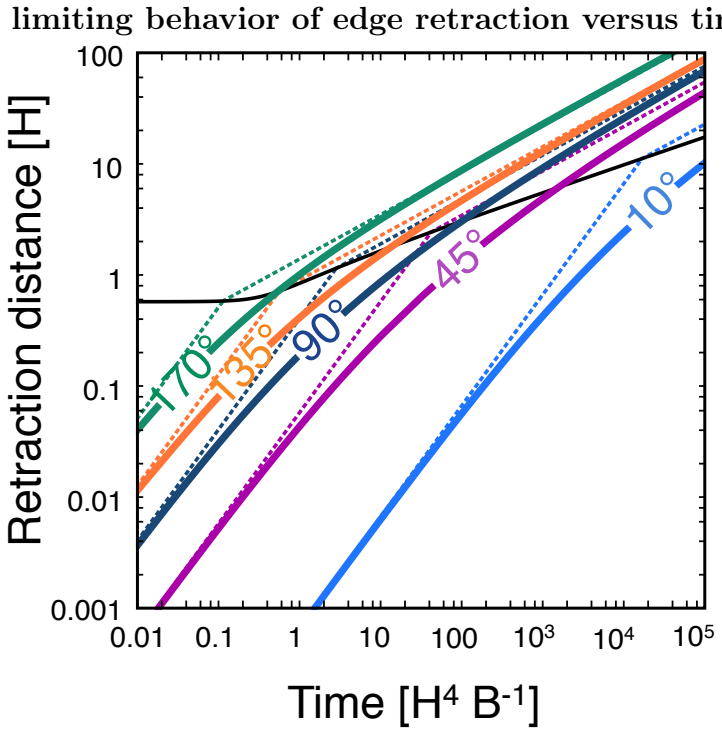

Figure 4-4: The retraction distance as a function of time (thick curve) is shown with the limiting behavior as $t \to 0$ (Equation 4.19) and $t \to \infty$ (Equation 4.20) (dashed lines) for various contact angles. The black curve is the transition time t_{trans} (Equation 4.21) for all contact angles.

the transition from linear to power-law retraction happens at a retraction distance of 0.8-8 times the film thickness, being shorter for larger contact angles.

4.3.2 Comparison with numerical simulations

The linear and 2/5 power-law regimes have been reported in the literature for isotropic [85] and fully-faceted [96] materials. Edge retraction curves for various contact angle are shown in Figure 4-5, with data lifted from references [85, 96]. The isotropic and fully-faceted simulations give identical retraction curves after non-dimensionalization, so a single curve represents the simulation results for each contact angle. Anisotropy plays no role in determining the edge retraction distance versus time. The simulations at $t < 1$ are not reliable because time steps must be extremely small to resolve retraction in this regime, and the edge retraction rate becomes sensitive to the starting configuration.

Qualitatively, the model and simulation curves are very similar, though the model under-

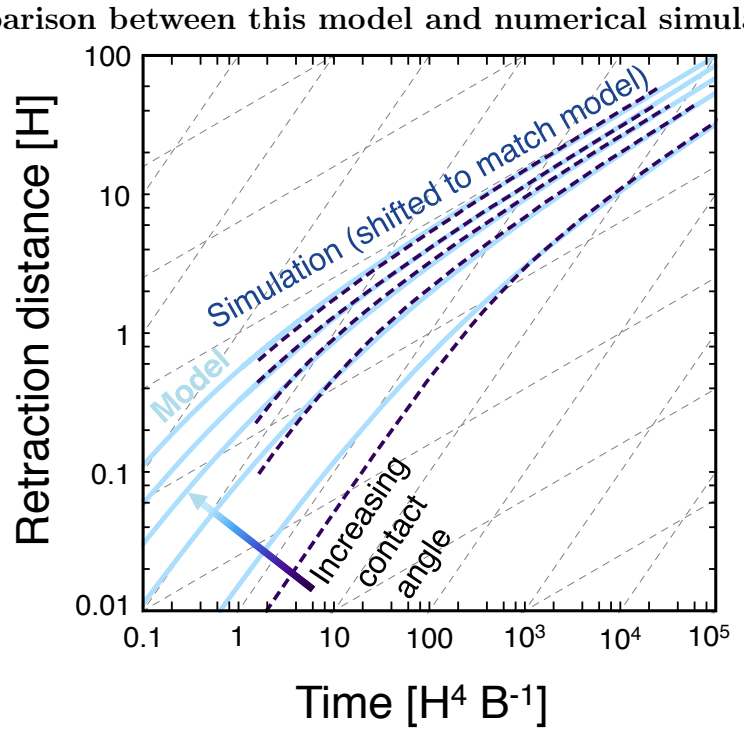

Figure 4-5: The retraction distance as a function of time for 30°, 60°, 90°, 120°, and 150° contact angles are shown for the model developed in this chapter (solid) and both isotropic [85] and fully-faceted [96] simulations (dashed). The isotropic and fully-faceted curves are completely overlapping, so they are shown as a single curve. The model and simulation curves have the same trend, but they are offset relative to each other. To enable comparison between the simulation and model curve shapes, the simulation 30°, 60°, 90°, 120°, and 150° contact angle curves were shifted down on the log-log log scale by 0.41, 0.38, 0.36, 0.34, and 0.25, respectively. This offset indicates different constants of proportionality in the best fit, but the scaling is the same: initially, edge retraction is linear in time, and follows a 2/5 power-law at late times. The unshifted simulation data can been seen in Figure 7-8.

estimates the retraction rate. If the simulation curves are shifted down by a constant on the log scale (as was done in Figure 4-5), then they follow the model curves closely. The transition from linear to 2/5 power-law retraction is also underestimated by the model, indicated by the simulation curves lying below the model curves in the linear regime.

4.4 Conclusions

The model presented here is extremely simple, but it reproduces the main features of dewetting, and explains the characteristic scalings. Initially, the rim is shaped like a quarter of a

circle. As mass is added to the rim, it initially grows in width, but not height. The driving force for retraction is not changing, and retraction proceeds linearly with time. At very late times, Brandon and Bradshaw's assumptions become valid, and the mass swept up is distributed evenly across a rim which is much taller than the film.

The transition time is very early for contact angles larger than about 45°. This explains why experiments often fail to detect the linear regime. For a typical metal, which often have contact angles near 90°, the transition time is on the order of a few seconds. However, it is worth noting that the exponent in the power-law model still takes some time to reach 2/5 to within measurable error. The fact that edge retraction is not a power law could be responsible for at least some of the error in fitting experimental data and its interpretation. It is more appropriate to fit edge retraction data to the model presented here.

Chapter 5

The Fingering Instability: a Stability Analysis of Retracting Thin Film Edges

5.1 Introduction

The fingering instability is introduced in Section 1.4.3. This instability leads to the formation of finger-like projections on a retracting film edge, as depicted in Figure 5-1. In this chapter, a morphological stability analysis is performed on the rim of a retracting thin film. Some geometric simplifications are made so that it is possible to do the analysis analytically. A perturbation is introduced, and the growth rate of the perturbation is calculated as a function of wavelength. The results are interpreted in the context of the three possible underlying mechanisms, which are defined in the following section. The analysis yields stability criteria, and offers insight into the causes of the fingering instability and how to control finger spacings.

5.2 Possible mechanisms of the fingering instability

The cause of the fingering instability is unknown. It has been suggested that the fingering instability is a Rayleigh-like instability of the rim [74, 40], or that it is analogous to the Mullins-Sekerka instability [28]. However, precise definitions for "Rayleigh-like" and "Mullins-

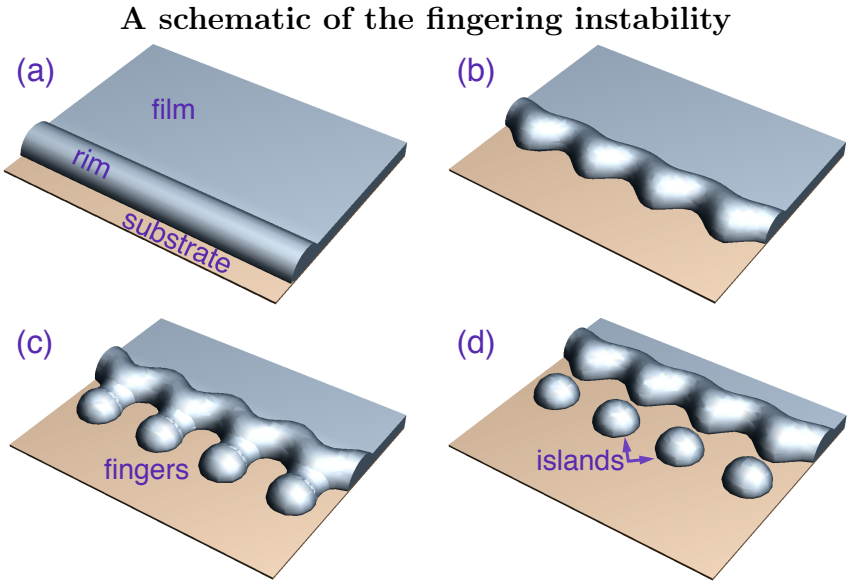

Figure 5-1: The progression from a straight, retracting rim to a fingering instability is drawn in (a) - (d). In (a), the film has just begin to retract and has formed a small rim. In (b), perturbations on the rim have grown into large-scale variations in triple line position and rim height. The thick parts of the rim retract slower, forming fingers as shown in (c). The fingers may become long before they break up into islands, as shown in (d). After islands break off from the fingers, the rim will look similar to figure (b), and the cycle repeats.

Sekerka like" instabilities are lacking. Therefore, definitions are presented here.

5.2.1 Rayleigh-like instability

The Rayleigh instability refers to the break-up of a cylinder into isolated spheres, driven by surface energy minimization [67]. A cylinder is unstable against perturbations if the wavelength of the perturbations is at least $2\pi r$, where r is the radius of the cylinder. The wavelength of perturbation that will grow fastest under surface diffusion, and therefore dominate the final state, is $2\sqrt{2}\pi r$ [59]. For longer wavelengths, the growth rate approaches zero.

For the edge-instability of a dewetting film, we define "Rayleigh-like" to be a shape instability that arises from mass transfer contained within the rim, with flux that is parallel to the triple line. Geometric quantities, such as the rim height $h(x)$, are defined in Figure 5-3. A perturbation to the rim height, $h(x)$, of sufficient wavelength should grow, and is driven by differences in mean curvature along the rim length, just as in the classical Rayleigh result. The mass flow that facilitates this instability is depicted in Figure 5-2(a).

Rayleigh break-up has been modeled for an isolated cylinder partially-wetting a substrate, analogous to the rim of a thin film [49]. Contact with a substrate can increase the minimum wavelength for break-up in some cases [49]. The question of whether a fingering instability could be initiated by a Rayleigh-like instability was tested by perturbing a numerically-obtained rim profile [40]. The resulting wavelength dependence qualitatively agrees with Rayleigh's results. However, their analysis is only valid for a stationary rim (or for late retraction times when the rim is very large), while fingering instabilities originate on rims at early times, when they are highly driven to retract.

5.2.2 Divergent retraction instability

The driving force for edge retraction is the gradient in mean curvature normal to the triple line. To first order, the mean curvature on the rim is $1/h(x)$, and the flat film has zero curvature. The distance from the triple line to the flat film is roughly $\pi/2h(x)$, so the gradient goes as $\big(h(x)\big)^{-2}$. Therefore, regions with a small rim will retract faster than regions with a large rim. The conditions under which variations in $h(x)$ produce a fingering instability in the triple line position $l(x)$ are determined below.

We define "divergent retraction" as a shape instability arising from variations in the edge retraction driving force. Divergent retraction is facilitated by mass transfer perpendicular to the triple line (*n.b.*, the Rayleigh instability is defined by parallel flow). A perturbation in $h(x)$ should give rise to differences in retraction rate, causing growing variations in $l(x)$. This instability is depicted in Figure 5-2(b).

5.2.3 Arc length instability

Isotropic edge retraction proceeds approximately normal to the triple line because this is the direction of maximum curvature gradient. However, a perturbation in the triple line position, $l(x)$, introduces additional curvature. As a section of triple line with negative in-plane curvature retracts, the arc length of the triple line must increase. An instructive example is a growing hole: the circumference of the hole increases with time, so the mass contained in the rim must be spread over a longer arc length, which will tend to decrease

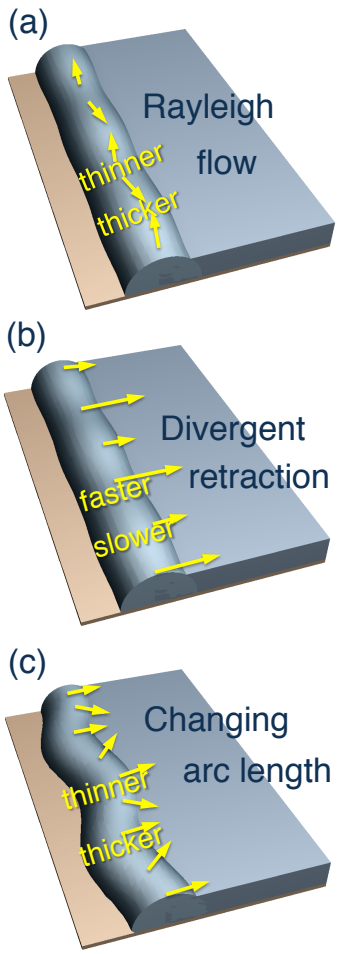

Figure 5-2: The mechanisms of instability are depicted. In each part of the figure, the film is retracting towards the right, exposing the underlying substrate. The perturbation amplitudes are exaggerated for emphasis. In (a), the arrows indicate the flux of mass for a Rayleigh-like instability on the rim. The rim will become thicker or thinner where indicated. In (b) and (c), the yellow arrows show retraction velocities. (b) shows that where the rim is thicker, it retracts more slowly. Likewise, the thinner rim retracts faster. The difference in retraction velocities gives rise to a divergent retraction instability. (c) shows that negatively-curved portions of the triple line are stretched due to retraction, leading to a thinner rim. Regions with positive triple-line curvature develop a thicker rim. The increasing variation in rim height is the changing arc length instability.

the rim height relative to the rim height of a straight rim. The opposite is true for sections of rim with a positive in-plane curvature: the arc length must decrease with retraction, so the rim thickens relative to a straight rim which has retracted the same distance.

The "changing arc length instability" refers to a perturbation in the triple line position, $l(x)$, giving rise to variations in the rim height $h(x)$. This instability derives from volume conservation within the rim, and is depicted in Figure 5-2(c).

This type of instability could be construed as analogous to the Mullins-Sekerka instability [56]. The Mullins-Sekerka instability occurs during solidification and leads to cellular or dendritic solid/liquid interfaces. The solid/liquid interface propagates towards the liquid, and a protuberance on the interface will be affected by two competing effects. It has increase surface area (positive curvature), and latent heat is rejected to a larger volume of liquid. This increases the thermal gradient at the interface and enables the liquid near the protuberance to solidify faster than that near a straight interface. However, increased surface energy penalizes the formation of shorter-wavelength perturbations, resulting in a characteristic wavelength. The run-away solidification of the protuberance leads to a cellular interface.

In the case of dewetting, the substrate/film interface is propagating toward the film at the retraction velocity. If the triple line protrudes into the unstable film, the film edge has negative curvature and the rim material is spread over a longer arc length. This decreases the protuberance's rim height relative to a straight rim and drives the protuberance to dewet faster than a straight interface. The run-away dewetting of the protuberance leads to a finger-like morphology. The rim height is analogous to the thermal gradient in the Mullins-Sekerka instability. However, unlike the Mullins-Sekerka instability, there is no competing effect that eliminates the smaller wavelengths.

5.2.4 The combined effect of the three instabilities

The instability mechanisms have been described independently. However, the rim's height and triple line are geometrically coupled, and the instabilities interact in a non-linear fashion. Although they cannot be separated, considering their individual effects helps to interpret the result of the stability analysis.

These instabilities will effectively compete with one another. For example, the Rayleigh-like instability suppresses short wavelength perturbations, while the changing arc length instability promotes them. Likewise, divergent retraction tends to suppress variations in rim height, while the other two instabilities promote rim-height variations. Independent stability analyses will reveal which instability dominates.

5.3 Methods

5.3.1 Geometry and assumptions

We treat an initially-straight edge of an isotropic film. The film is infinite in the x-direction, semi-infinite in the y-direction, and has finite thickness in the z-direction, as shown in Figure 5-3. All lengths in the analysis are normalized to the film thickness. At the film edge, a small rim exists with mean height η above that of the flat film, so that the total height of the rim is $1 + \eta$. In a cross-section normal to the triple line, the rim profile is a circular arc that intersects the substrate with contact angle θ.

The rim height is perturbed sinusoidally with amplitude ϵ. The rim height is taken to be $h(x) = (1 + \eta) + \epsilon(1 - \cos kx)$, where k is the wavenumber of the perturbation. This perturbation also leads to a perturbation of the triple line position, $l(x) = y_0 + \frac{\epsilon}{\sin\theta}\cos kx$, where y_0 is the mean triple line position. Throughout the analysis, both the rim height $h(x)$ and triple line position $l(x)$ are considered to be susceptible to instability.

In the model, there is no valley (*i.e.*, the film is not thinned) between the rim and the bulk film. This assumption is justified by the valley depth always being small compared to the rim height [75, 85], so the curvature gradients produced by the valley should be negligible.

In the analysis, the x-coordinate is used interchangeably with the arc length coordinate s_1, as defined in Figure 5-3. This "small-perturbation" approximation should be valid when slopes are small, *i.e.*, for small perturbations.

It is assumed that all of the rim's mass increase comes from retraction; there is no mass transfer between the rim and bulk film. This assumption is consistent with numerical simulations which show that the total mass flux between the rim and the film is small

The assumed geometry of the rim

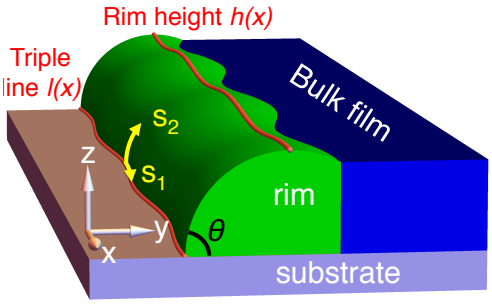

Figure 5-3: The cartesian coordinates, x, y, z, and arc length coordinates, s_1 and s_2, are shown with a perturbed rim. Curves indicate the rim height $h(x)$ and triple line position $l(x)$. The contact angle θ is measured inside the material.

compared to the flux within the rim [85, 96].

The assumption that the rim cross-section is a circular arc should not significantly influence the rim stability. McCallum *et al.* [49] and Kan & Wong [40] found that instability conditions do not have a strong dependance on rim cross-section.

The two-dimensional model presented in the previous chapter incorporates very similar assumptions. The main difference is that in this chapter, the rim is 3D, not 2D, and further effort must be made to capture the additional dimension. The 2D model's success in capturing the dynamics of edge retraction suggests that this simplified geometry captures the essential physics of thin film kinetics.

5.3.2 The triple line perturbation growth rate, GR_{TL}

The retraction velocity

The retraction velocity of the triple line is

$$v_{\text{retr}} = \frac{1}{\sin\theta}\, v_n\big|_{s_1=l(x),s_2=0}, \tag{5.1}$$

where v_n is the dimensionless capillary-driven surface diffusion normal velocity, defined in Equation 1.8. v_{retr} is the projection of the normal velocity into the plane of the substrate.

The goal of this section is to find v_{retr} by computing $\frac{\partial^2 \kappa}{\partial s_1^2}\big|_{s_1=l(x),s_2=0}$ and $\frac{\partial^2 \kappa}{\partial s_2^2}\big|_{s_1=l(x),s_2=0}$ from the prescribed geometry.

An expression for $\kappa(l(x),0)$ in needed. Consider the curvature in the s_1 direction. The axis of symmetry of the rim is taken to be at $y=0$. The small-perturbation approximation allows the s_1 coordinate to be replaced with the x-coordinate. The triple line position $l(x)$ is the intersection of the rim and the substrate:

$$\sqrt{r(x)^2 - l(x)^2} - r(x)\cos\theta = 0 \tag{5.2}$$

$$l(x) = -\sqrt{-h(x)^2 + \frac{2\,h(x)^2}{1-\cos\theta}}. \tag{5.3}$$

The negative square root is chosen because the rim is centered on $y=0$, and the bulk film lies on the positive y side of the rim. The second derivative of the triple line position, $\frac{\partial^2 l(x)}{\partial x^2}$, gives the curvature of the triple line. Next, consider the s_2 coordinate. The rim profile is taken to be a circular arc, so the curvature is $1/r(x)$. The radius of curvature of the rim, $r(x)$, is

$$r(x) = \frac{h(x)}{1-\cos\theta} = \frac{1+\eta+\epsilon(1-\cos kx)}{1-\cos\theta}. \tag{5.4}$$

Summing the curvatures in the s_1 and s_2 directions gives the mean curvature of the rim along the triple line:

$$\kappa\big(x,0\big) \approx \frac{\cos\theta - 1}{1+\eta+\epsilon(1-\cos kx)} + \epsilon k^2 \cos kx \cot\frac{\theta}{2}. \tag{5.5}$$

The second derivatives of the mean curvature must be computed to obtain the retraction velocity. $\frac{\partial^2 \kappa}{\partial s_1^2}$ is simply $\frac{\partial^2 \kappa(x,0)}{\partial x^2}$, due to the small-perturbation approximation. $\frac{\partial^2 \kappa}{\partial s_2^2}$ must be obtained indirectly because κ has no explicit dependence on s_2, due to the assumption that the rim is a circular arc. A forward finite-difference scheme is used to estimate $\frac{\partial^2 \kappa}{\partial s_2^2}$, just as in the previous chapter:

$$\frac{\partial^2 \kappa}{\partial s_2^2} \approx \frac{\kappa(s_1, 2\Delta s_2) - 2\kappa(s_1,\Delta s_2) + \kappa(s_1,0)}{(\Delta s_2)^2}, \tag{5.6}$$

where Δs_2 is the arc length from the triple line to the point where the rim and flat film

meet. Δs_2 is found using the known geometry of the rim. $\kappa(s_1, 0)$ is the curvature at the triple line, given by Equation 5.5. $\kappa(s_1, \Delta s_2)$ is the curvature of the film just beyond the point where the rim and film meet, and $\kappa(s_1, 2\Delta s_2)$ is the curvature measured even further into the flat region. Therefore, $\kappa(s_1, \Delta s_2)$ and $\kappa(s_1, 2\Delta s_2)$ are equal to zero. Equation 5.6 becomes

$$\frac{\partial^2 \kappa}{\partial s_2^2} \approx \frac{\kappa(x,0)}{(\Delta s_2)^2} = \frac{(\cos\theta - 1)^2 \left(\frac{1-\cos\theta}{1+\eta+\epsilon-\epsilon\cos kx} - \epsilon k^2 \cos kx \cot\frac{\theta}{2}\right)}{\left(\theta + \arctan \frac{(1-\cos\theta)\sqrt{\frac{(\eta+\epsilon-\epsilon\cos kx)(2+\eta+\epsilon-\epsilon\cos kx+\cos\theta(\eta+\epsilon-\epsilon\cos kx))}{1-\cos\theta}}}{1+\cos\theta(\eta+\epsilon-\epsilon\cos\theta)}\right)^2 (1+\eta+\epsilon-\epsilon\cos kx)^2} \tag{5.7}$$

The triple line perturbation growth rate, $\mathbf{GR_{TL}}$

With expressions for $\frac{\partial^2 \kappa}{\partial s_1^2}$ (the second derivative with respect to x of Equation 5.5) and $\frac{\partial^2 \kappa}{\partial s_2^2}$ (Equation 5.7), the retraction velocity is obtained by substitution into Equation 5.1. The triple line perturbation growth rate is

$$\mathrm{GR_{TL}} = \vec{v}_{\mathrm{retr}}|_{x=0} - \vec{v}_{\mathrm{retr}}|_{x=\pi/k}. \tag{5.8}$$

This is a measure of how quickly the thin part of the rim retracts, relative to the thick part of the rim. $\mathrm{GR_{TL}}$ is plotted in Figure 5-5.

5.3.3 The rim height perturbation growth rate, $\mathbf{GR_{RH}}$

The change in rim height with time

The mass swept up by the advancing rim during retraction must be incorporated into the rim. Knowledge of the mass incorporated via retraction, along with any flows contained within the rim, allows the change in rim height, $dh(x)$, to be calculated as a function of retraction distance, $dl(x)$. The geometry and definitions are shown in Figure 5-4. The crux of this calculation is satisfying the condition of volume conservation.

The equation for $\frac{dh(x)}{dl(x)}$ is continuous, but it is useful to think about a short section of the rim of arc width s with uniform curvature. This section of rim initially has volume V_{r1}. After edge retraction for a distance $dy = v_{\mathrm{retr}} dt$, the rim section has volume V_{r2}.

The volume of the rim is

$$V_{\mathrm{r}} = \frac{s}{R(x)} \int_{y_{\mathrm{LB}}}^{y_{\mathrm{UB}}} y(\sqrt{r(x)^2 - (R(x) - y)^2} - r(x)\cos\theta)\, dy, \tag{5.9}$$

Where the multiplication by y makes this the expression for a volume of revolution. This can be imagined as finding the volume of a portion of a torus. $r(x)$ is the local radius of rim curvature, and $R(x)$ is the radius from the axis of revolution to the midpoint of the torus, which is $1/l''(x) + r(x)\sin\theta$ for a negative in-plane curvature, and $1/l''(x) - r(x)\sin\theta$ for positive in-plane curvature. y_{LB} and y_{UB} are where the rim intersects the substrate and bulk film, respectively, for negative in-plane creature, and vice-versa for positive in-plane curvature, as indicated in Figure 5-4.

The volume of the bulk film that is incorporated during retraction is equal to

$$V_{\mathrm{f}} = \frac{s}{2}(y_{\mathrm{UB2}}^2 - y_{\mathrm{UB1}}^2). \tag{5.10}$$

All of the volumes can be expressed in terms of: the rim height before retraction ($h_1(x)$), the rim height after an increment of retraction ($h_2(x)$), the retraction distance ($dl(x)$), the contact angle (θ), the perturbation amplitude (ϵ), and the perturbation wavenumber (k). Sufficiently small retraction distances can be linearized in time: $dl(x) = v_{\mathrm{retr}}dt$. In the volume expressions, dependance on $dl(x)$ can therefore be replaced by dependance on dt. Furthermore, the new rim height, $h_2(x)$, can be re-expressed as $h_1(x) + \alpha(x)\, dl(x)$, where α is an unknown function. To solve for α at a given place on the rim, the volume expression,

$$dV = V_{\mathrm{r2}} - V_{\mathrm{r1}} - V_{\mathrm{f}}, \tag{5.11}$$

is expanded to first order in dt. The linearization is necessary to obtain a result which is not transcendental. By comparison with numerically-obtained solutions to $dV = 0$, the linearization introduces negligible error. The first-order approximation to dV, $dV^{(1)}$, is then set equal to zero and solved for α.

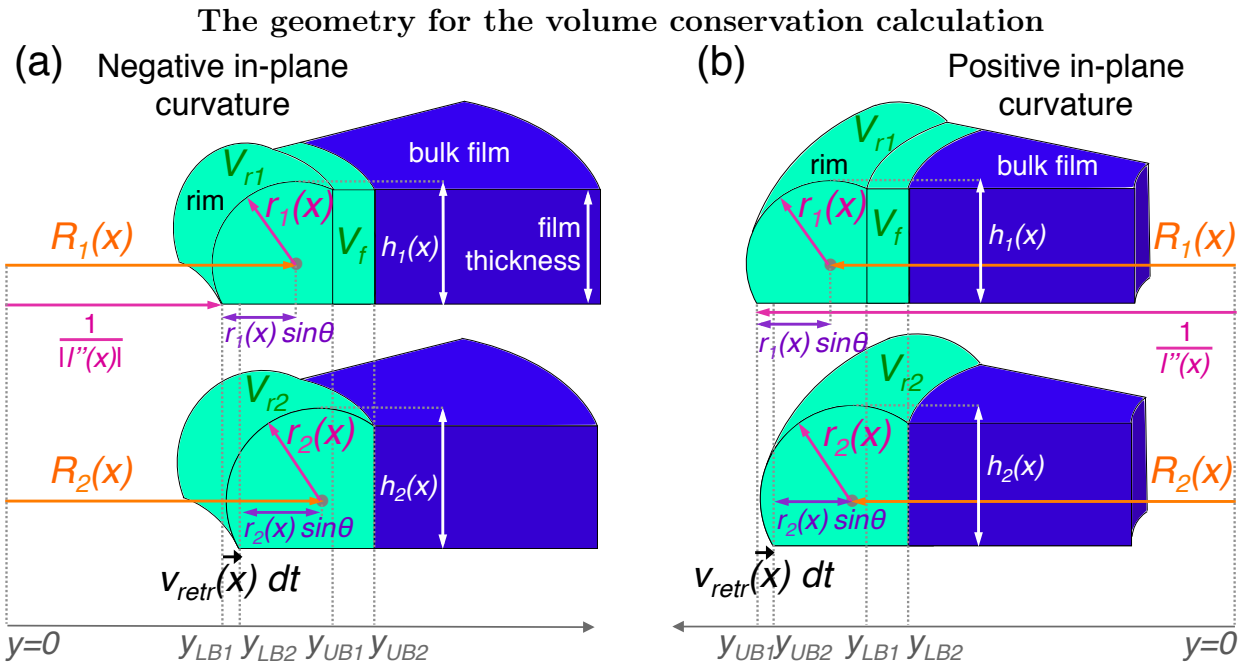

Figure 5-4: The geometry for the volume conservation calculation is shown. The edge of the film may have non-zero in-plane curvature, $l''(x)$. The top part of each diagram, with subscript 1, is the starting geometry, which is prescribed by the applied perturbation. The bottom part of each diagram, with subscript 2, is the geometry after a small increment of edge retraction, $dl(x) = v_{\text{retr}}(x)dt$. The goal is to find $h_2(x)$. The radial coordinate, y, is shown at the bottom of each diagram, and y-values for Equations 5.9 and 5.10 are indicated.

The rim height perturbation growth rate, $\mathbf{GR_{RH}}$

In time dt, the edge retracts a distance $dl(x) = v_{\text{retr}}(x)dt$. The rim height increases in this time by an amount $\alpha(x)dl(x)$. Therefore, the rate of rim height increase with time is $\alpha(x)v_{\text{retr}}(x)$.

The growth rate of perturbations to the rim height, GR_{RH}, is the growth rate of the thick part of the rim, minus the growth rate of the thin part of the rim:

$$\text{GR}_{\text{RH}} = \Big(\alpha(x)\, v_{\text{retr}}(x)\Big)\Big|_{x=\pi/k} - \Big(\alpha(x)\, v_{\text{retr}}(x)\Big)\Big|_{x=0}. \tag{5.12}$$

The perturbation growth rate depends only on ϵ, θ, and k. GR_{RH} is plotted in Figure 5-5.

5.3.4 The perturbation growth rates for the three instabilities

The Rayleigh-like instability is defined to arise from mass flow parallel to the triple line. Therefore, the perturbation growth rate due to the Rayleigh-like instability in the absence of the other effects is

$$\text{GR}_{\text{Rayleigh-like}} = \frac{1}{\sin\theta}\Big(\frac{\partial^2\kappa}{\partial s_1^2}\Big|_{x=0,s_2=0} - \frac{\partial^2\kappa}{\partial s_1^2}\Big|_{x=\pi/k,s_2=0}\Big). \tag{5.13}$$

This expression is similar to GR_{TL}, defined in Equation 5.8, except that the contribution from mass flow normal to the triple line has been dropped. The $1/\sin\theta$ term is present for same reason it occurs in Equation 5.1 - it projects the velocity normal to the surface into the plane of the substrate.

The divergent retraction instability arises from the mass flow normal to the triple line, within the rim:

$$\text{GR}_{\text{Divergent retraction}} = \frac{1}{\sin\theta}\Big(\frac{\partial^2\kappa}{\partial s_2^2}\Big|_{x=0,s_2=0} - \frac{\partial^2\kappa}{\partial s_2^2}\Big|_{x=\pi/k,s_2=0}\Big). \tag{5.14}$$

This expression compares the retraction rate at the thick part of the rim with the retraction rate at the thin part of the rim. The definition is similar to GR_{TL} (Equation 5.8), but in this case there is no flux parallel to the rim.

The changing arc length instability arises only from the motion of the triple line, and does not require long-range diffusive mass transport. Its behavior can be studied in the absence of the other instabilities by computing $\mathrm{GR}_{\mathrm{RH}}$, given by Equation 5.12 which includes all three effects, without the differences in height along the rim. With no differences in rim height, the Rayleigh-like and divergent retraction instabilities cannot operate. Thus, the effects of the changing arc length instability are described by

$$\mathrm{GR}_{\text{changing arc length}} = \Big(\alpha(x)\, v_{\mathrm{retr}}(x)\Big)\Big|_{h(x)=1+\eta,\, \kappa(x)=+\epsilon k^2} - \Big(\alpha(x)\, v_{\mathrm{retr}}(x)\Big)\Big|_{h(x)=1+\eta,\, \kappa(x)=-\epsilon k^2}. \tag{5.15}$$

5.4 Results and discussion

5.4.1 Properties of the perturbation growth rate

The two perturbation growth rates that define the fingering instability, $\mathrm{GR}_{\mathrm{TL}}$ and $\mathrm{GR}_{\mathrm{RH}}$, are shown in Figure 5-5. All plots use the wavelength λ instead of the wavenumber k, with $\lambda = 2\pi/k$. Generally, small wavelength perturbations decay (*i.e.*, have a negative growth rate), and long wavelength perturbations grow. Additionally, the amplitude of the perturbation growth rate scales with $\sqrt{\epsilon}$; *i.e.*, the larger the perturbation, the faster it grows (or decays). Figure 5-5 also shows that the perturbation grows 3-4 times faster on top of the rim than at the triple line.

In the limit of long wavelengths, the growth rates approach non-negative, finite values. These values are shown as a function of contact angle in Figure 5-6. Scaling the growth rates by $1/\sqrt{\epsilon}$ reveals limiting behavior as ϵ goes to zero. The higher the contact angle (*i.e.*, the higher the interfacial energy between the film and substrate), the faster the instability grows.

The wavelength at which GR = 0 is the critical wavelength, $\lambda_{\mathrm{critical}}$. Only wavelengths greater than $\lambda_{\mathrm{critical}}$ can grow. The perturbation with the largest growth rate (*i.e.*, the λ at which $\frac{\partial}{\partial\lambda}(\mathrm{GR}) = 0$) is $\lambda_{\mathrm{fastest}}$. $\lambda_{\mathrm{critical}}$ and $\lambda_{\mathrm{fastest}}$ are plotted in Figure 5-7.

The fastest-growing wavelength is not sensitive to the value of ϵ, so a single curve is shown in Figure 5-7. However, the critical wavelength nearly matches the Rayleigh-like instability

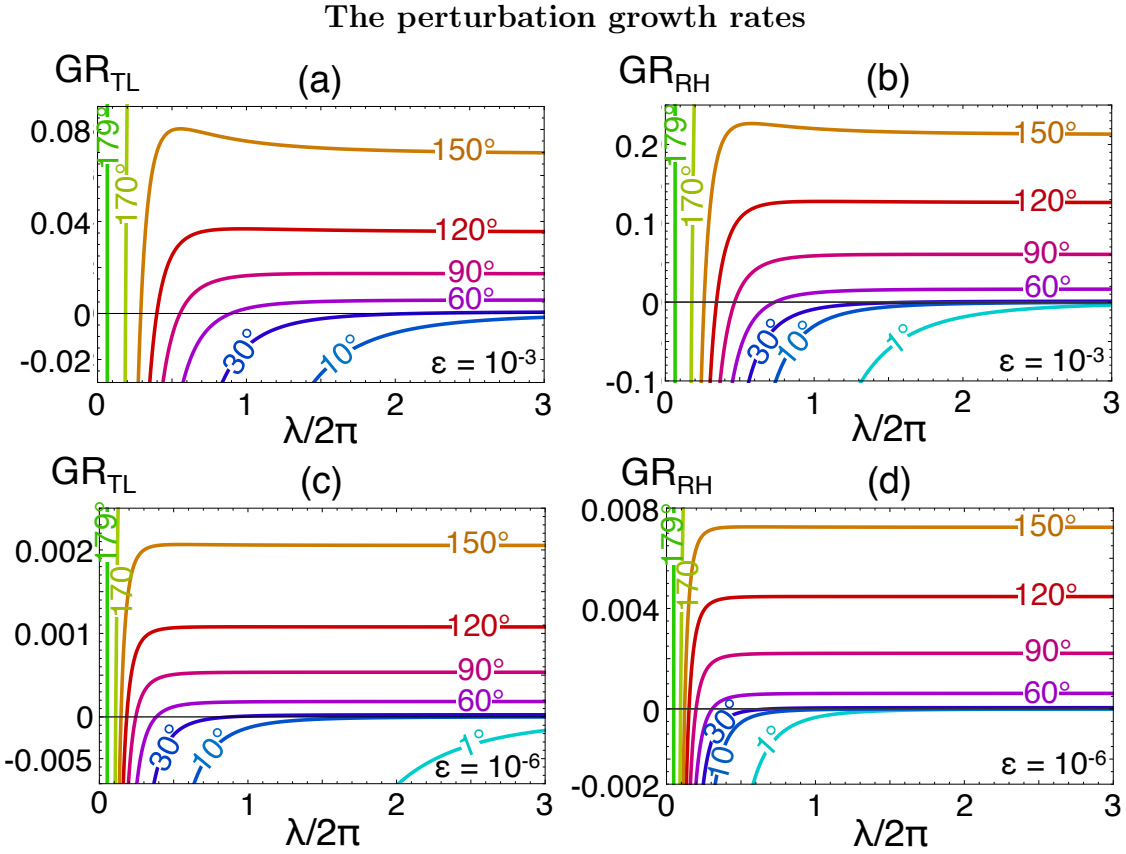

Figure 5-5: The perturbation growth rates for different values of θ and ϵ are shown. The horizontal axis is the perturbation wavelength, normalized to the film thickness and divided by 2π, with $\lambda/2\pi = 1/k$. The vertical axis is the perturbation growth rate on the triple line (TL) in figures (a) and (c), and the rim height (RH) in (b) and (d). Each curve is labeled with the corresponding value of the contact angle θ. In figures (a) and (b), $\epsilon = 10^{-3}$, and in figures (c) and (d), $\epsilon = 10^{-6}$. Where GR > 0, the perturbation will grow. In all four cases, the shape of the 170° and 179° curves is the same as the smaller contact angles, but the magnitude is too large to show on the same axes.

Perturbation growth rates in the long-wavelength limit

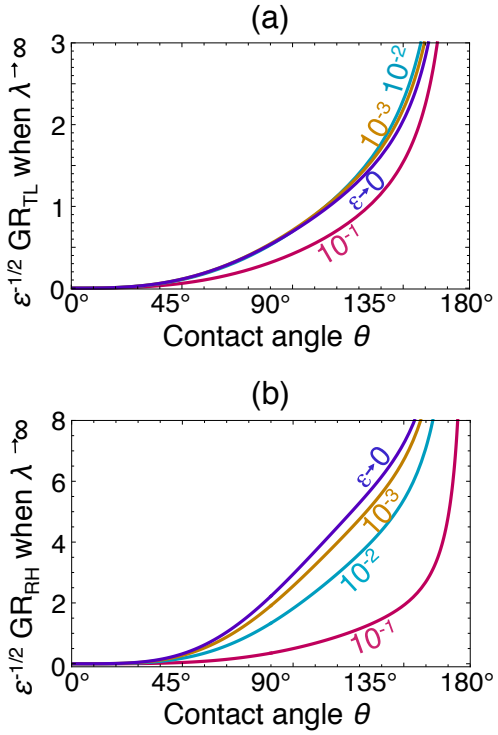

Figure 5-6: The perturbation growth rate as $\lambda \to \infty$ for (a) the triple line, and (b) the rim height. The growth rates are multiplied by $1/\sqrt{\epsilon}$ so that they appear at the same scale for different ϵ. Each curve is labeled with the corresponding value of ϵ. At this scale, curves for $\epsilon < 10^{-5}$ are indistinguishable from the $\epsilon \to 0$ curve.

(discussed in the following section) when ϵ is large, and approaches zero for all contact angles in the limit $\epsilon \to 0$.

The dependence of the perturbation growth rate on the initial film height, $1+\eta$, is shown in Figure 5-8. When $\eta > \epsilon$, the growth rate goes to zero. When $\eta < \epsilon$, the growth rate is essentially that when the rim height equals the film thickness. In other words, perturbations only grow at the onset of retraction, and do not grow once the rim has thickened.

5.4.2 The contributions of the three instabilities

The perturbation growth rates for the three underlying instabilities—Rayleigh-like, divergent retraction, and changing arc length—are plotted with the overall triple line and rim height perturbation growth rates in Figures 5-9 and 5-10. The conditions under which each instability dominates the fingering instability are discussed in this section.

The properties and influence of the Rayleigh-like instability

The orange, dashed curves in Figures 5-9 and 5-10 show the wavelength dependence of the Rayleigh-like instability. The shape of the growth rate curve is the same as for an isolated cylinder. At short wavelengths, the perturbation increases the total surface area, so these perturbations decay. The fastest-growing perturbation is $\sqrt{2}$ times the critical wavelength, and the growth rate goes to zero for long wavelength perturbations.

When the contact angle is 90°, the Rayleigh-like instability behaves identically to the classical (cylindrical) case: $\lambda_{\text{critical}} = 2\pi r$ and $\lambda_{\text{fastest}} = 2\sqrt{2}\pi r$, where r is the radius of curvature of the rim. This is because the symmetry of the 90° contact angle case is identical to a cylinder.

The Rayleigh-like instability plays a central role in determining $\lambda_{\text{critical}}$ for the fingering instability. In Figure 5-7, the orange, dashed curves are the critical wavelengths for the Rayleigh-like instability. For large perturbations, the critical wavelength behavior of the fingering instability resembles the Rayleigh-like instability.

The Rayleigh-like instability is also responsible for the existence of a λ_{fastest} for the fingering instability. No other underlying instability exhibits a finite extremum in its growth

The critical and fastest-growing wavelengths

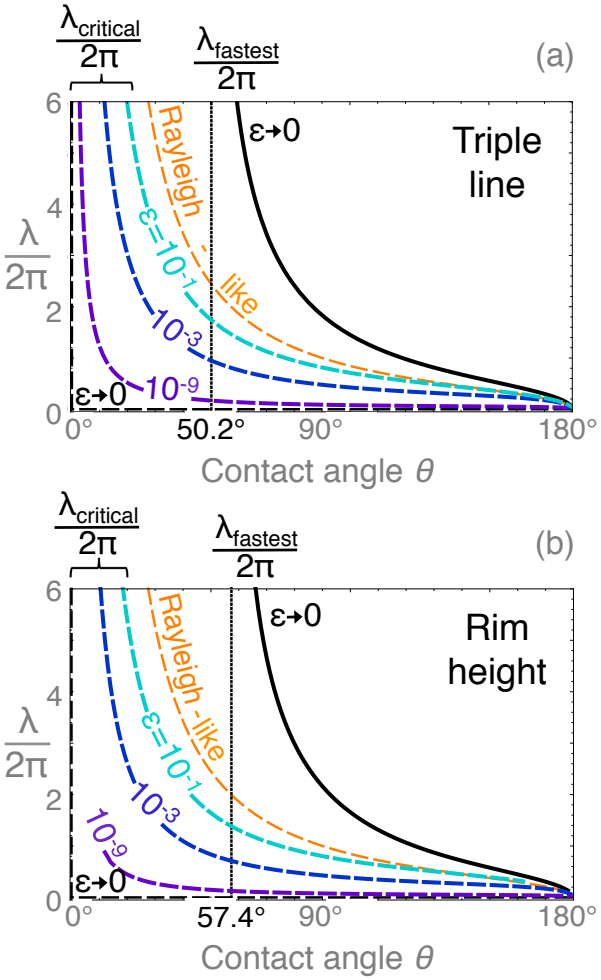

Figure 5-7: The critical and fastest-growing wavelengths for (a) the triple line, and (b) the rim height. The fastest-growing wavelength is the solid black curve. The fastest-wavelength is finite only for contact angles which are sufficiently large, and diverges as it approaches the value indicated with the vertical, dashed black line. The critical wavelength varies strongly with the perturbation amplitude ϵ. The dashed curves are the critical wavelengths, labelled with the corresponding value of ϵ. The critical wavelength for the pure Rayleigh-like instability in the limit $\epsilon \to 0$ is shown in orange as a basis for comparison.

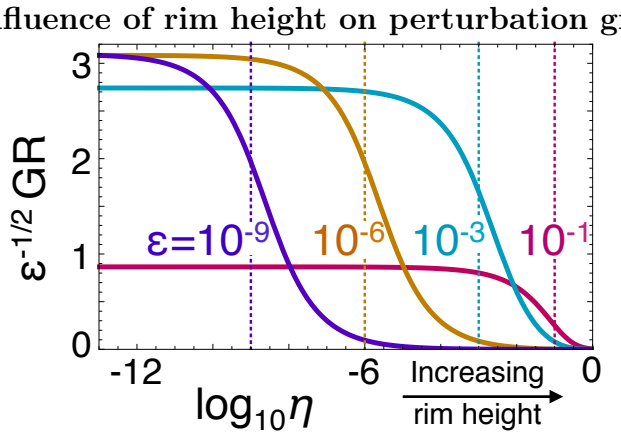

Figure 5-8: The dependence of the perturbation growth rate on the initial rim height $1+\eta$. When $\eta = 0$, the average rim height is $1+\epsilon$. When $\log_{10}\eta = 0$, the rim height is $2+\epsilon$. The growth rate is multiplied by $1/\sqrt{\epsilon}$ so that the vertical scale is independent of ϵ. Each curve is labeled with the corresponding value of ϵ, and the vertical dashed line which passes through the label is where $\eta = \epsilon$. The figure is plotted for the rim-height perturbation growth-rate with $\theta = 90°$, but the curves are qualitatively independent of θ and whether they are for the rim height or triple line perturbation.

rate curve. However, λ_{fastest} disappears with decreasing ϵ, and with decreasing contact angle. This is because with decreasing perturbation amplitude, the contribution of the Rayleigh-like instability decreases faster than divergent-retraction, as shown in Figures 5-10 and 5-9. Physically, this means that a perturbation to the rim affects flows normal to the triple line much more than flows parallel to the triple line. For a small enough perturbation, the Rayleigh-like component of the flow is overwhelmed by other flows, and the fastest-wavelength peak disappears.

The properties and influence of the divergent retraction instability

The green, dashed curves in Figures 5-9 and 5-10 show the wavelength dependence of the divergent retraction instability. This instability grows fastest at long wavelengths. This can be understood by considering the limit of infinite perturbation wavelength: in this case, the instability growth rate reduces to comparing the retraction rates of two uncoupled, infinitely-long, straight rims. The thicker rim has height $1+\eta+2\epsilon$, and retracts more slowly than the thinner rim with height $1+\eta$, due to a difference in driving force. No long-range mass transport is necessary to accommodate a difference in retraction rate.

At first glance, it may appear that the divergent retraction instability should be independent of wavelength. If the triple line position was not perturbed, but the rim height was perturbed, the divergent retraction instability would be independent of wavelength. However, the prescribed perturbation (illustrated in Figure 5-3) advances the triple line wherever the rim is thin. The resulting curvature along the triple line affects the driving force for retraction and introduces the wavelength dependence.

Divergent retraction dominates the critical wavelength behavior for small perturbations. In the limit of small ϵ, the critical wavelength for the divergent retraction instability goes to zero. This same behavior occurs for the fingering instability, as shown in Figure 5-7.

The fastest-growing perturbation for divergent retraction is in the limit of long wavelengths. For small contact angles, the fingering instability exhibits this behavior as well. At larger contact angles ($\theta > 57.4°$), there is a fastest-growing wavelength at finite values. This occurs due to the Rayleigh-like instability; however, λ_{fastest} is at significantly higher wavelengths than the Rayleigh-like case. Divergent retraction is primarily responsible for this shift to longer wavelengths.

The properties and influence of the changing arc length instability

The blue, dashed curves in Figures 5-9 and 5-10 show the wavelength dependence of the changing arc length instability. This instability is only significant at very short wavelengths. When the wavelength of the perturbation is less than $\mathcal{O}(\epsilon)$, the thin portion of the rim gets even thinner during retraction, rather than thickening. This is because the triple line is lengthening so rapidly that the volume swept up by the rim during retraction is less than the the amount required to lengthen the rim and maintain its height.

The arc length instability only makes a small numerical contribution to the net instability. However, the arc-length instability is expected to become more important when the interface energies are anisotropic (see Chapter 6).

The perturbation growth rates for the three underlying instabilities and the fingering instability for different θ

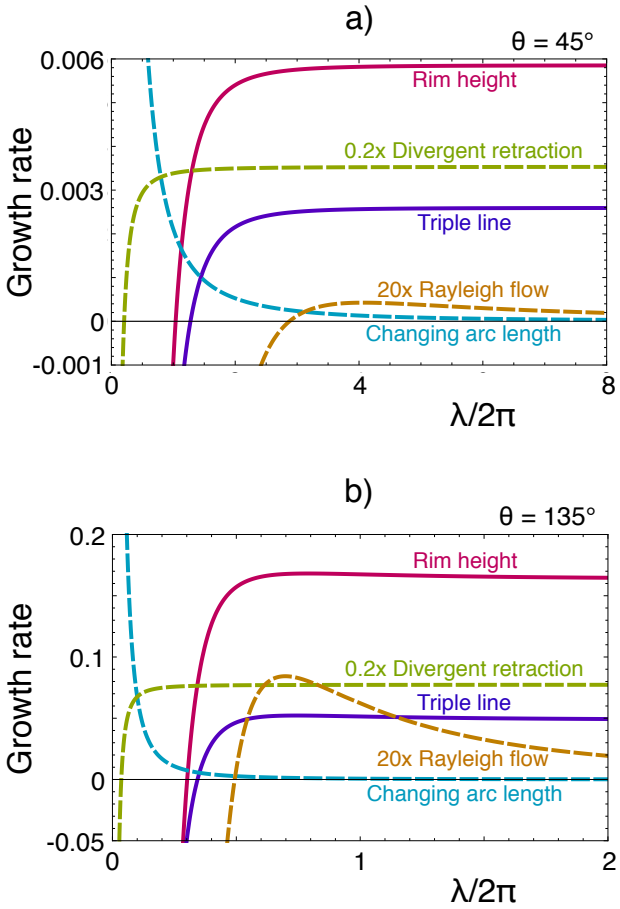

Figure 5-9: The perturbation growth rates on the triple line (Equation 5.8) and rim height (Equation 5.12), as well as for Rayleigh-like (Equation 5.13), divergent retraction (Equation 5.14), and changing arc length (Equation 5.15) instabilities are shown. The horizontal axis is the perturbation wavelength, normalized to the film thickness and divided by 2π. The vertical axis is the perturbation growth rate. (a) is for a contact angle of 45°, and (b) is for 135°. The Rayleigh flow and divergent retraction curves are scaled so that they appear at a similar magnitude to the other curves. Both figures are for $\epsilon = 10^{-3}$.

The perturbation growth rates for the three underlying instabilities and the fingering instability for different ϵ

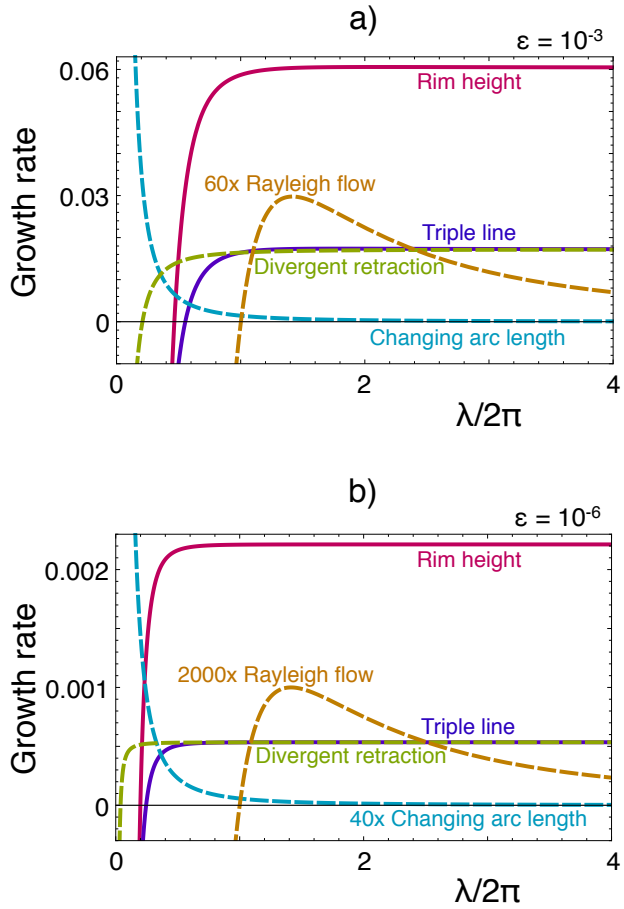

Figure 5-10: The perturbation growth rates on the triple line (Equation 5.8) and rim height (Equation 5.12), as well as for Rayleigh-like (Equation 5.13), divergent retraction (Equation 5.14), and changing arc length (Equation 5.15) instabilities are shown. The horizontal axis is the perturbation wavelength, normalized to the film thickness and divided by 2π. The vertical axis is the perturbation growth rate. (a) is for $\epsilon = 10^{-3}$, and (b) is for $\epsilon = 10^{-6}$. The Rayleigh-like and changing arc length instability curves are scaled differently in each figure. Both figures are for a contact angle of 90°.

5.4.3 Discussion

The growth rate of the instability increases with contact angle (Figure 5-6). Therefore, the instability is more likely to be observed for films with high contact angles.

The perturbation growth rate is essentially constant for $\lambda > \lambda_{\text{fastest}}$ (Figure 5-5). However, this does not imply that extremely large finger spacings are expected. Rather, it suggests that the distance between peaks should be $\lambda_{\text{fastest}} < \lambda < 2\lambda_{\text{fastest}}$. This is because if $\lambda > 2\lambda_{\text{fastest}}$, then another wavelength with a large, positive growth-rate could fit between the existing peaks and reduce the apparent wavelength.

Increasing rim height leads to an overall reduction in the perturbation growth rates (Figure 5-8). This implies that once fingers begin to grow, no new fingers should develop. However, the fingers may merge with time, resulting in a larger finger spacing.

Figure 5-7 shows that $\lambda_{\text{critical}}$ increases with the perturbation size. A larger perturbation being less likely to grow may seem counter-intuitive, but it arises from the Rayleigh-like behavior dominating over divergent retraction as ϵ increases. This is an important consideration when patterning an initial perturbation to achieve a particular finger spacing. For example, if the film thickness is f with contact angle 90°, and the triple line position is deliberately perturbed by a distance $\pm 0.1f$, then the minimum wavelength that can grow is $6.2f$. If it is perturbed by $\pm 0.01f$, then the minimum wavelength is $4.5f$.

5.4.4 Comparison with other models and experiments

In contrast with our results, Kan & Wong concluded that in the limit of long wavelengths, the perturbation growth rate goes to zero [40]. However, their analysis does not include the influence of retraction on the instability, so it cannot account for divergent retraction, nor changing arc length. Additionally, their results are only valid in the limit of long times (*i.e.*, when retraction is negligibly slow), while ours are only valid at short times (*i.e.*, for small rims and negligible valleys). The difference in modeled time regimes may explain the different conclusions.

Our results can be tested experimentally. If the fingering instability arose from the Rayleigh-like and/or arc length instabilities, then perturbations longer than $\approx 2\sqrt{2}\pi r$, where

r is the radius of curvature of the rim, would not grow fast enough to be observed. However, if the divergent retraction mechanism indeed dominates the character of the fingering instability, then finger spacings much greater than the $2\sqrt{2}\pi r$ should be seen.

While there are many publications which show fingers, there are none to the author's knowledge that show the film edge at early times with the initial perturbation. Fingers are known to evolve to a steady-state geometry (studied elsewhere **??**), which may have a different characteristic wavelength than the initial, fundamental instability. The different mechanisms inherent to the initial fingering instability and subsequent steady-state finger geometry mean that comparing the predictions of this work with steady-state finger spacings is meaningless.

5.5 Conclusion

We identify three underlying mechanisms of the fingering instability:

1. Rayleigh-like instability: This instability arises when variations in rim height would lead to a reduction in the total surface area of the rim. Gradients in mean curvature parallel to the triple line drive mass transport.

2. Divergent retraction instability: The driving force for retraction is greater for thinner rims, so they will retract faster than thicker rims. Mass flows normal to the triple line.

3. Changing arc length: The rate of change of rim arc length during retraction is a function of the in-plane curvature of the triple line. Positively-curved sections of rim thicken faster than a straight rim because the mass contained in the rim must fit into an ever-shorter length, and vice-versa.

These mechanisms all play a part in the shape evolution of dewetting thin film edges. The mechanisms are coupled, but an analysis which artificially separates them reveals that the divergent retraction instability is the underlying cause of the fingering instability (Figures 5-9, 5-10). The Rayleigh-like and changing arc length instabilities affect the critical and fastest-growing wavelength values, but only when the perturbation is large.

Poorly-wetting (large contact angle) films are much more susceptible to the fingering instability than highly-wetting (small contact angle) films (Figure 5-5). As the contact angle increases, the critical wavelength decreases, so shorter wavelength perturbations can grow (Figure 5-7). Simultaneously, the perturbation growth rate increases with contact angle, so perturbations will grow into fingers much more quickly (Figure 5-6).

Dewetting is often used to create arrays of particles [50, 19, 65, 64, 70]. There has recently been interest in tempting the substrate to achieve particular particle spacings [20, 87, 30]. However, an easier approach would be to control finger spacings to achieve the desired spacing. This work suggests that intentionally perturbing the film edge prior to annealing is sufficient to control the finger spacing. A large range of wavelengths will grow (Figure 5-7), and the growth rate increases with the perturbation size, so the prescribed wavelength should dominate over random fluctuations. Furthermore, only the perturbations which are initially present should grow because growth rates go to zero for small perturbations once the rim is thicker than the perturbation amplitude (Figure 5-8).

Chapter 6

The Corner Instability: An Analytical Model and Underlying Mechanisms

6.1 Introducion

The corner instability is introduced in Section 1.4.3. It occurs on anisotropic films, where two straight edges meet. Initially, the corner retracts at the same rate as the edges. However, at some point, the retraction rate at the corners becomes constant, while the retraction rate of the edges continues to decrease over time [18]. The difference in retraction rates arises from a constant rim height at the corner, while the rims along the edges thicken with time in a similar fashion to a retracting infinite, straight edge [18].

No quantitative approach has been present to explain this phenomenology. Previous work has suggested that the corner instability is associated with mass flow away from the tip of the retracting corner. Ye and Thompson [88, 78] proposed that the corner instability arises due to mass flow away from the corner tip, onto the flat film. It is supposed that near the corner, there is a two-dimensional diffusion field, while along the edge, there is a one-dimensional diffusion field (such flows are depicted in Figure 2 of reference [88]). The two-dimensional field implies transport to a larger area, and therefore enables faster retraction near corners. However, there is no evidence supporting this proposed mass flow. The film is not observed to thicken ahead of the retracting rim in experiments [63]. Also, isotropic models of dewetting show no net mass flow onto the flat film at all [75, 85], and anisotropic models show a small

mass flow in the opposite direction, leading to thinning of the bulk film [96]. Rabkin *et al.* [63] suggested that mass rejected from corners flows along the thickening rim towards the centers of the straight edges, leading to a constant rim size at the corner while the centers of the edges accumulate mass. However, no evidence of this mass flow has been presented.

In this chapter, an alternative mechanism for the corner instability is presented, which is based on the results of a model and comparison with experiments. The geometric assumptions in the model are consistent with the observed structure near a corner. The model and experiments are in quantitative agreement, showing that the mechanism found in the model is a plausible explanation for the corner instability.

6.2 Summary of experimental results

Experiments to study the onset of the corner instability were performed by Gye-Hyun Kim [95]. He investigated 130 nm-thick, single-crystal (001) Ni films on a (001) MgO substrate at 890°C. Initially-square holes either formed naturally during annealing, or were patterned by photolithography.

Figure 6-1 is reproduced from reference [95], and shows the development of a corner instability for a natural hole. The hole is bounded by [110] facets. Initially, the hole grows and remains square, but after some time, the corners retract faster than the hole edges. To accommodate the shape change to the hole after the instability develops, [010]-type facets appear as well. The hole has a roughly uniform rim height along most of the edge, which is connected by a sloped, straight section to the tip. Henceforth, the "tip" will be used to refer to the <1 μm-sized region where the rim height is uniform and the triple line has a large, negative curvature. The "transition" region refers to the sloped, straight section of rim on either side of the tip. The term "edge" refers to the central section of the rim which is roughly straight and has a uniform height; however, the triple line along the edge often develops a positive curvature after the corner instability forms. The tip, transition, and edge are schematically drawn in Figure 6-2. A similar rim structure around polygonal holes has been observed previously [76, 18, 63].

To analyze the mass accumulation trend at the tip and the center of the edge, the cross-

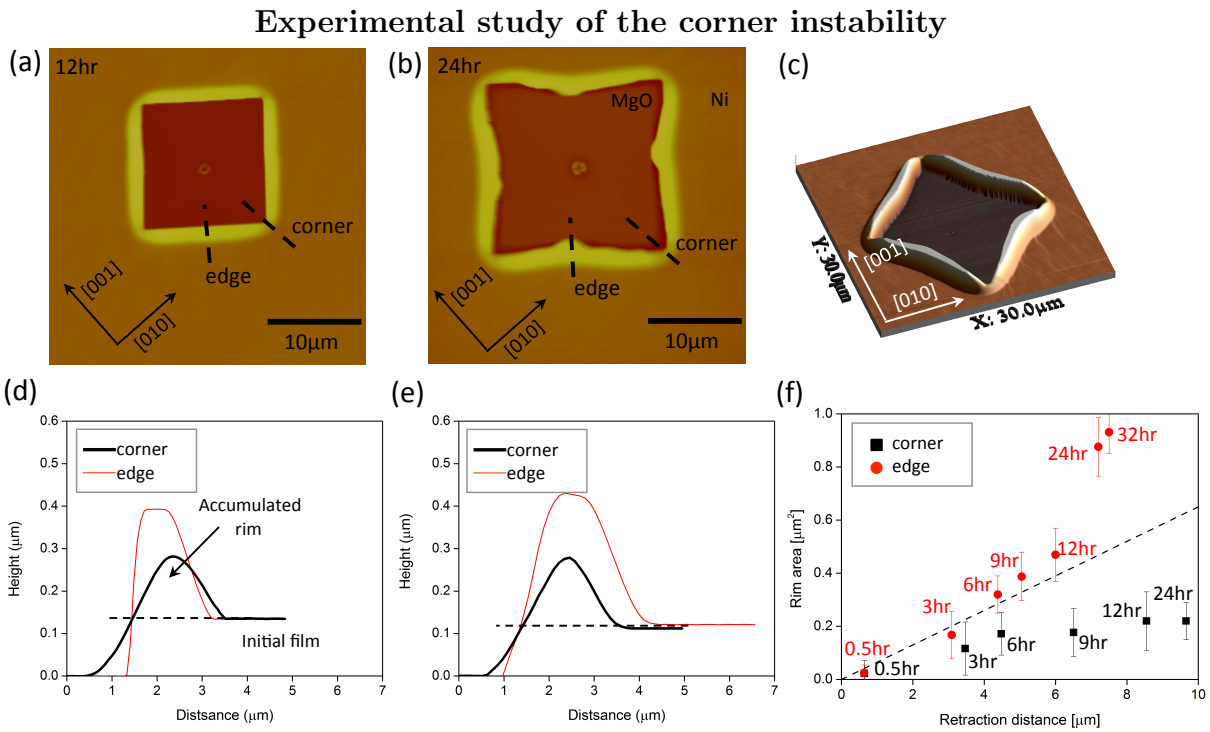

Figure 6-1: This figure is reproduced from reference [95]. (a) A top-down AFM image of a natural hole after 12 hours of annealing, showing that a corner instability has not yet developed. (b) A top-down AFM image of a natural hole after 24 hours of annealing, showing the early stages of a corner instability, with the corners retracting faster than the edges. (c) A three-dimensional view of a natural hole after the corners became unstable, showing that central regions of the rims at edges have uniform heights, while regions adjacent to the tip have a constant slope. (d) A cross-sectional AFM profile of the edge and the tip at the corner of a natural hole after a 12-hour anneal, showing that the rim is much taller on the edge. (e) A cross-sectional AFM profile of the edge and the tip at the corner of a natural hole after a 24-hour anneal, showing that the tip rim has not changed from (d), but that the rim at the edge is even taller and thicker. (f) The cross-sectional rim area at the edge and the tip of a natural hole at different retraction distances (distance is measured from the center of the hole). The dashed line is a linear fit for the first three data points for the edge, and is intended as a visual guide. The annealing time for each data point is indicated in the figure. Samples were annealed at 890°C.

sectional area of the accumulated rim was quantified at the tip and the center of the edge using the AFM scans [95]. This is illustrated in Figures 6-1(d)-(e). Cross-sectional SEM images (not shown) indicate that the contact angle is approximately 90ą. However, non-90ą contact angles are observed in the profiles due to the 75ą AFM tip angle. This is more significant at the tips, where the tip is confined on two sides.

Figure 6-1(f) shows the cross-sectional rim areas at the edge and the tip of natural holes at different retraction distances. Increasing retraction distance corresponds to increasing annealing time. The dashed line serves a basis for comparison. If all of the material swept up due to retraction were incorporated into the rim, and no mass transfer occurred parallel to the rim, the rim cross-sectional area should grow linearly with retraction distance with a slope equal to the film thickness. The edge data follow a linear trend, to within experimental error, with the exception of the last two data points. However, the tip data follow a sublinear trend, and at late times, the cross-sectional area approaches a constant value. This indicates that at that point the rim at the tip does not change its shape with time. The late stage data were collected well after the corners became unstable and the edges of the hole underwent significant bending. The ÒnotchÓ visible at the midpoint of each edge in Figure 6-1(b) occurs through a combination of faceting along the triple line and interactions between the rim regions on either side of the midpoint. Therefore, the last two data points for the edge of the hole show effects that are not directly related to the onset of the corner instability.

Square holes of various sizes were patterned and also annealed [95]. The length of the transition region is independent of the size of the patterned holes, and found to be $5.6\,\mu m \pm 0.61\,\mu m$. Only the holes with edge lengths less than two times the transition region length show a size effect. Therefore, retraction distances are at most weakly dependent of the initial hole size. These size-independent characteristics imply that the corner instability is a local phenomenon.

6.3 Corner instability model

To determine the underlying mechanism for the corner instability, we present a simple model. A core assumption of this model is based on fundamental results from prior modeling efforts:

the material contained in the rim is taken to be equal to the amount swept up during edge retraction. For isotropic materials (materials with both isotropic surface energies and diffusivities) rims develop an oscillatory cross-sectional profile, in which a set of valleys with rapidly decreasing depth forms ahead of the advancing rims **??**. This implies that some mass from the first valley flows toward the rim, but this is a small fraction of the total mass incorporated due to retraction, and can be neglected. Similarly, for anisotropic films lacking a valley, an additional mass flow from the bulk film toward the rim is present. However, it is negligibly small over the relevant time scales, comprising at most a few percent of the total rim mass [96].

Another assumption of the model is that the rim is semi-circular in cross-section. The actual rim profile is not described by a closed-form function, and varies with time, as shown in Figure 6-1(d) and (e). This complexity is difficult to capture in an analytical model, so a semi-circle is assumed to make calculations of volume within the rim straightforward.

The two-dimensional model presented in Chapter 4, and the fingering instability analysis in Chapter 5, use very similar assumptions. However, the rim geometry used to model the corner instability includes additional complexity to describe the corner evolution.

6.3.1 Model geometry

The geometry assumed for the model is informed by experimental results. The three regions near the corner identified in Figure 6-1, the "tip," "transition," and "edge," are shown schematically in Figure 6-2. In the model, all lengths are normalized to the film thickness H, and the contact angle is 90°, to be consistent with the observed contact angle. This contact angle indicates that the surface energy of the substrate in contact with the vapor phase is equal to the interfacial energy of the substrate-film interface.

The tip of the corner is not perfectly sharp, but instead has uniform curvature along the triple line. The radius of curvature, b_{tip}, is on the order of a few times the film thickness. b_{tip} is fixed by a combination of the surface energy anisotropy and corner energy of the Ni film, and its value is observed to be independent of time. The rim also has a uniform height in this region, r_{tip}. Therefore, the tip area will be modeled as a portion of a torus, as drawn in Figure 6-2. The inner radius of the torus is b_{tip} and the cross-sectional radius is r_{tip}.

A schematic of the corner geometry

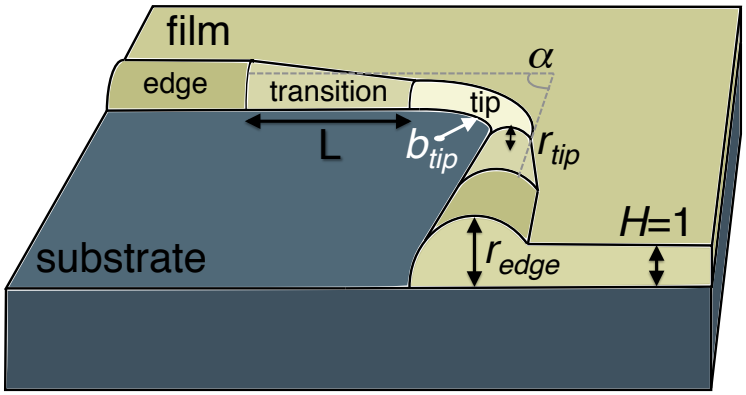

Figure 6-2: The assumed geometry of the corner of a hole is shown. All distances are normalized to the film thickness H. The rim has height r_{tip} at the tip of the corner and height r_{edge} along the majority of the edge of the hole. The rim height gradually increases from r_{tip} to r_{edge} over a distance L. The anisotropy of the film material holds the apparent angle of the corner, α, and the radius of curvature of the triple line at the tip, b_{tip}, at constant values.

The rim on the edge of the hole has a uniform height. However, the observed rim width varies. For the purposes of the model, the variation in rim profile is neglected, and the rim height is taken as r_{edge}. This assumption is made because the variation in rim width is only significant after the corner instability has developed. The model is intended to capture the behavior which causes the instability, rather than subsequent behavior (including notch formation). Therefore, it is also assumed that the edge is straight. It also turns out that accounting for curvature of the edge does not significantly affect the model results, so it is acceptable to neglect it.

Detailed AFM scans of the transition region of the rim revealed a linearly-increasing rim height from r_{tip} to r_{edge}. The triple line in this region is straight. Both of these observations are incorporated into the model. The length of the sloped region is taken to be L, as shown in Figure 6-2. The angle between the transition regions on either side of the tip is α. For the (001)Ni-on-MgO system, $\alpha = 90°$, and is set by the facets bounding the hole.

6.3.2 Retraction velocity

The retraction velocity, v_{retr}, is simply the dimensionless capillary-driven surface diffusion normal velocity, v_n (Equation 1.8), at the triple line:

$$v_{\text{retr}} = \Big(\frac{\partial^2 \kappa}{\partial s_1^2} + \frac{\partial^2 \kappa}{\partial s_2^2}\Big). \tag{6.1}$$

The curvature of the triple line at the corner tip is $\kappa_{\text{tip}} = 1/r_{\text{tip}} - 1/b_{\text{tip}}$, with r_{tip} and b_{tip} defined in Figure 6-2. The curvature of the triple line at the edge is $\kappa_{\text{edge}} = 1/r_{\text{edge}}$ (assuming that the edge is straight, or that the radius of curvature for the triple line is much greater than r_{edge}, which is the case in all experimental results discussed above).

To find the retraction velocity, a finite-difference approximation is used to estimate the second derivatives of curvature. The forward finite-difference formula for a second derivative at the point $f(x)|_{x=0}$, accurate to second order, is

$$\frac{\partial^2 f}{\partial x^2} \approx \frac{f(2\Delta x) - 2f(\Delta x) + f(0)}{\Delta x^2}. \tag{6.2}$$

The value of s_1 at the tip of the corner is defined as zero, and the value of s_2 is defined as zero at the triple line, as shown in Figure 6-3. Using Equation 4.12, $\partial^2\kappa/\partial s_1^2$ can be estimated as

$$\frac{\partial^2 \kappa}{\partial s_1^2} \approx \frac{\kappa(2\Delta s_1, 0) - 2\kappa(\Delta s_1, 0) + \kappa(0,0)}{\Delta s_1^2} = \frac{(1/r_*) - 2(1/r_{\text{tip}}) + (1/r_{\text{tip}} - 1/b_{\text{tip}})}{(b_{\text{tip}}\alpha/2)^2}, \tag{6.3}$$

where α is the angle of the tip, Δs_1 is the arc length from the midpoint of the tip to the beginning of the transition region, and r_* is the rim radius of curvature a distance $2\Delta s_1 = (b_{\text{tip}}\alpha)$ away from the tip, as indicated in Figure 6-3. Taking into account the linear increase in rim height across the transition region, r_* is given by

$$r_* = r_{\text{tip}} + \frac{r_{\text{edge}} - r_{\text{tip}}}{L} b_{\text{tip}} \frac{\alpha}{2}. \tag{6.4}$$

Equation 6.3 accounts for mass flow towards or away from the tip, parallel to the rim.

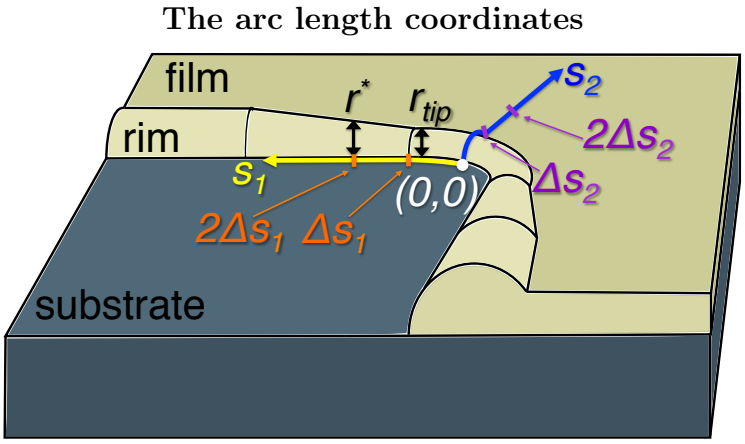

Figure 6-3: The arc length coordinates s_1 and s_2 are shown on the corner geometry schematic. The origin is at the midpoint of the corner tip, and the points used to calculate $\frac{\partial^2\kappa}{\partial s_1^2}$ and $\frac{\partial^2\kappa}{\partial s_2^2}$, Δs_1 and Δs_2, are marked.

$\partial^2\kappa/\partial s_2^2$ at the tip midpoint can be estimated as

$$\frac{\partial^2\kappa}{\partial s_2^2} \approx \frac{\kappa(0,2\Delta s_2) - 2\kappa(0,\Delta s_2) + \kappa(0,0)}{\Delta s_2^2} = \frac{(1/r_{\text{tip}}) - (1/b_{\text{tip}})}{\left(\pi r_{\text{tip}} - r_{\text{tip}} \sin^{-1}(1/r_{\text{tip}})\right)^2}, \tag{6.5}$$

where Δs_2 is the arc length from the triple line to the flat film at the center of the tip, $\kappa(0,\Delta s_2)$ is measured on the flat film just beyond where it meets the rim, and $\kappa(0,2\Delta s_2)$ is measured further out on the flat film. $\kappa(0,\Delta s_2) = \kappa(0,2\Delta s_2) = 0$, as shown in Figure 6-3. Equation 6.5 accounts for the driving force for the corner to retract.

Equations 6.1, 6.3, and 6.5 together provide the retraction velocity, $v_{\text{retr,tip}}$. With $\alpha = 90°$, for a given rim height and tip sharpness, b_{tip},

$$v_{\text{retr, tip}} = \frac{4}{L^2}\left(\frac{1}{r_{\text{tip}}} + \frac{1}{r_{\text{edge}}} - \frac{4}{r_{\text{tip}} + r_{\text{edge}}} - \frac{1}{b_{\text{tip}}}\right) + \frac{b_{\text{tip}} - r_{\text{tip}}}{r_{\text{tip}}^3 b_{\text{tip}}\left(\pi - \sin^{-1}\frac{1}{r_{\text{tip}}}\right)^2}. \tag{6.6}$$

In Equation 6.6, the first term is negligible (less than 2% of the second term) when $L > \approx 25$. Experiments give $L = 47$ (in dimensionless units), so it can be expected that L has little to no effect on the retraction velocity.

The same method as above can be applied to arrive at the equation describing the retraction velocity on the edge of the hole. It is assumed that the edge is roughly straight

near the midpoint, so $\partial^2\kappa/\partial s_1^2 = 0$. Therefore,

$$v_{\text{retr, edge}} = \frac{1}{r_{\text{edge}}^3\left(\pi - \sin^{-1}\frac{1}{r_{\text{edge}}}\right)^2}. \tag{6.7}$$

6.3.3 Rim height as a function of time

The change in the rim height as a function of time can be calculated by enforcing volume conservation within the rim. As the rim retracts at the corner tip, the arc length must increase, and a portion of the flat film will be incorporated into the rim. Figure 6-4 shows a schematic of the tip at time t and at time $t + dt$. The volume contained in the rim at time $t + dt$ must equal the volume contained in the rim at time t, plus the volume of flat film swept up due to retraction.

Given $r_{\text{tip},1}$ and b_{tip}, the volume in the rim at the tip can be found; this is equivalent to finding the volume of a portion of a torus. With these parameters, the retraction velocity is also known. Thus, the distance the film retracts in time dt is equal to $v_{\text{retr,tip}}dt$.

The portion of flat film swept up during retraction has width w, as shown in Figure 6-4. w can be found in terms of $r_{\text{tip},2}$. Setting the total change in volume to zero provides an equation for $r_{\text{tip},2}$. However, it is transcendental. To arrive at an analytical answer, it is assumed that $r_{\text{tip},2} = r_{\text{tip},1} + \epsilon v_{\text{retr,tip}}dt$, where ϵ is an unknown, dimensionless parameter. The equation for $r_{\text{tip},2}$ is expanded as a Taylor series in dt to first-order. The first-order expansion can be solved for ϵ:

$$\begin{aligned}\epsilon_{\text{tip}} = \Big(&-2 + 4r_{\text{tip}}\sqrt{r_{\text{tip}}^2 - 1} + r_{\text{tip}}^2(2 - \pi\sqrt{r_{\text{tip}}^2 - 1}) + 4b_{\text{tip}}\sqrt{r_{\text{tip}}^2 - 1} \\ &- 2r_{\text{tip}}^2\sqrt{r_{\text{tip}}^2 - 1}\tan^{-1}\sqrt{r_{\text{tip}}^2 - 1}\Big) \Big/ \Big(2 + r_{\text{tip}}^2(-2 + 3\pi\sqrt{r_{\text{tip}}^2 - 1}) - 4b_{\text{tip}}\sqrt{r_{\text{tip}}^2 - 1} \\ &+ 2r_{\text{tip}}\sqrt{r_{\text{tip}}^2 - 1}(\pi b_{\text{tip}} - 4) + 2r_{\text{tip}}\sqrt{r_{\text{tip}}^2 - 1}(3r_{\text{tip}} + 2b_{\text{tip}})\tan^{-1}\sqrt{r_{\text{tip}}^2 - 1}\Big).\end{aligned} \tag{6.8}$$

A differential equation for $r_{\text{tip}}(t)$ is provided by computing $(r_{\text{tip},2} - r_{\text{tip},1})/dt$, which equals $\epsilon v_{\text{retr, tip}}$.

The discretized time evolution of the corner tip

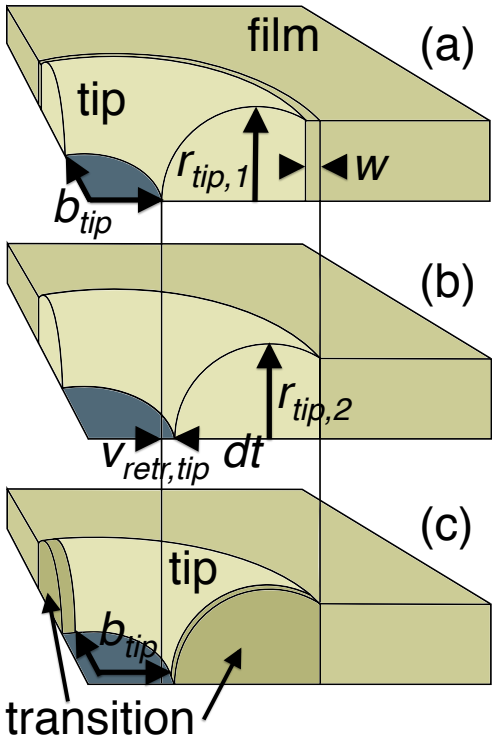

Figure 6-4: A detailed schematic of the tip geometry is shown. Part (a) shows the film at time t. Part (b) shows the film at time $t + dt$. The initial rim height, $r_{\mathrm{tip},1}$, is known, and b_{tip} is constant. The new rim height, $r_{\mathrm{tip},2}$, is found by volume conservation: the volume in the rim at time t plus the volume of film swept up in the time dt must equal the volume in the rim at time $t + dt$. The volume swept up during retraction is that contained in the region of radial thickness w, shown in (a). Part (c) also shows the film at time $t + dt$. The dark-shaded portions of the rim are now part of the transition region, and are no longer part of the corner tip. This is because b_{tip} is fixed by the anisotropy of the film material, preventing the arc length of the tip region from increasing with time.

The same method can be applied to find $r_{\text{edge}}(t)$. ϵ_{edge} is given by

$$\epsilon_{\text{edge}} = \frac{1}{-1 + \pi r_{\text{edge}} - r_{\text{edge}} \sin^{-1} \frac{1}{r_{\text{edge}}}}. \tag{6.9}$$

The differential equations for $r_{\text{tip}}(t)$ and $r_{\text{edge}}(t)$ are coupled because $dr_{\text{tip}}/dt = \epsilon_{\text{tip}} v_{\text{retr,tip}}$, and $v_{\text{retr,tip}}$ depends on both $r_{\text{tip}}(t)$ and $r_{\text{edge}}(t)$.

The differential equations for $r_{\text{tip}}(t)$ and $r_{\text{edge}}(t)$ do not have closed-form solutions. However, they can be integrated numerically. Using the built-in numerical differential equation solver and numerical integration function in *Mathematica 9* on a *ca.* 2011 laptop, the total time for the numerical work takes just a few seconds. The initial conditions are at $t = 0$, $r_{\text{tip}} = 1$ and $r_{\text{edge}} = 1$. Plots of $r_{\text{tip}}(t)$ and $r_{\text{edge}}(t)$ are shown in Section 5.4.

6.3.4 The steady-state rim height at the tip

While the rim height on the edge of the hole always increases with time, the rim height at the tip may increase or decrease. This is possible because mass is added to the rim during retraction, but the arc length of the tip must increase due to high curvature of the triple line at the tip. This effect is analogous to a Poisson's ratio of 0.5: lengthening the rim parallel to the triple line requires the height to decrease. This can be seen in Figure 6-4.

When the volume of flat film swept up due to retraction is exactly balanced by the volume "lost" due to lengthening of the rim, the rim height stays constant. This balance occurs when ϵ_{tip} is equal to zero. $\epsilon_{\text{tip}} = 0$ when b_{tip} equals the critical value b_{critical}:

$$b_{\text{critical}} = \frac{1}{4}\Big(-4r_{\text{tip}} + \frac{2}{\sqrt{r_{\text{tip}}^2 - 1}} + r_{\text{tip}}^2(\pi - \frac{2}{\sqrt{r_{\text{tip}}^2 - 1}}) + 2r_{\text{tip}}^2 \tan^{-1}\sqrt{r_{\text{tip}}^2 - 1}\Big) \tag{6.10}$$

A contour plot of ϵ_{tip} is shown in Figure 6-5. The black line is the trace of Equation 6.10, and provides the steady-state value of r_{tip}, r_{tip}^*, for a given value of b_{tip}. The rim height r_{tip}^* is at a stable equilibrium because a rim height greater than r_{tip}^* will decrease with time, and vice-versa.

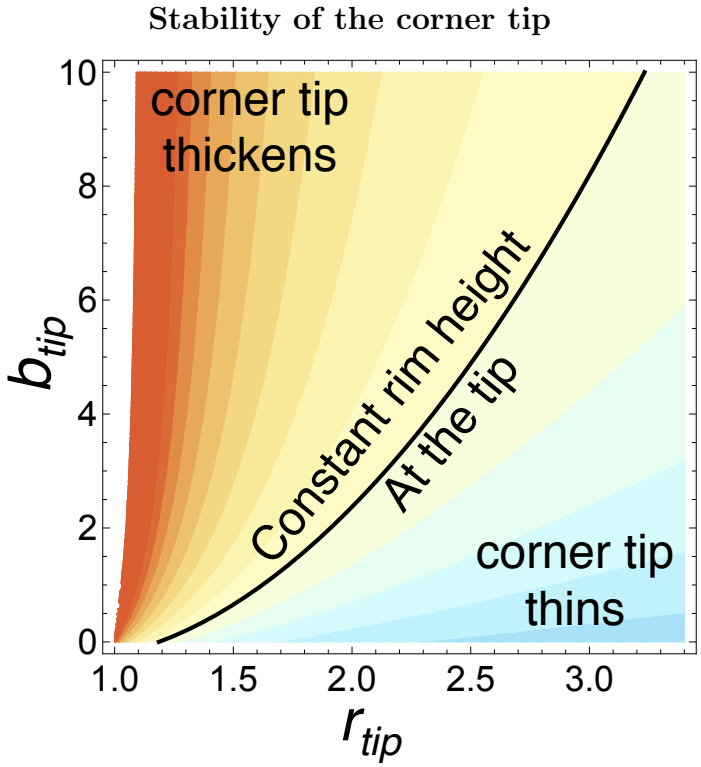

Figure 6-5: A contour plot of the rate of rim height change at the tip is shown. Warm colors indicate that the rim is thickening with time for a given r_{tip} and b_{tip}; cool colors indicate that the tip rim thins with time. The heavy black line is the steady-state rim height at the tip, r^*_{tip}.

6.4 Discussion

6.4.1 The mechanism of the corner instability

The main result from the model is that the corner instability arises from two competing effects: the mass swept up due to retraction tends to increase the rim height, while the increasing arc length of the hole tends to decrease the rim height. These two effects are shown in Figure 6-4. When these effects are in equilibrium, the rim height at the tip remains constant.

Note that no long-range mass transport is necessary for a corner instability to develop. The effect is entirely local, and the only mass transport needed is contained with in the rim at the corner tip. The only condition for the instability to occur is the pre-existence of a sharp corner in the film edge so that arc length increases are localized to the curved portion of the triple line. Therefore, the corner instability can occur in patterned isotropic films as well.

For a circular hole, as modeled by Brandon and Bradshaw [6], the mass swept up always dominates over the increasing arc length effect. Therefore, the rim height increases with time. However, a polygonal hole is fundamentally different. The edges remain straight, and so their arc length does not increase over time. All of the increase in arc length must occur at the tip. Edge retraction is driven in the direction locally-normal to the triple line, so the radius of curvature at the corner tip tends to increase, as shown in Figure 6-4(b). However, anisotropy straightens out the material at the edges of the tip, correcting the increase in radius of curvature. The material at the edges of the tip joins the transition region, as shown in Figure 6-4(c).

6.4.2 Evidence against other mechanisms for the instability

A simple estimation casts doubt on the mechanism proposed by Rabkin et al. [63]. They suggest that the corner instability occurs by a mass flow, within the rim, from the tip region towards the edges. However, the following calculation demonstrates that the driving force for mass flow points in the opposite direction, which should, if anything, inhibit the corner

instability (this flow is accounted for in our model).

The curvature at the tip is estimated to be $\kappa_{\text{tip}} = 1/r_{\text{tip}} - 1/b_{\text{tip}}$, with r_{tip} and b_{tip} defined in Figure 6-2. The curvature at the edge is $\kappa_{\text{edge}} = 1/r_{\text{edge}}$. The chemical potential, μ, for a system whose only contribution to the free energy is surface tension, is $\mu = \Omega\gamma\kappa$, where Ω is the atomic volume and γ is the surface energy. The mass flux is $J = (-D_s\nu)/(kT)\partial\mu/\partial s$, where we take the s coordinate to be parallel to the rim, and all other parameters have the usual meaning. The gradient in chemical potential, parallel to the rim, can be estimated as

$$\frac{\partial\mu}{\partial s} \approx \frac{\Delta\mu}{\Delta s} = \frac{\mu_{\text{tip}} - \mu_{\text{edge}}}{s_{\text{tip}} - s_{\text{edge}}} = \Omega\gamma\frac{\kappa_{\text{tip}} - \kappa_{\text{edge}}}{L} = \frac{\Omega\gamma}{L}\Big(\frac{1}{r_{\text{tip}}} - \frac{r_{\text{edge}} + b_{\text{tip}}}{r_{\text{edge}}b_{\text{tip}}}\Big). \tag{6.11}$$

Therefore, the mass flux becomes

$$J = \frac{D_s\nu\Omega\gamma}{LkT}\Big(\frac{r_{\text{edge}} + b_{\text{tip}}}{r_{\text{edge}}b_{\text{tip}}} - \frac{1}{r_{\text{tip}}}\Big). \tag{6.12}$$

If the flux is positive, then the chemical potential is higher at the edge than at the tip, so mass flows from the edge towards the tip, and vice versa.

Using the experimentally-obtained value of $b_{\text{tip}} = 3.89$ and the model values for r_{tip} and r_{edge} shown in Figure 6-6, the mass flux is expected to initially be positive, indicating that material flows from the edge towards the tip. The flux decreases slowly with time, and will only reverse after the corner instability is already established, when $r_{\text{tip}} = 2.32$ and $r_{\text{edge}} = 5.75$, which corresponds to a dimensionless time of 29,000. Using the experimentally-obtained values of r_{tip} and r_{edge}, the flux does not reverse during the experiment. If the triple line along the edge is bent like in Figure 6-1, it increases the flux towards the tip and further delays the sign change. Therefore, mass flow parallel to the triple line is not responsible for the corner instability.

6.4.3 Comparison of the model and experimental results

The steady-state rim height at the tip predicted by the model matches the experimental results to within experimental error. The experimental value of r^*_{tip} is 2.3 ± 0.2, and b_{tip} is 3.89 ± 0.2 (both quantities are normalized to the film thickness of 130 nm). Using $b_{\text{tip}} = 3.89$

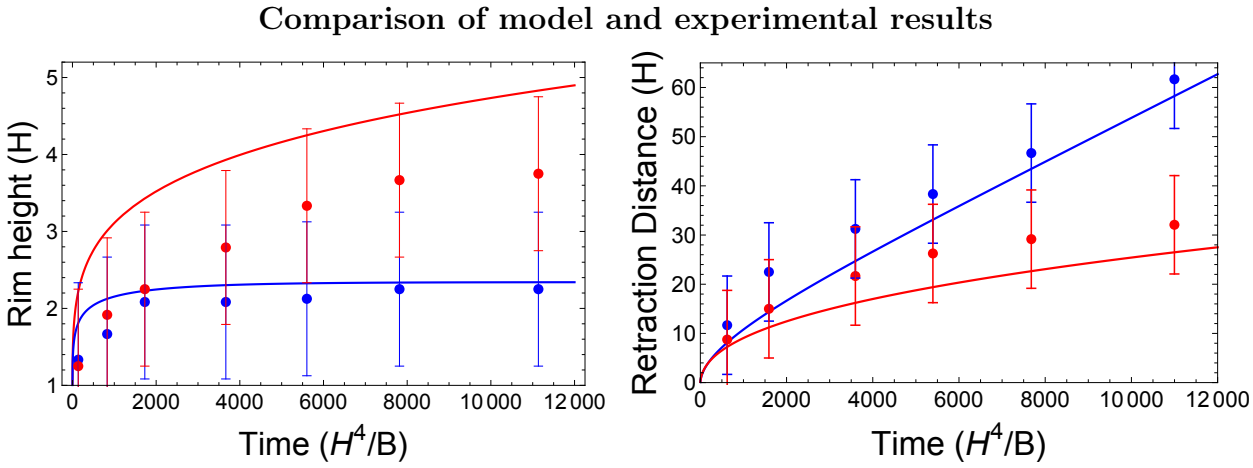

Figure 6-6: Experimental and model results for the rim height and retraction distance as a function of time are shown. The red data and curves are for the edge of the hole, and the blue data and curves are for the tip. The model was run with experimentally-obtained values for b_{tip} and L. The model and experimental results at the tip are in good agreement. The model over-estimates the height of the rim at the edge, and therefore underestimates the retraction distance at the edge.

in Equation 6.10 gives r^*_{tip} as 2.32, which is in excellent agreement with the observed value. Furthermore, Equation 6.6 gives the relationship between r_{tip}, b_{tip}, L, and the retraction velocity of the tip. When L is large (> 25), the dependence on L is negligible, and the corner tip retraction velocity simplifies to

$$v_{\text{retr, tip}} = \frac{b_{\text{tip}} - r_{\text{tip}}}{r_{\text{tip}}^3 b_{\text{tip}} \left(\pi - \sin^{-1} \frac{1}{r_{\text{tip}}}\right)^2}. \tag{6.13}$$

Using the experimental value for b_{tip}, the corner tip velocity should be $4.4 \times 10^{-3} BH^{-3}$, which is 221 nm/hr. Fitting the last 4 data points for the corner retraction distance vs. time (shown in Figure 6-6) with a line gives a corner tip velocity of 204 nm/hr, which is only an 8% mismatch with the model.

The rim height as a function of time from experiments and the model are shown in Figure 6-6. At the tip, the model and experiment agree to within experimental error. At the edge, the model overestimates the rim height, and therefore underestimates the retraction distance. However, the model qualitatively follows the trend of the data.

The discrepancies between the model and experiment at the hole edge may be due to the

assumption of a straight rim along the edge with uniform width. Figure 6-1 shows that the rim height is constant along the edge, but the width and retraction distance vary after the corner instability takes effect. In Figure 6-1(b), a notch is visible at the center of each edge of the hole. The rim is sufficiently wide at the notch that parts of the rim on either side of the midpoint will interact, which is not counted for in the model.

The over-estimate of rim height on the hole edge could be also due to the anisotropy of the real system. The top of the rim on the hole edge is faceted, as shown in Figure 6-1(c)-(e). This facet may decrease the rimÕs mean curvature relative to the assumed semi-circular rim, which would cause it to retract more slowly than the model rim.

6.5 Conclusion

Holes in single-crystal thin films may be faceted. The corners where facets meet rapidly evolve to and maintain a characteristic in-plane radius of curvature. For Ni (100) films [95], the radius of curvature was observed to be constant throughout the dewetting process. The rim at the tip itself is uniformly thin, and connects to the thicker rim along the edges of the hole via a straight, linearly-sloped transition section of rim. These two observations are sufficient to define the geometry for a model that reproduces the corner instability.

In addition to the geometric constraints, the model contains two assumptions: the rim cross-sectional profile is simplified to a circular arc, and mass does not leave the rim, and can only enter it by being swept up due to retraction. These assumptions lead to the conclusion that the corner instability arises due to a balance of mass flows. The addition of mass by retraction tends to increase the rim height, while the need to increase the perimeter of the hole tends to thin the rim as mass is spread over a longer length. The thinning effect only occurs at the tip because this is the only region of the triple line with in-plane curvature.

In the early stages of hole growth, the rim at the tip of the corner grows because it is still thin enough that additional mass can compensate for elongation of the rim adjacent to the tip. However, as the rim at the tip becomes thicker, an increasing fraction of the incoming mass is needed for elongation of the rim adjacent to the tip. Eventually, a steady state is reached, and the rim height stays constant. A constant rim height implies a constant

retraction rate, which is observed experimentally. This is in contrast to what happens on the straight edges of the hole, where there is no arc length increase. There is only addition of mass to the rim due to retraction, so the rim always grows with time, and thus the retraction rate decreases with time.

The model and experiments are in good quantitative agreement, particularly in the value of the equilibrium rim height at the tip and the velocity of the tip. The model over-estimates the rim thickness at the edge of the hole, but this is probably due to anisotropy, which is not accounted for in the model. Experiments on pre-patterned holes demonstrate that the on-set of the corner instability and edge bending are not coupled. Experiments also show that the corner instability does not depend on the hold size, confirming the model result that no long-range mass transport is involved in the corner instability. Only mass flow within the corner tip region its self is necessary for the instability.

Chapter 7

A 2D model for dewetting of a fully-faceted thin film

7.1 Introduction

The evolution of fully-faceted shapes due to capillarity-driven surface diffusion in two dimensions was treated by Carter *et al.* [15]. They present the framework for developing the equations of motion, as well as an algorithm to simulate surface diffusion for fully-faceted materials. Klinger *et al.* [43] applied their method to test the stability of valley formation during dewetting, and found that it is not favorable for a valley to form when a limited number of facet orientations is available, consistent with experimental observations in strongly-anisotropic systems [27, 8, 43, 34]. The model in this chapter modifies that of Carter *et al.* to include the effects of the substrate to simulate dewetting. Topological changes, such as the introduction of new facets, are included. Simulations using this model offer an understanding of which material properties determine dewetting kinetics, and of the underlying mass flows that generate the characteristic dewetting morphology.

The method begins with the definition of weighted-mean curvature (κ^γ, defined in Chapter 1), the definition of chemical potential, and Fick's first law. These are combined with the condition that volume is conserved, and that for a moving facet to remain flat, the velocity on that facet must be uniform for all s on that facet. Solving these equations and constraints

together gives

$$\mu_i(s) = \mu_i^0 - \frac{J_i}{M_i}s + \frac{v_i}{2M_i}s^2, \tag{7.1}$$

where s is taken to range from zero to the facet-length L_i on each facet, μ_i^0 is the chemical potential on facet i at $s = 0$ (units of Jm^{-2}), J_i is the flux on the facet at $s = 0$ (units of ms^{-1}), M_i is the mobility on the facet times the atomic volume, $M_i = \frac{D_i\Omega}{kT}$, where D_i is the diffusivity (yielding units of $m^4J^{-1}s^{-1}$), and v_i is the normal velocity of the facet, in units of s^{-1}. Multiplying the velocity by the atomic size gives a velocity in m/s.

The boundary conditions on facet i are used to find μ_i^0, J_i, and v_i. The flux of atoms leaving the adjacent facet, $i-1$, must equal the flux entering facet i. Similarly, the chemical potential must be smooth and continuous from one facet to the next. For a shape with N facets, these three conditions provide $3N$ equations for $3N$ unknowns, and thus the shape evolution is known, with [15]

$$v_i = \frac{6M_i(\kappa_i^\gamma - \mu_i) + 3J_iL_i}{L_i^2}. \tag{7.2}$$

The requirements that the mass flux is continuous and that the chemical potential is smooth and continuous provide topological constraints on the shape evolution. These constraints are useful for bounding the possible topologies, discussed below.

For a smooth evolution, the driving force, and therefore the chemical potential, must be finite. This implies that the neighbors of a facet i must have the same orientation as the facet either immediately preceding or following the equivalently-oriented facet on the Wulff shape. If this were not the case, the WMC (weighted-mean curvature) of intervening facets, with length zero, would be infinite unless $\sigma_i = 0$. If a body were fashioned with a corner that is too sharp, the missing facets would instantaneously appear (above 0K) and blunt the corner. This "neighbor constraint" limits the possible geometries.

During shape evolution, the topology may change due to the formation of new facets or removal of existing facets. The former is referred to as "stepping," while the later is "merging." The formation of a step may be thought of as the accumulation of many atomic ledges. During these topological changes, the chemical potential must change continuously with time. If the chemical potential did not change continuously with time, there would be

an instantaneous change in the shape morphology, an infinite driving force, and an infinite flux, which is not physically possible. To satisfy continuity, if a new facet is introduced, it must initially have zero length. Because the WMC is inversely related to L_i and Λ_i is a positive constant, σ_i must be zero to avoid a singularity. Thus, all new facets must have $\sigma_i = 0$, as in Figure 1-2(b). Similarly, all facets that disappear must have $\sigma_i = 0$ so their length can go to zero, and the adjacent facets merge.

Another constraint is that steps can only form at places on existing facets where the chemical potential goes through zero. Introducing a zero length facet where the chemical potential is zero has no detectable effect, and the step can then grow to finite length in the next time instant without discontinuous changes in the chemical potential or morphology.

Finally, steps can only form when

$$\sigma_i \int_0^{L_i} \mu_i(s) ds \geq \Lambda_i \tag{7.3}$$

is satisfied for both pieces of the original facet. If this inequality is not satisfied, the pieces of the original facet will have relative velocities driving them to re-merge.

The work by Carter *et al.*, summarized above, provides a complete description the evolution of fully-faceted bodies via surface diffusion in 2D, which we implement in this work to describe retraction of the edges of thin films.

7.2 Model implementation

The model developed by Carter *et al.* was implemented in Wolfram *Mathematica*. The equilibrium shape for the film, the diffusivity on each facet, and the initial film configuration are the inputs. To treat dewetting, the equilibrium shape of the film was taken to be the Winterbottom shape [83], which is essentially the Wulff construction, but incorporating the substrate-film interfacial energy. The surface energy per unit area on the substrate-film interface is $\gamma_{SF} - \gamma_{SV}$, where SV refers to the substrate-vapor interface and SF refers to the substrate-film interface. This is the relevant quantity because for every unit of SF interface removed during dewetting, a unit of SV is created.

To iterate through time, the chemical potential on each facet is computed using Equations 7.1 and 7.2 and a step is introduced at all points where the chemical potential is zero. The "sense" of the step (whether its normal is that of the preceding facet or the following facet on the equilibrium shape) is opposite the derivative of the chemical potential at the zero point [15]. To ensure that the step is allowed, Equation 7.3 is computed for each half of the host facet. The step is kept only if the inequality is satisfied for both halves. Any steps on the film-substrate interface are discarded.

The surviving steps are checked again, this time for stability with respect to time. If the equality in Equation 7.3 is exactly satisfied, the relative velocities of the two halves are zero. Only steps which will grow in length are kept; steps which would shrink and disappear in the subsequent time step are discarded. This leaves only the steps which are stable. The exact placement of these steps is found using a binary search to choose the position that will make their initial velocity zero.

The stable steps are incorporated into the shape, and the chemical potential, velocity, and flux are recalculated for each facet. If the velocities of adjacent facets will cause them to become coplanar, then the intervening facet must reach zero length and the adjacent facets will merge. This is tested two ways: either the two adjacent facets are separated by a very small distance and have velocities such that they will become coplanar, or the two adjacent facets actually "overshoot" being coplanar, which would cause the intervening facet to change "sense." In either case, a merge occurs.

Finally, the shape is checked for major topological changes, or "breaking." If two corners or edges, which are not adjacent along the s coordinate, are touching (or within a few atomic radii of each other), the film is split into two or more disconnected parts. This occurs, for example, during pinch-off due to film thinning.

With stepping, merging, and breaking complete, the chemical potential, velocity, and flux are again recalculated for each facet. The time step dt is set by the Courant-Friedreichs-Lewy (CFL) condition, *i.e.*, dt cannot exceed $1/v_{\max}$ to ensure numerical stability, where $v_{\max}$ is the speed of the fastest-moving facet on the shape at the current time, in units of s^{-1}. This choice of time step, multiplied by a "safety factor" of 0.001 to ensure numerical convergence, guarantees volume conservation. Each facet is then moved along its normal by

an amount $v_i a_0 dt$, where a_0 is the atomic size, and the whole process is repeated.

In practice, stepping, merging, and breaking are quite rare. Stepping usually occurs in the first time step because the film is far from equilibrium, and the creation of new facets is necessary to accommodate the tremendous flux of material from the film edges onto the top of the film. Merging typically occurs near the end of the evolution, as the two ends of the retracting film meet. Breaking may or may not occur, and depends on a variety of factors, including relative diffusivity values for different facets and the initial aspect ratio of the film, discussed in more detail below.

7.3 Reference film

Edge retraction is discussed below for a reference film with an octagonal Wulff shape (Figure 7-1). This shape is chosen because FCC and BCC materials usually have Wulff shapes which are octagonal in cross-section, *i.e.*, shapes composed of (100), (111), and (110)-type facets. The equivalent contact angle of the film on the substrate is taken to be 90°, resulting in an equilibrium shape equivalent to the Wulff shape truncated at its center (Figure 7-1) [83]. The reference diffusivity is taken to be that of Ni at 900°C on the (100) facet, $D_0 = 5.53 \times 10^{-11}\, m^2/s$ [48]. This value was chosen because it falls roughly in the middle of the range observed for FCC materials [2]. The diffusivity of the substrate-film interface was taken to be $10^{-5} D_0$ because interfacial diffusivities are usually several orders of magnitude smaller than surface diffusivities, and the model is insensitive to this value as long at it is less than $\approx 10^{-2} D_0$. The reference surface energy is taken to be $2.0\, J/m^2$. This was chosen because solid-vapor interfaces for metals typically have surface energies on the order of $0.4 - 4\, J/m^2$ [81], and $2\, J/m^2$ falls in the middle of this range. The reference film shape is 100 μm wide and 100 nm thick. This size was chosen for comparisons with the experiments of Kim *et al.* [34]. The reference annealing time is 24 hours.

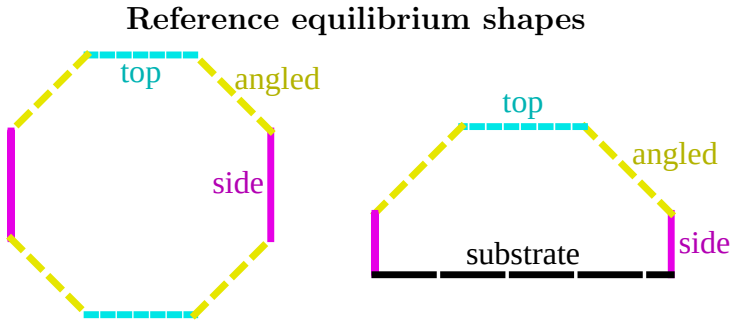

Figure 7-1: The reference equilibrium shapes are shown. Left: the Wulff shape is assumed to be octagonal. There are three crystallographically-distinct facets present: the side facet, the angled facet, and the top facet. Right: the Winterbottom shape for the film. The Wulff shape of the film material is truncated through its inversion center to achieve an equivalent wetting angle of 90°.

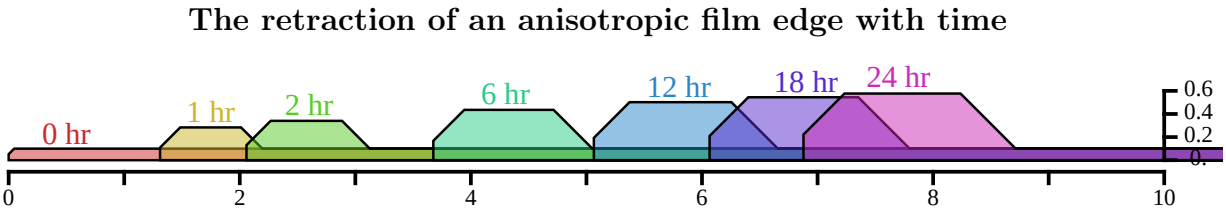

Figure 7-2: The reference film edge profile is shown for various times after the annealing begins. The aspect ratio is 1:1, and the units of both the vertical and horizontal scale are micrometers.

7.4 Results and discussion

7.4.1 Reference film retraction

The evolution of a fully-faceted thin film begins with a change in topology. At time $t = 0$, a step is introduced on the top facet $\tilde{2}00$ nm from each of the film edges. This step initiates the formation of a rim. Subsequently, the rim expands both in height and width as the edges retract (Figures 7-2 and 7-3). The bulk of the film thins linearly with time as material is driven towards to rims. The thinning has a slope of -1.24×10^{-4}/hr, where the current height is normalized to the initial height. Integrated over the first hour of retraction, the bulk film contributes an area of 0.0061 μm^2 to the rim, representing just 3% of the total rim area. The formation of a localized valley is not favorable, and even if one is artificially inserted, it quickly fills and disappears.

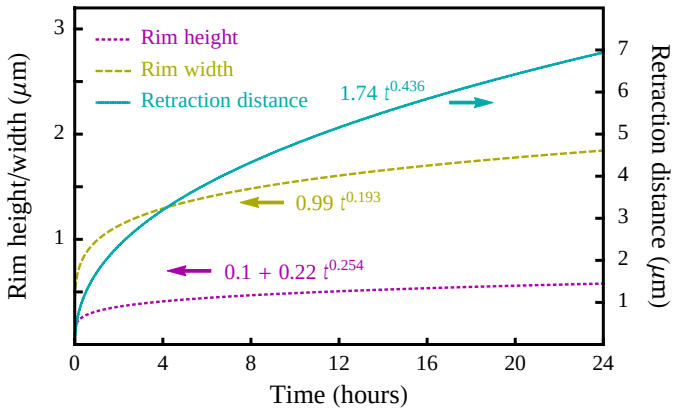

Figure 7-3: The retraction distance, the rim height, and the rim width for the reference film as a function of time. The ct^n fit is shown adjacent to each curve. The rim height fit has the constant included because the rim height at $t = 0$ is 0.1 μm.

7.4.2 Numerical sensitivity

The evolution is initially fast and slows with time. Therefore, the model has a tendency to over-estimate the retraction distance, due to the explicit discretization in time. However, if the CFL condition is satisfied, this overestimation is generally less than a percent, and has first-order convergence as the time step is decreased.

7.4.3 The influence of film parameters on the rate of retraction

Diffusivity anisotropy

Diffusivities were varied for the facets present on the reference film to investigate the influence of diffusivity anisotropy on edge retraction. The results were fit to $x_o = ct^n$, where x_o is the retraction distance, t is time, and c and n are constants, as shown in Figure 7-3. Changes in the diffusivities have strong effects on the absolute magnitudes of the retraction distances (c), but have relatively weak effects on the scaling exponent n. Using the nomenclature in Figure 7-3, the diffusivity on the top facet has the biggest impact on c, the diffusivity of the angled facet has roughly half the effect of the top facet, and the diffusivity on the side facet is inconsequential. These dependancies are illustrated in Figure 7-4. If the diffusivities on the top and side facets are adjusted together, such as in the case of 4-fold symmetry, the

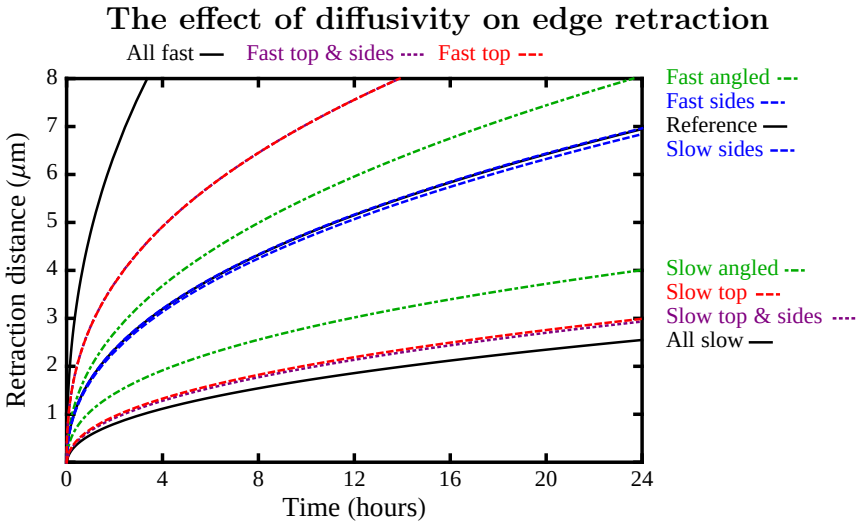

Figure 7-4: The diffusivity on each set of symmetrically-related facets was changed to show its effects on the retraction distance vs. time. The ct^n fit parameters for each curve are listed in Table 7.1.

retraction distance is not significantly different from the case in which the diffusivity on only the top facet is adjusted.

To identify which individual facet has the greatest effect on the retraction rate, the symmetry was broken, and the diffusivity of each facet was adjusted independently. The results are shown in Figure 7-5. The diffusivity on the facet at the top of the rim has the largest influence, followed by the ramp, angled, side, and bulk facets. This ordering can be understood by considering the relationship between the chemical potential and the mass flux, as shown in Figure 7-6. The chemical potential profile evolves to the shape of the one shown in this figure within a few minutes of the start of retraction, and gradually decreases in peak magnitude with time. The diffusivity on the facet which must accommodate the highest flux will set the retraction rate. The larger the chemical potential gradient, the higher the flux, and therefore the more sensitive the retraction rate is to the diffusivity on that facet.

The diffusivity on the bulk facet has almost no effect on the retraction rate, despite being orders of magnitude larger than the other facets. However, its effects are reversed from the rest of the facets. Slowing the bulk facet diffusivity accelerates retraction because the flux of material from that facet is towards the rims. Feeding the rim with material from the bulk offsets diffusion from the triple line.

The diffusivity on each facet and fit parameters for the curves in Figure 7-4

Curvel label	D_{top}/D_0	D_{angled}/D_0	D_{side}/D_0	c	n
Reference	1	1	1	1.740	0.436
All fast	10	10	10	4.795	0.419
All slow	0.1	0.1	0.1	0.585	0.464
Fast top	10	1	1	2.835	0.394
Slow top	0.1	1	1	0.701	0.457
Fast angled	1	10	1	1.996	0.440
Slow angled	1	0.1	1	1.076	0.414
Fast sides	1	1	10	1.745	0.436
Slow sides	1	1	0.1	1.705	0.438
Fast top & sides	10	1	10	2.838	0.394
Slow top & sides	0.1	1	0.1	0.672	0.465

Table 7.1: The diffusivity on each facet and fit parameters for each curve shown in Figure 7-4 are listed.

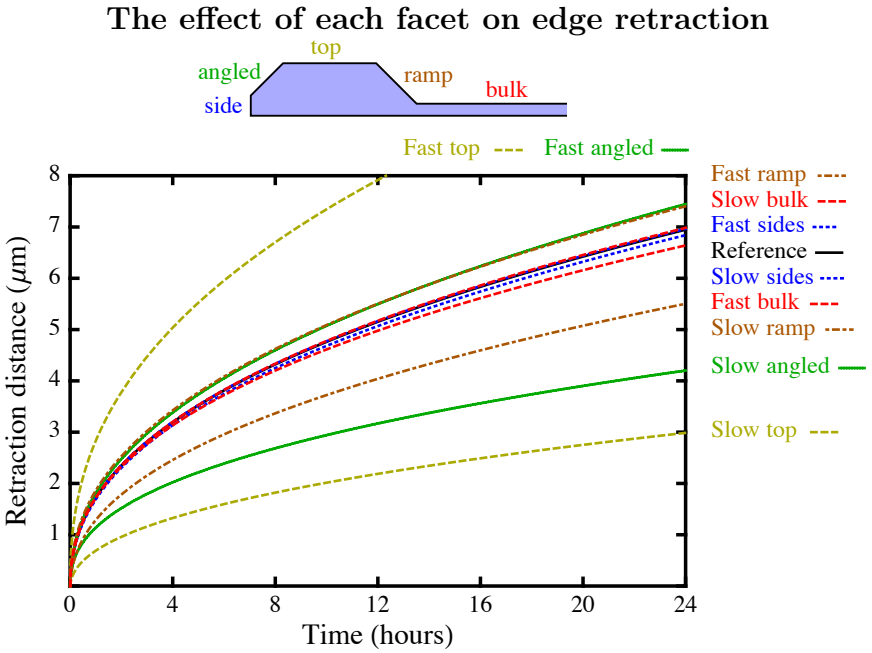

Figure 7-5: The effect of changes in the diffusivity on individual facets on the retraction distance vs. time. The labeling convention is shown in the schematic above the plot. "Slow" corresponds to a diffusivity of 0.1 D_0 on the facet of interest and 1 D_0 on all other facets, while "fast" corresponds to 10 D_0 on the facet of interest. The fit parameters to each curve are tabulated in Table 7.2.

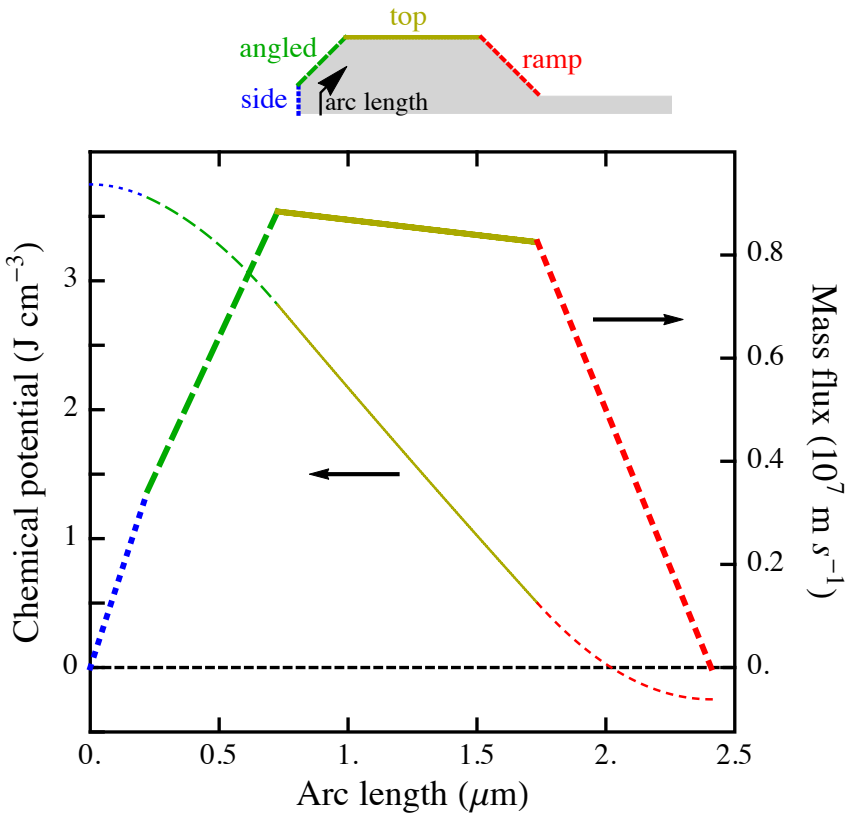

Figure 7-6: The chemical potential and mass flux as a function of the arc length at $t = 24$ hours. The curves are divided into four segments corresponding to the four facets shown in the small figure above the plot. Chemical potential is zero on an infinitely long facet. The chemical potential varies parabolically on each facet with curvature proportional to the normal velocity of the facet. The mass flux is proportional to the derivative of the chemical potential with respect to arc length. The curves for the bulk facet and substrate interface are not shown because they are orders of magnitude larger in length and have fluxes that are several orders of magnitude smaller than the four facets shown. These data are for the reference film.

The diffusivity on each facet and fit parameters for the curves in Figure 7-5

Curvel label	D_{side}/D_0	D_{angled}/D_0	D_{top}/D_0	D_{ramp}/D_0	D_{bulk}/D_0	c	n
Reference	1	1	1	1	1	1.740	0.436
Fast sides	10	1	1	1	1	1.745	0.436
Slow sides	0.1	1	1	1	1	1.705	0.438
Fast angled	1	10	1	1	1	1.826	0.443
Slow angled	1	0.1	1	1	1	1.144	0.410
Fast top	1	1	10	1	1	2.838	0.412
Slow top	1	1	0.1	1	1	0.701	0.457
Fast ramp	1	1	1	10	1	1.877	0.432
Slow ramp	1	1	1	0.1	1	1.309	0.453
Fast bulk	1	1	1	1	10	1.740	0.422
Slow bulk	1	1	1	1	0.1	1.740	0.438

Table 7.2: The diffusivity on each facet and fit parameters for each curve shown in Figure 7-5 are listed.

Value of surface energies

The relative values of surface energy of each facet must fall within a narrow range of each other because the Wulff construction excludes orientations with significantly different energies. For the octagonal Wulff shape explored here with $= \gamma_{\text{top}}$, both facets appear only if $1/sqrt2 \approx 0.707 < \gamma_{\text{angled}}/\gamma_{\text{top}} < \sqrt{2} \approx 1.414$. As a result, changing the relative surface energies has a relatively weak effect on the retraction distance. The retraction distance for $\gamma_{\text{angled}}/\gamma_{\text{top}} = 1.3$ is about 1.24 times faster than that for $\gamma_{\text{angled}}/\gamma_{\text{top}} = 0.8$. The exponent is even more weakly affected by surface energy changes in this range, $n = 0.442$ for $\gamma_{\text{angled}}/\gamma_{\text{top}} = 1.3$ and $n = 0.426$ for $\gamma_{\text{angled}}/\gamma_{\text{top}} = 0.8$.

The effect of relative surface energy is secondary to the effect of differences in diffusivity. Changing the relative surface energy changes the length of each facet exposed during the retraction, allowing the longer facet's diffusivity to have a stronger effect.

While the relative values of the surface energies have a weak effect on the retraction rate, the absolute values of the surface energies have a stronger effect. However, in nature, surface energies generally fall in the range $\approx 0.5\,J/m^2$ to $4\,J/m^2$. The effects of changing γ_0 over this range are shown in Figure 7-7. Again, the exponent is only very weakly affected.

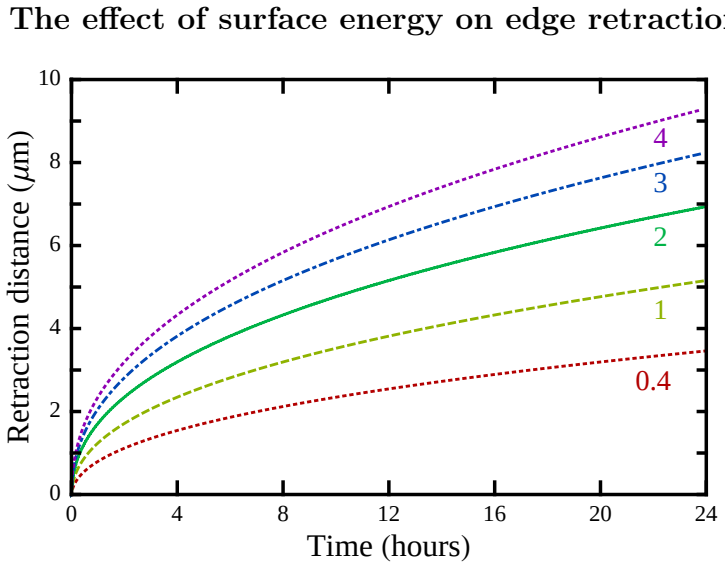

Figure 7-7: The influence of the absolute value of surface energy on the film edge retraction distance vs. time. Each curve is labeled with the surface energy in J/m^2. The ct^n fit to each curve is shown in Table 7.3.

The ct^n fit parameters for each curve in Figure 7-7

Curve label	c	n
0.4 J/m^2	0.794	0.468
1 J/m^2	1.231	0.455
Reference, 2 J/m^2	1.697	0.447
3 J/m^2	2.041	0.443
4 J/m^2	2.323	0.440

Table 7.3: The ct^n fit parameters for each curve in Figure 7-7 are listed.

Effective wetting angle: $\cos^{-1}\frac{\gamma_{SV}-\gamma_{SF}}{\gamma_{FV}}$

The retraction rate is extremely sensitive to $\gamma_{SV}-\gamma_{SF}$, where γ_{SV} is the surface energy of the substrate in contact with vapor and $-\gamma_{SF}$ is the substrate-film interfacial energy. Although the physical contact angle between the film and the substrate is highly constrained by the anisotropy, an equivalent to the isotropic contact angle can be defined as $\cos^{-1}\frac{\gamma_{SV}-\gamma_{SF}}{\gamma_{FV}}$, where γ_{FV} is the surface energy of the top facet. Figure 7-8 shows the results of systematically varying $\gamma_{SV}-\gamma_{SF}$. The film retraction accelerates for higher equivalent contact angles, and approaches zero as the equivalent contact angle goes to zero. The power-law exponent is 1 in the limit of complete wetting and at short times, and approaches 2/5 at long times. The latter is in excellent agreement with the isotropic model [85].

For contact angles less than 65.5°, the Winterbottom shape is trapezoidal, and the side facets are absent. Similarly, for contact angles greater than 114.5°, the Winterbottom shape has eight sides and includes the angled facets below the sides. However, the abrupt transition in topology as the contact angle changes does not cause an abrupt change in the retraction rate. This is because the influence of each facet is proportional to the length of that facet on the Winterbottom shape, so the transition is smooth.

Film thickness

If the width of the film is fixed and the thickness is varied, a strong effect on the retraction rate is observed (Figure 7-9). The total retraction distance per unit time scales as $H^{-1/2}$, where H is the film thickness. The exponent is slightly time-dependent, being -0.520 at $t = 1$ hour and -0.483 at $t = 24$ hours. F or the thinnest film, the exponent in the ct^n fit is 0.382 for the 10 nm-thick film immediately before it undergoes pinch-off by film thinning after 56 hours of retraction. This indicates that 2/5 is not the minimum value the exponent may have.

Film width

The retraction rate is largely insensitive to the initial width of the film. However, the exponent and retraction rate do increase slightly as the film width increases. The retraction

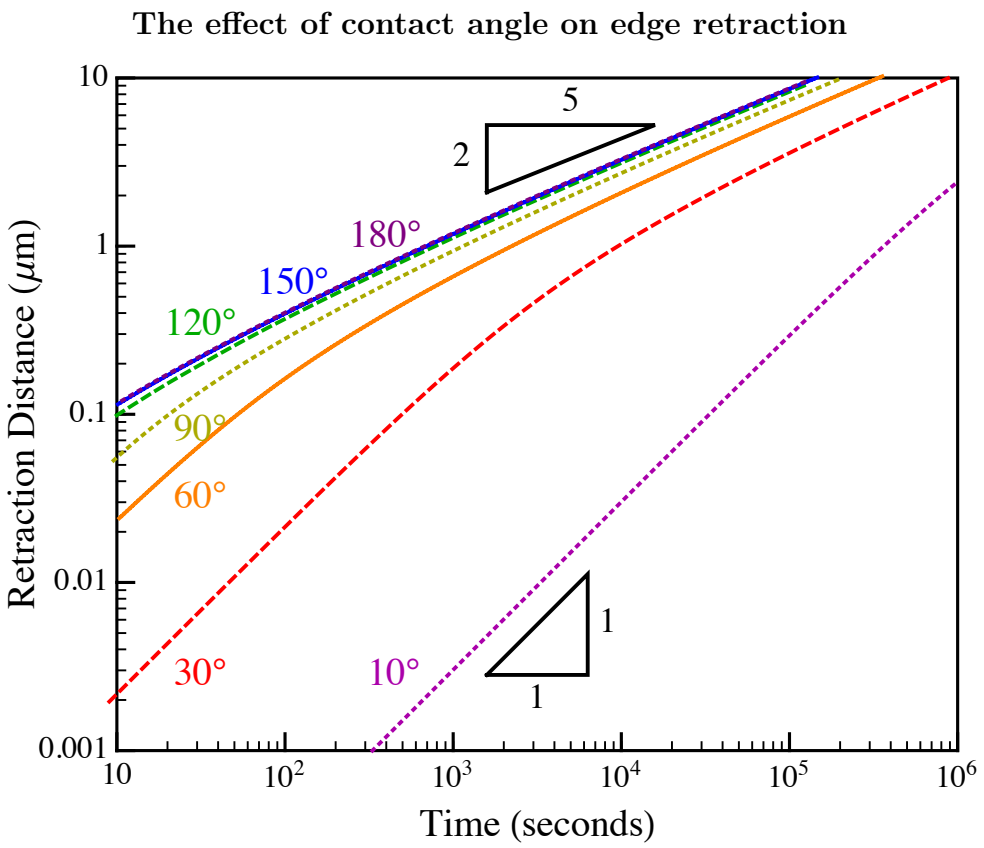

Figure 7-8: The effect of changing the $\gamma_{SV} - \gamma_{SF}$ on the retraction distance vs. time. Each curve is labeled with the equivalent contact angle, $\cos^{-1} \frac{\gamma_{SV} - \gamma_{SF}}{\gamma_{FV}}$.

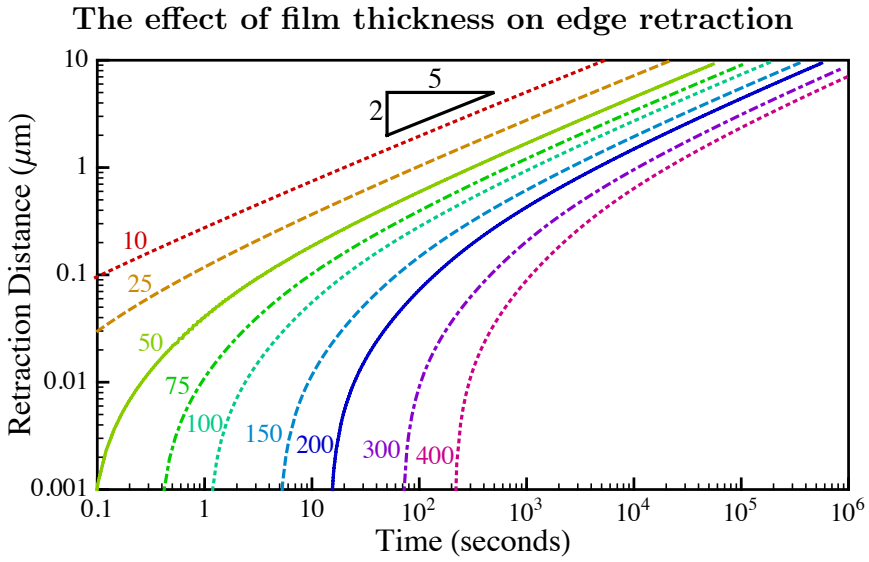

Figure 7-9: The effect of changing the thickness of the film on the retraction distance as a function of time. Each curve is labeled with the thickness of the film, in nanometers.

distance of a 25 μm-wide film is only 8.8% less than that of an 800 μm-wide film. The exponent is 0.418 for the 25 μm-wide film, and 0.443 for the 800 μm-wide film. The width dependence is due to the flux of material from the bulk into the rims. If the diffusivity of the bulk facet is set to $10^{-5}D_0$, there is no width dependence. This follows because the two retracting edges are independent until they impinge. The case of zero diffusivity on the bulk facet represents an "infinitely wide" film. The ct^n power-law fit for 24 hours of retraction is $c = 1.742$ and $n = 0.438$. For 250 -1000 hours of retraction, the power law fit is $c = 1.903$ and $n = 0.415$.

Facet orientation

The orientation of the normal to the angled facet (Figure 7-1) can be changed to represent different crystallographic orientations. The reference film has a 45° normal, as would be the case for a cubic crystal with (001) as the top facet, (110) as the angled facet, and (100) as the side facet. As an example of another common orientation, if the normal is 62.6° above the horizontal, this could represent a slice through a cubic material with (011) as the top facet, (111) as the angled facet, and (100) as the side facet. The model was found to be completely insensitive to the orientation of the angled facet. The exponent in the power law fit was changed by less than 0.1% by changing the orientation. The retraction distance was changed by less than 1%. This follows because the model is essentially one dimensional, tracking properties along the surface coordinate only.

Film edge geometry

The model is insensitive to the initial geometry of the film edge. A nearly rectangular film edge was constructed, having an angled facet which is 4 nm in length and a side facet 96 nm long, and was compared to a nearly trapezoidal film edge, having an angled facet which was 133 nm long and a side facet 6 nm long. After 24 hours of retraction, the retraction distance differed by less than 0.4% due to changes in the film edge profile. This is because the film edge reaches the shape shown in Figure 7-2 very quickly, within about 5 minutes, so it has little time to influence the retraction rate.

Number of facets

The model is insensitive to the number of facets present on the equilibrium shape. The retraction distance of materials with square, hexagonal, and 16-gonal Wulff shapes was found to vary by less than 4% from the retraction distance of a film with the octagonal reference Wulff shape after 24 hours. The exponent of retraction is unchanged. The only systematic differences are that the bulk of the film thins faster and the rim is taller when more facets are present. This implies that in the limit of infinite facets (isotropy), the bulk film would be driven to thin at a high rate and one might expect a valley to form as diffusion can no longer supply material fast enough to achieve uniform thinning.

7.4.4 Comparison with experiments

The properties of Ni at 890°C were input into this model and compared with experimental results for the retraction of 130 nm-thick Ni films on MgO for four crystallographically-distinct orientations. The results of this study are discussed at length in Kim *et al.*, summarized in Figure 3 [34]. Both experiments and the model showed retraction distances varying by nearly a factor of 2, depending on the edge orientation. The model matched experimental results to within 10% for a (001) film with an edge retracting in the [100] direction, and a (011) film with an edge retracting in the [100] direction. The model over-estimated the retraction distance for a (001) film retracting in the [110] direction by nearly a factor of 2, and under-estimated the retraction of a (011) film retracting in the [110] direction by about 50%. The discrepancy between the model and experiment can be accounted for by error in the reported values of diffusivities for Ni on the facets present, and the uncertainty in the interfacial energy between Ni and the MgO substrate.

7.4.5 Pinch-off

This model predicts that localized valleys do not form ahead of the retracting rim with a flat top surface, which is distinct from isotropic and non-fully faceted anisotropic models [85, 27]. Experiments indicate that for fully-faceted films, valleys are absent, in agreement with this model [27, 8, 43, 34]. Even if valleys are artificially introduced in the model at $t = 0$, they

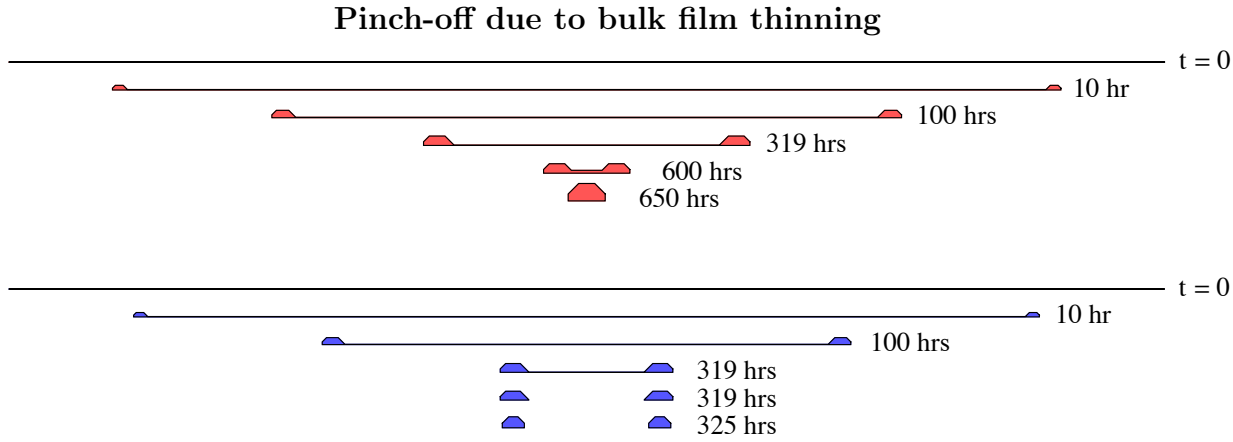

Figure 7-10: Profiles of a (a) 40 nm-thick and (b) 30 nm-thick 100 μm-wide film dewetting until equilibrium is reached. The 40 nm-thick film thins during dewetting, but the rims interact before pinch-off is achieved. The 30 nm-thick film thins until the bulk of the film has zero thickness. The time shown is the number of hours after the initiation of dewetting.

quickly fill in and disappear because they are not stable morphologies. However, the bulk film is thinning, and if the aspect ratio of the film is sufficiently high, the film can thin to zero thickness before the retracting edges meet (Figure 7-10(b)). Bulk thinning means that the film acts as one large valley, donating material to both rims.

For a 100 μm-wide film, pinch-off by film thinning takes a few hundred hours. The thickness for which pinch-off occurs by film thinning in a 100 μm-wide film is between 30 and 40 nm. For thicker films, the rims interact before pinch-off occurs (Figure 7-10(b)) and the thickness at the center begins to go up (Figure 7-11). In this case, the rims merge.

7.4.6 Valley formation

A valley can be produced with this model if there is no equilibrium facet parallel to the substrate, so that the top of the film instead has a sawtooth morphology (Figure 7-12). Such a geometry could be generated if the top surface of a thin film underwent a faceting instability. A faceting instability occurs when a flat physical surface does not correspond to an equilibrium facet (a facet on the Wulff shape). In this case, the originally flat surface becomes composed of alternating equilibrium facets [71, 25].

If the top of the film has a sawtooth morphology, then as the edge retracts, a valley develops (Figure 7-12). The film is initially 100 nm thick on average, and is identical to the

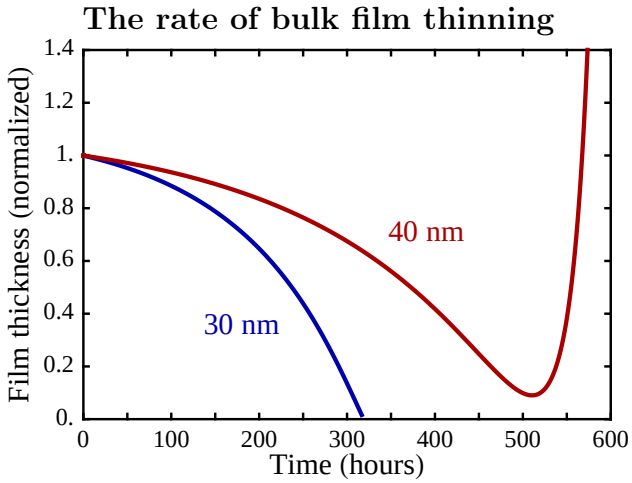

Figure 7-11: The bulk film height normalized to the initial film thickness as a function of time is shown for a 100 μm-wide film. The 30 nm-thick film undergoes pinch-off after 319 hours, and leaves 2 lines of material. The 40 nm thick film initially thins, but as the two rims approach the center, they begin to interact and cause thickening, ultimately merging and leaving a single line of material. The final height of the 40 nm-thick film is 38.6 times its original height.

reference film, except that the octagonal Wulff shape was rotated by 22.5° so that a vertex, not a facet, is at the top of the film. Pinch-off by valley formation is achieved after 57.3 minutes. The final morphology and time to pinch-off is insensitive to the length scale of the sawtooth pattern of facets. The retraction rate up until pinch-off is very similar to that of the reference film. The film profile shows not only a rim and a valley, but also a secondary, smaller rim and valley. This is similar to the isotropic case, which has a decaying, undulatory profile [85].

7.5 Summary and conclusions

A two-dimensional model for the capillarity-driven evolution of bodies with fully-faceted shapes developed by Carter *et al.* [15] was adapted to modeling of solid-state dewetting of fully-faceted thin films. Capillarity-induced retraction of a film edge was studied in detail, and the effects of adjusting various physical parameters on the retraction rate were explored.

The major factors which determine the retraction rate of a thin film, according to this model, are: the film thickness, the atomic diffusivity on the top facet and the angled facet,

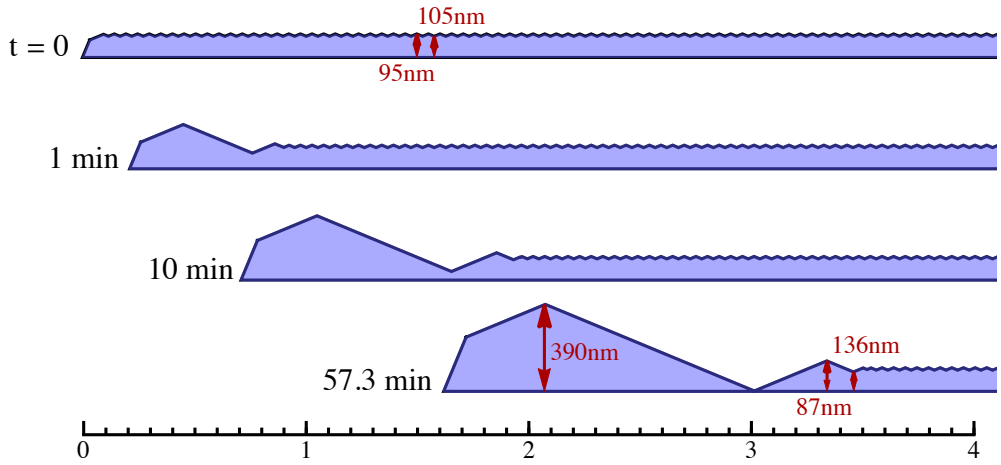

Figure 7-12: The retraction of a film with a sawtooth morphology on the top surface. The scale bar at the bottom is in micrometers.

the equivalent contact angle of the film on the substrate, and the absolute value of the surface energy. The edge retraction distance scales with the film thickness H as $H^{1/2}$.

Although it is not a bad approximation, edge retraction does not obey a power-law because the rim geometry is not self-similar over time. Instead, the length scale of the rim grows relative to the original thickness of the film. The bulk thinning of the film adds to this effect. The same is true for isotropic films, as discussed in Chapter 4. Therefore, no universal value of the power-law exponent n is expected.

When applied to a real system, this model shows good agreement with experimental edge retraction results for the Ni on MgO system, discussed at length by Kim *et al.* [34]. In this case, the retraction distance scales with time as ct^n, where c is a constant and $n \approx 2/5$. The increase in the thickness of the rim and the rim width scale with $n \approx 1/5$. These scaling parameters are not affected by reasonable variations in facet surface energies or the diffusivities on the facets. However, the proportionality constant c is strongly affected by the diffusivities, especially on the top facet. The energy per area of the film substrate interface, which affects the equivalent contact angle, can strongly affect n.

In isotropic models, valleys form ahead of retracting rims and can eventually lead to pinch-off. In experimental studies of single-crystal films, valleys are often absent at retracting edges. The model presented here predicts that pinch-off does not occur through localized

valley formation in fully-faceted films when the top facet is an equilibrium facet. Instead, the entire bulk film acts as the valley, donating material to the rims. However, if a non-equilibrium top facet decomposes due to a faceting instability, valleys do form ahead of the rim and can lead to pinch-off.

Chapter 8

A phase field model for dewetting

8.1 Introduction

Mullins [54] developed an expression that describes the motion of a surface due to capillarity. This equation of motion can describe dewetting by selecting appropriate boundary conditions [75, 85]. Carter *et al.* [15] developed the equivalent equations of motion for a strongly-anisotropic surface, and Zucker *et al.* [96] developed the corresponding dewetting boundary conditions. In general, the governing equations of motion for the surface have no closed-form solution, and must be solved numerically.

Surface diffusion can drive two separate objects to merge, or a split into separate bodies (see Figure 8-1). When anisotropy is present, it may also be necessary to introduce new facets or to remove existing ones. In two dimensions, these topological changes can be managed [85, 96]. However, in three dimensions, the number of possible topological changes becomes intractable.

Using a phase-field method circumvents the issue of managing topological changes. The phase-field method (and the closely-related level-set method) do not explicitly track the position of the interface. Instead, they re-formulate the problem in a higher-dimensional space. The equations of motion apply to every point in the higher-dimensional space, and the interface is represented by a contour, as shown in Figure 8-1. In a phase field, topological changes are trivial. Such changes correspond to a smooth, continuous change of height, rather than a fundamental change in the domain of the problem. The "price" paid for easily

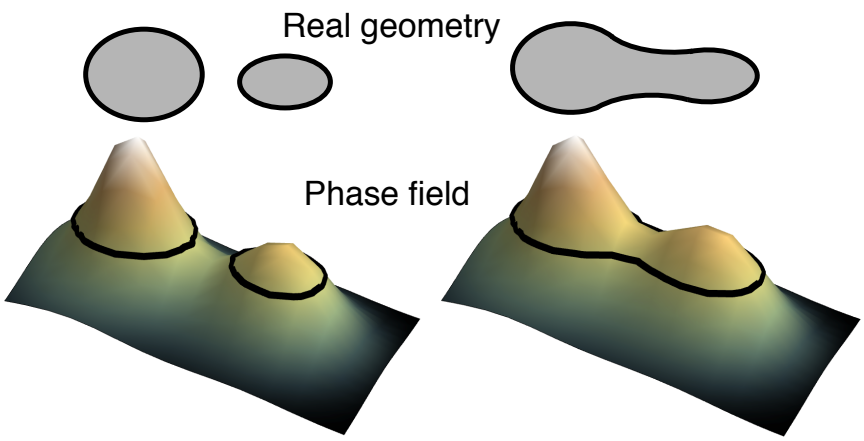

Figure 8-1: A schematic of two example geometries and the corresponding phase field representations are shown. The heavy black line is the interface. The drawings on the left versus on the right show the system before and after a topological change. The phase field does not undergo a topological change, even though the contour line has.

managing topological changes is that the computational domain increases in size: a problem originally confined to a 2D surface becomes a problem in an entire 3D space. In addition, the interface becomes diffuse, rather than sharp, and the equations of motion and boundary conditions must be represented in the phase-field space. The phase-field formulation for dewetting is discussed in the following section.

8.2 Phase-field formulation for dewetting

8.2.1 Isotropic equations of motion

In the case of a sharp interface, the total energy due to capillarity is

$$E = \int_A \gamma(A) dA, \tag{8.1}$$

where A is the interface area and $\gamma(A)$ is the surface energy density of the interface. For an isotropic material, there are three possible values of $\gamma(A)$: γ_{FV}, the film-vapor interface; γ_{SV}, the substrate-vapor interface; and γ_{FS}, the film-substrate interface. The total energy

becomes

$$E = \gamma_{FV} \int_{FV} dA + \gamma_{SV} \int_{SV} dA + \gamma_{FS} \int_{FS} dA, \tag{8.2}$$

where FV, SV, and FS are the film-vapor, substrate-vapor, and film-substrate interfaces.

However, the above expression only works for a sharp interface model. In a phase-field approach, the position of the interface is not known. Therefore, the integral must be taken not just over the surface, but over the entire phase-field domain. An equivalent expression for the total energy is sought that applies for a diffuse interface.

The phase-field parameter ϕ is (arbitrarily) assigned a value of 1 inside the film and 0 in the surrounding vapor. Near the interface, ϕ transitions from one value to the other over a region of characteristic size ϵ. To compute a total energy over the entire phase-field domain that is consistent with the expression for E above, the integrand must be zero where ϕ is constant. Furthermore, the form of the integrand must converge to Equation 8.2 as ϵ goes to zero.

The energy functional

$$E_{FV} = \int_{\Omega} f_{FV} d\Omega, \tag{8.3}$$

where Ω is the phase-field domain, converges to $\gamma_{FV} \int_{FV} dA$ in the small-ϵ limit when f_{FV} is equal to

$$f_{FV} = \frac{3\sqrt{2}\gamma_{FV}}{4} \Big(\frac{1}{\epsilon} f(\phi) + \frac{\epsilon}{2} |\nabla \phi|^2 \Big). \tag{8.4}$$

f_{FV} is the Ginzburg-Landau energy density. The prefactor is the "mixing" energy density, *i.e.*, the energy density in the diffuse interface region [51]. The first term that depends on ϕ is the "double-well potential,"

$$f(\phi) = \frac{1}{4} \phi^2 (\phi^2 - 1). \tag{8.5}$$

It represents the free energy density of a spatially-homogeneous region, and its minima are at 1 and 0 to correspond with the chosen phase-field values in the film and vapor. This homogeneous term effectively penalizes chemical mixing, which drives the film-vapor interface to become thinner. The second term in Equation 8.4 that depends on ϕ is the gradient energy term. It represents the free energy of a spatially-inhomogeneous region, and the faster the change in composition, the larger the penalty. This inhomogeneous term

prevents abrupt changes in phase, which drives the interface to become thicker.

The competition between the homogeneous and inhomogeneous terms in f_{FV} leads to an equilibrium profile across the interface

$$\phi = \frac{1}{2}\Big(1 + \tanh\frac{d}{2\sqrt{2}\epsilon}\Big), \tag{8.6}$$

where d is the signed distance to the center of the interface [79]. This expression shows that the characteristic width of the diffuse interface is $\sqrt{2}\epsilon$.

Equation 8.3 only accounts for the film-vapor interfacial energy. The energy contribution from the substrate interface is found following Jiang *et al.* [36]. The substrate energy integrand f_S must be chosen so that $f_S = \gamma_{FV}$ where $\phi = 0$ and $f_S = \gamma_{FS}$ where $\phi = 1$. The derivative of f_S with respect to ϕ should also vanish far from the triple line so that the free energies of the bulk phases are unaffected by the presence of the substrate. The expression

$$f_S = \frac{\gamma_{SV} + \gamma_{FS}}{2} + \frac{4\phi^3 - 6\phi^2 + 1}{2}(\gamma_{SV} - \gamma_{FS}) \tag{8.7}$$

meets these requirements [35, 91].

In all, the total energy functional for isotropic dewetting is

$$E = \int_\Omega f_{FV} d\Omega + \int_\Gamma f_S d\Gamma, \tag{8.8}$$

where Γ is the substrate surface (this is taken to be the bottom edge of the domain Ω).

The chemical potential μ is the change in energy of a system with change in the volume of a phase. The substrate terms do not contribute to changes in μ because the substrate is immobile. μ should also be independent of the mixing energy density value. Therefore, μ is the first variational derivative of Equation 8.3 with respect to ϕ, divided by the mixing energy density:

$$\mu = \frac{4}{3\sqrt{2}\gamma_{FV}}\frac{\delta E_{FV}}{\delta\phi} = \frac{1}{\epsilon}f'(\phi) - \epsilon\Delta\phi. \tag{8.9}$$

Following Fick's first law, the mass flux $\vec{j}$ is

$$\vec{j} = -M\nabla\mu, \tag{8.10}$$

where M is the mobility. M must be chosen so that only surface atoms can move. With M having the form

$$M(\phi) = \frac{4}{\epsilon}\phi(1-\phi), \tag{8.11}$$

the phase-field equations converge to motion by capillary-driven surface diffusion as ϵ goes to zero [11].

Finally, Fick's second law gives the change in the phase field with time,

$$\frac{\partial \phi}{\partial t} = -\nabla \cdot \vec{j} = \nabla \cdot (M(\phi)\nabla\mu). \tag{8.12}$$

Equations 8.9 and 8.12 together are the equations of motion, and they are equivalent to the Cahn-Hilliard equation, except that the scalar mobility is replaced with a function of ϕ [11].

8.2.2 Isotropic boundary conditions

Jiang *et al.* provide the boundary conditions to treat solid-state dewetting with the above phase-field formulation [36]. There are two boundary conditions on each edge of the computational domain Ω. First, material cannot leave or enter the domain across any boundary, which is enforced when

$$\left|\frac{\partial \mu}{\partial \boldsymbol{n}_b}\right| = 0, \tag{8.13}$$

where $\boldsymbol{n}_b$ is the normal vector to the boundary of the domain. The second boundary condition fixes the gradient in the phase field variable. On the substrate surface, the Young's condition is maintained by satisfying

$$\left|\frac{\partial \phi}{\partial \boldsymbol{n}_b}\right| = -\frac{\phi(\phi-1)}{\sqrt{2}\epsilon}\cos\theta, \tag{8.14}$$

where θ is the equilibrium contact angle between the film and substrate, measured inside the film. The factor of $\phi(\phi-1)$ ensures that $\frac{\partial \phi}{\partial \boldsymbol{n}_b}$ is zero far from the interface, so that the substrate does not affect the chemical potential of the bulk phases. The factor of $\sqrt{2}\epsilon$ is the characteristic width of the interface. This boundary condition is depicted in Figure 8-2.

On all other boundaries, periodic boundary conditions are chosen, which is equivalent to

The dewetting boundary condition in a phase field

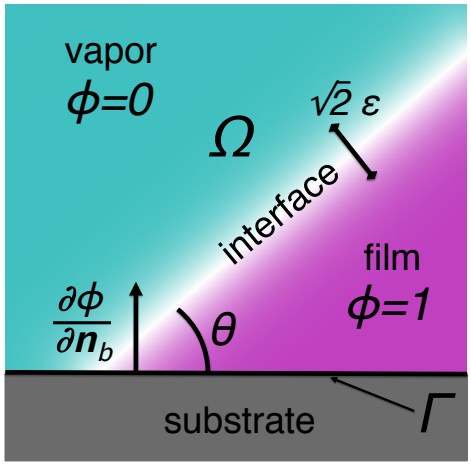

Figure 8-2: The region of the phase field near the triple line (*i.e.*, where the substrate, film, and vapor phases meet) is shown. The substrate is outside the domain volume Ω, and Γ is the edge of Ω that coincides with the substrate surface. The contact angle θ is shown, as is the relevant vector for computing boundary conditions, $\frac{\partial\phi}{\partial \boldsymbol{n}_b}$. The characteristic width of the interface is $\sqrt{2}\epsilon$.

a 90° contact angle:

$$\left|\frac{\partial\phi}{\partial \boldsymbol{n}_b}\right| = 0. \tag{8.15}$$

8.2.3 Anisotropic regularization

Anisotropic surface energies give rise to non-spherical equilibrium shapes. "Weak" anisotropy refers to the case when the surface energy as a function of orientation, $\gamma(\boldsymbol{n})$, is convex everywhere. All orientations are present on the equilibrium shape. "Strong" anisotropy refers to the case when $\gamma(\boldsymbol{n})$ is non-convex, *i.e.*, $d\gamma/d\boldsymbol{n} < 0$ for some orientations. Sharp edges or corners are present on the equilibrium shape, representing discontinuities in the surface orientation.

In a numerical method, discontinuities cannot be represented due to finite spatial resolution, and they cause numerical instability. Therefore, the sharp edges in strongly anisotropic systems must be removed. Rounding the corners can be achieved by the addition of a term to the energy functional that penalizes abrupt changes in orientation.

The Willmore energy is a measure of how much a surface differs from a sphere. For a

closed surface, it is the integral of the square of the Gaussian curvature H, $E_W = \int_s H^2 dA$. Including this energy in the phase field formulation does not significantly alter smooth portions of the geometry, but it does prohibit the formation of sharp corners. Rätz *et al.* developed the phase-field representation of this energy, following De Giorgi:

$$E_W = \frac{\beta}{2\epsilon^3}\int_\Omega H^2 d\Omega = \frac{\beta}{2\epsilon^3}\int_\Omega \left(f'(\phi) - \epsilon^2\Delta\phi\right)^2 d\Omega, \tag{8.16}$$

where $\sqrt{\beta}$ is a small length scale over which the corner is rounded [31, 66]. When simulating strongly anisotropic dewetting, this term is added to the total energy functional to achieve stability.

8.2.4 Anisotropic equations of motion

For isotropic capillary-driven surface diffusion, the film-vapor component of the energy functional (the first term in Equation 8.8) can be written

$$E[\phi] = \int_\Omega \frac{1}{\epsilon}\Big(f(\phi) + \frac{\epsilon^2}{2}|\nabla\phi|^2\Big) d\Omega, \tag{8.17}$$

where $f(\phi)$ is the double-well potential. The natural approach for including anisotropy results in [44]

$$E[\phi] = \int_\Omega \frac{1}{\epsilon}\Big(f(\phi) + \frac{\epsilon^2}{2}|\gamma(\boldsymbol{n})\nabla\phi|^2\Big) d\Omega. \tag{8.18}$$

However, if this energy functional is used, the interface width varies with orientation. This is a problem in the case of strong anisotropy because the Willmore regularization affects each orientation differently.

Torabi *et al.* achieve uniform interfacial thickness by multiplying the entire Ginzburg-Landau energy by the surface energy [79]:

$$E[\phi] = \int_\Omega \frac{\gamma(\boldsymbol{n})}{\epsilon}\Big(f(\phi) + \frac{\epsilon^2}{2}|\nabla\phi|^2\Big) d\Omega. \tag{8.19}$$

Multiplying $f(\phi)$ by $\gamma(\boldsymbol{n})$ still results in convergence to surface diffusion in the small ϵ limit, and it has a negligible quantitative effect on the numerical results. In the case of strong

anisotropy, the Willmore regularization is included in the energy functional

$$E[\phi] = \int_\Omega \frac{\gamma(\boldsymbol{n})}{\epsilon}\Big(f(\phi) + \frac{\epsilon^2}{2}|\nabla\phi|^2\Big) + \frac{\beta}{2}\frac{1}{\epsilon^3}\Big(f'(\phi) - \epsilon^2\Delta\phi\Big)^2 d\Omega. \tag{8.20}$$

Through asymptotic analysis, Torabi *et al.* showed that $f(\phi)$ is approximately equal to $(\epsilon/2)|\nabla\phi|^2$ near the interface. Using this approximation, the equations of motion become [79]

$$\frac{\partial\phi}{\partial t} = \frac{1}{\epsilon}\nabla\cdot\big(M(\phi)\nabla\mu\big), \tag{8.21}$$

$$\mu = \frac{1}{\epsilon}\Big(\gamma(\boldsymbol{n})f'(\phi) - \epsilon^2\nabla\cdot\boldsymbol{m}\Big) + \beta\frac{1}{\epsilon^2}\Big(f''(\phi)\kappa - \epsilon^2\Delta\kappa\Big), \tag{8.22}$$

where

$$\boldsymbol{m} = \gamma(\boldsymbol{n})\nabla\phi + |\nabla\phi|\boldsymbol{P}\nabla_n\gamma(\boldsymbol{n}), \tag{8.23}$$

$$\kappa = \frac{1}{\epsilon}\Big(f'(\phi) - \epsilon^2\Delta\phi\Big), \tag{8.24}$$

$\boldsymbol{n}$ is the outward normal vector

$$\boldsymbol{n} = -\frac{\nabla\phi}{|\nabla\phi|}, \tag{8.25}$$

and P is the projection matrix

$$\boldsymbol{P} = \boldsymbol{I} - \boldsymbol{n}\otimes\boldsymbol{n}. \tag{8.26}$$

Even with the simplifying approximation, the system converges to surface diffusion in the small ϵ limit [79]. However, the cost of regularization is an increase in the order of the equations of motion from 4^{th} order to 6^{th} order.

8.2.5 Anisotropic dewetting boundary condition

For isotropic systems, the contact angle between the film and substrate is simply a number, θ. For anisotropic systems, the apparent contact angle will be a function of the normal to the interface. Thus, the contact angle θ is replaced by $\theta(\boldsymbol{n})$.

For example, consider a four-fold symmetric surface energy

$$\gamma(p,q) = 1 + \chi(\sin^4 p(\cos^4 q + \sin^4 q) + \cos^4 p), \tag{8.27}$$

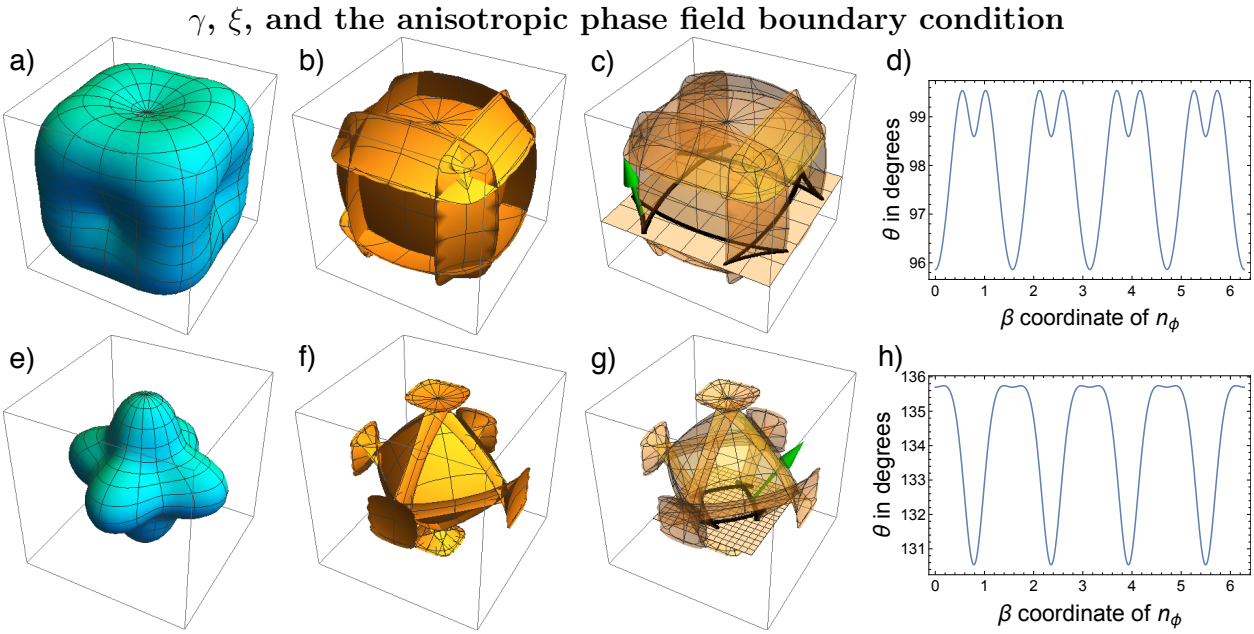

Figure 8-3: The γ-plot (blue), ξ-plot (orange), truncated ξ-plot (transparent orange), and contact angle (blue curve) for χ = -0.5 (top row) and χ = 2 (bottom row) are shown. In figures c) and g), the plane of the substrate is shown with an equivalent contact angle of 120°. The heavy black line is the intersection between the ξ-plot and the substrate plane. The green arrow is an example of $\frac{\partial \xi}{\partial p}$ evaluated at the ξ-substrate intersection. This arrow is dotted with the substrate normal $\boldsymbol{n}_b$ to find the contact angle as a function of the phase field interface orientation $\boldsymbol{n}$.

where χ is the anisotropy parameter and p and q are the "latitude" and "longitude" spherical coordinates, respectively. p and q are used instead of the traditional θ and ϕ to avoid confusion with the contact angle and phase-field parameter, respectively.

The equilibrium shape defined by this γ-plot will be the convex region on the corresponding $\vec{\xi}$-vector. It is defined as

$$\vec{\xi} = \nabla \gamma_{\text{ext}}, \tag{8.28}$$

where

$$\gamma_{\text{ext}} = |\vec{A}|\gamma(\boldsymbol{n}) = |\vec{A}|\,\gamma\left(\frac{\vec{A}}{|\vec{A}|}\right) \tag{8.29}$$

is an extensive measure of surface energy that scales with the area of the surface. The area vector is defined $\vec{A} = A\boldsymbol{n}$, with A being the area of the surface. Example γ- and ξ-plots are shown in Figure 8-3.

The ξ-plot requires modification to satisfy the contact angle of the film on the substrate.

According to the Winterbottom construction [83], the center of the ξ-plot is displaced relative to the substrate surface by a distance $d = \gamma_{SV} - \gamma_{SP}$, where the γ's are surface free energy densities for the substrate-vapor interface (SV) and substrate-particle interface (SP). Any portion of the ξ-plot that falls below the substrate plane is truncated.

In practice, γ_{SV} and γ_{SP} are rarely known. Instead, the equivalent contact angle is typically reported, in degrees. The equivalent contact angle, defined by Zucker *et al.* [94], is $\theta_{\text{equiv}} = \cos^{-1} \frac{d}{\gamma_{PV}}$, where γ_{PV} is the surface free energy of the particle-vapor interface. γ_{PV} is defined as the distance from the center of the ξ-plot to the lowest surface of the ξ-plot (*i.e.*, the ξ value that would appear on the equilibrium shape, rather than on the "ears" of the ξ-plot), measured in the direction normal to the substrate, $\boldsymbol{n}_b$.

As an example, let the equivalent contact angle be 120°. Following from Equation 8.27, $\gamma_{PV} = 1 + \chi$, so $d = -\frac{1+\chi}{2}$. Therefore, the center of the ξ-plot should be raised a distance $\frac{1+\chi}{2}$ above the substrate plane.

To find the intersection of the ξ-plot with the substrate plane, the z-component of the ξ-vector is set equal to d, and solved for p. This particular value of the coordinate p, p^*, will depend on q and χ. The resulting parametric curve, $\xi(p^*(q,\chi), q, \chi)$, is shown as the heavy black curve in Figures 8-3(c) and 8-3(g).

The displaced ξ-plot can be used to construct the dewetting boundary condition. The derivative of ξ with respect to p is evaluated when $p = p^*$ to give the tangent vector to the ξ surface that is normal to the intersecting curve $\xi(p^*(q,\chi), q, \chi)$. Examples of this tangent vector are shown as the green arrow in Figures 8-3(c) and 8-3(g). Finally, the apparent contact angle as a function of interface orientation, $\theta(\boldsymbol{n})$, is

$$\theta(\boldsymbol{n}) = \frac{\pi}{2} \pm \cos^{-1}\left(\left(\frac{\partial \vec{\xi}}{\partial p} \right)_{p=p^*} \cdot \boldsymbol{n}_b \right). \tag{8.30}$$

The addition of $\pi/2$ makes the contact angle relative to the substrate plane, instead of the normal to the substrate plane. If the effective contact angle θ is less than 90°, then a minus sign is used in Equation 8.30. For larger contact angles, a plus sign is used.

The end result is the dewetting boundary condition for anisotropic materials. On the

substrate surface, the equivalent contact angle condition is maintained by satisfying

$$\left|\frac{\partial\phi}{\partial \boldsymbol{n}_b}\right| = -\frac{\phi(\phi-1)}{\sqrt{2}\epsilon}\cos\left(\theta(\boldsymbol{n})\right) \tag{8.31}$$

8.3 Numerical method

8.3.1 Challenges

The governing equations for dewetting are non-linear, fourth-order PDEs (partial differential equations). With strong anisotropy, the governing equations are sixth-order. The high order of the governing equations eliminates finite difference and finite volume numerical approaches. For a typical scheme such as the explicit finite-difference method, the maximum time step allowable that maintains numerical stability scales with the grid size, Δx, raised to a power equal to the order of the equations. In this case, $\Delta t \approx \Delta x^4$ or Δx^6. When the grid size is small enough to resolve the surface evolution accurately, the time steps become miniscule, and the total computation time becomes impractical. The finite element method scales better for higher order equations, so it is the most practical approach for dewetting problems.

Implicit solvers (numerical methods which assume the new value at time $t+\Delta t$ is a function of the new value) generally offer larger stable time steps that explicit solvers (numerical methods which assume the new value at time $t+\Delta t$ is a function of the old value only). However, only linear terms (*i.e.*, terms which are invertible when written as a matrix) can be made implicit, and none of the terms in the phase-field dewetting scheme are linear. At best, surface diffusion problems can be solved semi-implicitly. Including implicit stabilization terms that penalize large changes in ϕ with time have also been successfully implemented to increase the time step size, without affecting the shape evolution [36].

There are other tools available to overcome the inherent speed problems for simulating dewetting. Adaptive meshing, which increases the density of grid points only near the interface, significantly reduces computation time. Adaptive time steps, which are small when a topological change happens and large in between events, can also dramatically improve computation time. Finally, parallelization allows several processors to share the problem,

which is especially effective for problems requiring a large spatial domain.

In summary, simulating capillary-driven surface diffusion requires start-of-the-art mathematical and numerical techniques, and even then, it requires significant computational resources. Using an adaptive grid, adaptive time-stepping, parallelization, implicit stabilization, and Willmore regularization, all within an efficient finite-element scheme, it is possible to simulate dewetting.

8.3.2 Discretization of the governing equations

Equations 8.21, 8.22, and 8.24 together form a system of coupled second-order equations. They can be written semi-implicitly as follows:

$$\frac{\phi^n - \phi^{n-1}}{\tau^n} = \frac{1}{\epsilon}\nabla \cdot \big(M(\phi^{n-1})\nabla\mu^n\big), \tag{8.32}$$

$$\mu^n = \frac{1}{\epsilon}\gamma(\boldsymbol{n}^{n-1})f'(\phi^n) - \epsilon\nabla\cdot\big(\gamma(\boldsymbol{n}^{n-1})\nabla\phi^n\big) - \epsilon\nabla\cdot\big(|\nabla\phi^{n-1}|P\nabla_{\boldsymbol{n}^{n-1}}\gamma(\boldsymbol{n}^{n-1})\big) + \beta\frac{1}{\epsilon^2}\big(f''(\phi^{n-1})\kappa^n - \epsilon^2\Delta\kappa^n\big), \tag{8.33}$$

$$\kappa^n = \frac{1}{\epsilon}f'(\phi^n) - \epsilon\Delta\phi^n, \tag{8.34}$$

where the superscripts refer to the value at timestep n or $n-1$, and τ^n is the time step size. The term $f'(\phi^n)$ can be linearized: $f'(\phi^n) = f'(\phi^{n-1}) + f''(\phi^{n-1})\big(\phi^n - \phi^{n-1}\big)$ [69]. Making this substitution and re-arranging results in the following linear equation

$$\begin{pmatrix} \frac{1}{\tau^n} & A & 0 \\ B & 1 & \frac{\beta}{\epsilon}C \\ C & 0 & 1 \end{pmatrix} \begin{pmatrix} \phi^n \\ \mu^n \\ \kappa^n \end{pmatrix} = \begin{pmatrix} \frac{\phi^{n-1}}{\tau^n} \\ D \\ E \end{pmatrix} \tag{8.35}$$

where

$$A = -\frac{1}{\epsilon}\nabla \cdot \big(M(\phi^{n-1})\nabla\big) \tag{8.36}$$

$$B = -\frac{1}{\epsilon}\gamma(\boldsymbol{n}^{n-1})f''(\phi^{n-1}) + \epsilon\nabla\cdot\big(\gamma(\boldsymbol{n}^{n-1})\nabla\big) \tag{8.37}$$

$$C = \epsilon\Delta - \frac{1}{\epsilon}f''(\phi^{n-1}) \tag{8.38}$$

$$D = -\epsilon\nabla\cdot\left(|\nabla\phi^{n-1}|P\nabla_{\boldsymbol{n}^{n-1}}\gamma(\boldsymbol{n}^{n-1})\right) + \gamma(\boldsymbol{n}^{n-1})E \tag{8.39}$$

$$E = \frac{1}{\epsilon}\left(f'(\phi^{n-1}) - f''(\phi^{n-1})\phi^{n-1}\right). \tag{8.40}$$

This is equivalent to the scheme found by Salvalaglio *et al.* [69]. For weak anisotropy, the third row is dropped and $\beta = 0$.

8.3.3 Computation

To implement a finite-element numerical method, we chose to use AMDiS [80]. AMDiS is a general C++ library to solve PDEs which includes adaptive grids, adaptive time steps, and parallelization.

Several minor modifications were made to the model to improve numerical stability. In Equation 8.35, the "1" in position $(2,2)$ of the matrix is replaced by $30(\phi^{n-1})^2\big(1-(\phi^{n-1})^2\big)^2$. This modification ensures that the chemical potential is zero away from the interface [42, 66, 69]. To include the stabilizing term $\Delta(\phi^{n-1}-\phi^n)$, the Laplacian operator is added to the "$1/\tau^n$" term in position $(1,1)$ of the matrix in Equation 8.35, and to the "ϕ^{n-1}/τ^n" term in the first position of the vector on the right-hand side of the equation. This stabilizing term prevents rapid changes in the value of ϕ [36]. The mobility $M(\phi) = 4/\epsilon\,\phi(1-\phi)$ was replaced by $M(\phi) = 4/\epsilon\sqrt{16\phi^2(1-\phi)^2+10^{-6}}$ to keep the mobility from going to zero, which is problematic when dividing by M [79].

8.4 Results and Discussion

The phase field method produces the correct equilibrium shape, as shown in Figure 8-4. The example shape has anisotropy factor $\chi = 0.25$ in the γ-function, given by Equation 8.27, and the equivalent contact angle is 120°. The triple line from the simulation is shown in blue in Figure 8-5, and it matches the exact solution for the triple line position (black). If a constant contact angle of 120° was chosen, the mean radius of the triple line would be much larger than it should, and the equilibrium shape would be badly distorted. The red curve in Figure 8-5 is for a constant contact angle equal to the average contact angle given by Equation 8.30. While it is better than using the equivalent contact angle, a constant contact

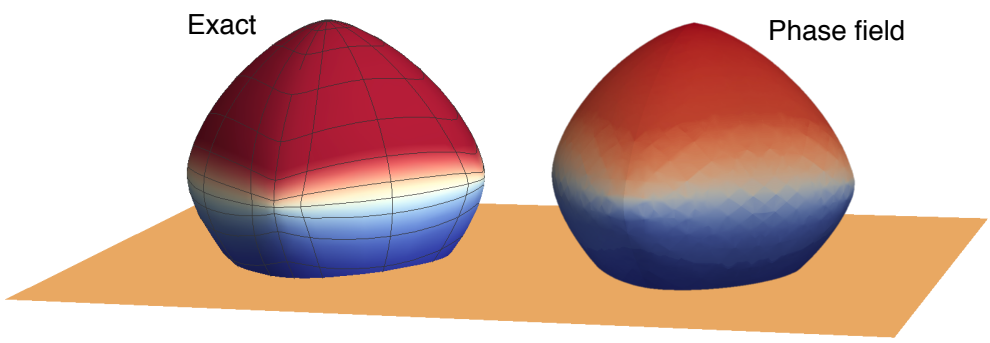

Figure 8-4: A sphere was evolved using the method described in this chapter to obtain the equilibrium shape. The exact solution for the Winterbottom shape is shown for comparison.

angle still introduces error.

Figure 8-6 shows the development of a perturbed rim into a fingering instability. This simulation is isotropic and has a 90° contact angle, the film edge initially has a sinusoidal perturbation with amplitude 0.2, and the film thickness is 1. A half-wavelength is shown, and the mirror boundary conditions make this equivalent to an infinite, straight film edge with a perturbation wavelength of 20 times the film thickness. At first, the amplitude of the perturbation decreases as the shape of the film edge adjusts. At a dimensionless time of about 0.3, the amplitude of the perturbation starts to increase, and after a dimensionless time of about 2.0, the perturbation amplitude is positive and increases linearly with time. This behavior is independent of the initial perturbation size.

Figure 8-7 shows the Rayleigh instability on a perturbed cylinder. This simulation is isotropic and has a 90° contact angle, the cylinder radius is initially 1, with a perturbation amplitude of 0.1. The mirror boundary conditions have been applied to visualize several repeats of the cell. The perturbation wavelength is 9, which is very close to the fastest-growing wavelength for a Rayleigh instability in this case, $2\sqrt{2}\pi \approx 8.9$. The cylinder breaks up due to surface area minimization and evolves to the equilibrium shape (a hemisphere) by surface diffusion.

Figure 8-8 shows the influence of weak anisotropy on the rim profile. The γ-function has the form shown in Equation 8.27, restricted to two dimensions. The valley is broad and shallow for the square Wulff shape, and the valley is narrow and deep for the diamond Wulff

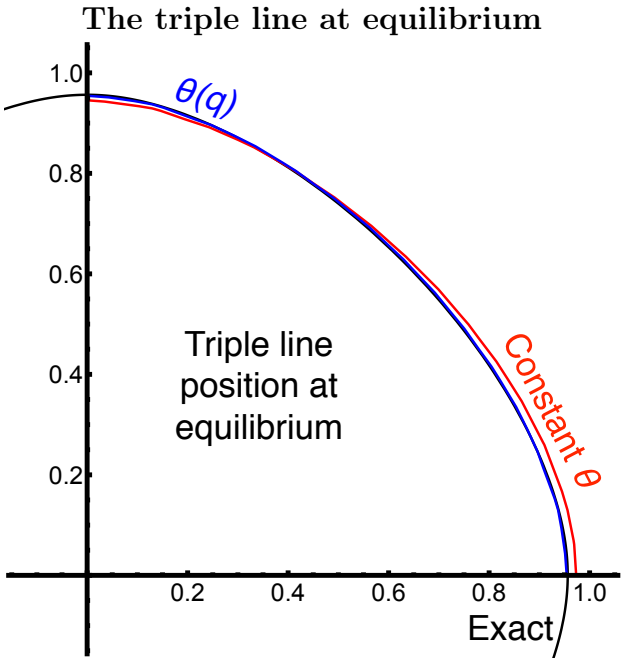

Figure 8-5: The triple line of the equilibrium shape is plotted for the exact solution (black), a constant contact angle of 127.95° (red), and a variable contact angle following Equation 8.30, which corresponds to an equivalent contact angle of 120° (blue).

shape. Relative to the isotropic film, pinch-off happens earlier for the diamond and later for the square. As the anisotropy factor χ increases in magnitude, the valley width increases and depth decreases for the square case. This seems to agree with the limiting case of strong anisotropy (see Chapter 7), where the valley width goes to infinity.

Figure 8-9 shows a film edge with strong anisotropy (*i.e.*, it has missing orientations). The film undergoes a faceting instability, unlike the weakly-anisotropic diamond case in Figure 8-8, which differs only in the value of χ. The faceting instability first propagates ahead of the retracting edge with a wavelength of 2.04. After a dimensionless retraction distance of about 5, the entire film spontaneously and rapidly undergoes a faceting instability with a wavelength of 2.60. The difference in wavelength shows that the spontaneous instability is not related to a perturbation originating from the retracting edge.

The faceting instability is the result of spinodal decomposition of an unstable surface orientation into two or three orientations which appear on the Wulff shape [10]. The faceting instability wavelength is governed by the ratio of the excess free energy associated with sharp edges or corners, $C(\theta)$, to the surface energy and stiffness of the unstable orientation,

Phase field simulation of the fingering instability

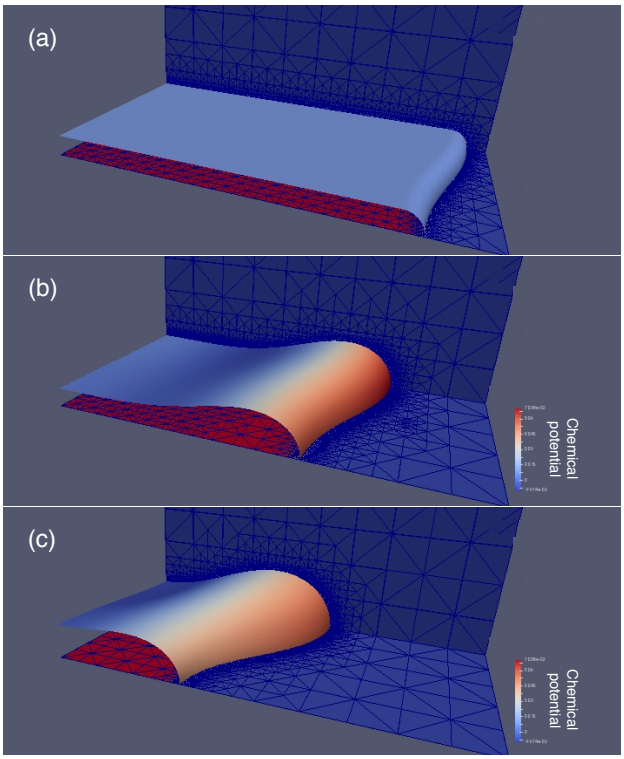

Figure 8-6: An initially-perturbed rim, (a), and its subsequent evolution, (b and c), is shown. In (b), the rim height is nearly uniform, while in (c), the rim is thinner where it has retracted further, consistent with a fingering instability. The adaptive grid is shown in blue. In (b) and (c), the film surface its self is colored by chemical potential. The lower bound of the domain is the substrate surface, and it is blue where it contacts vapor and red where it contacts the film.

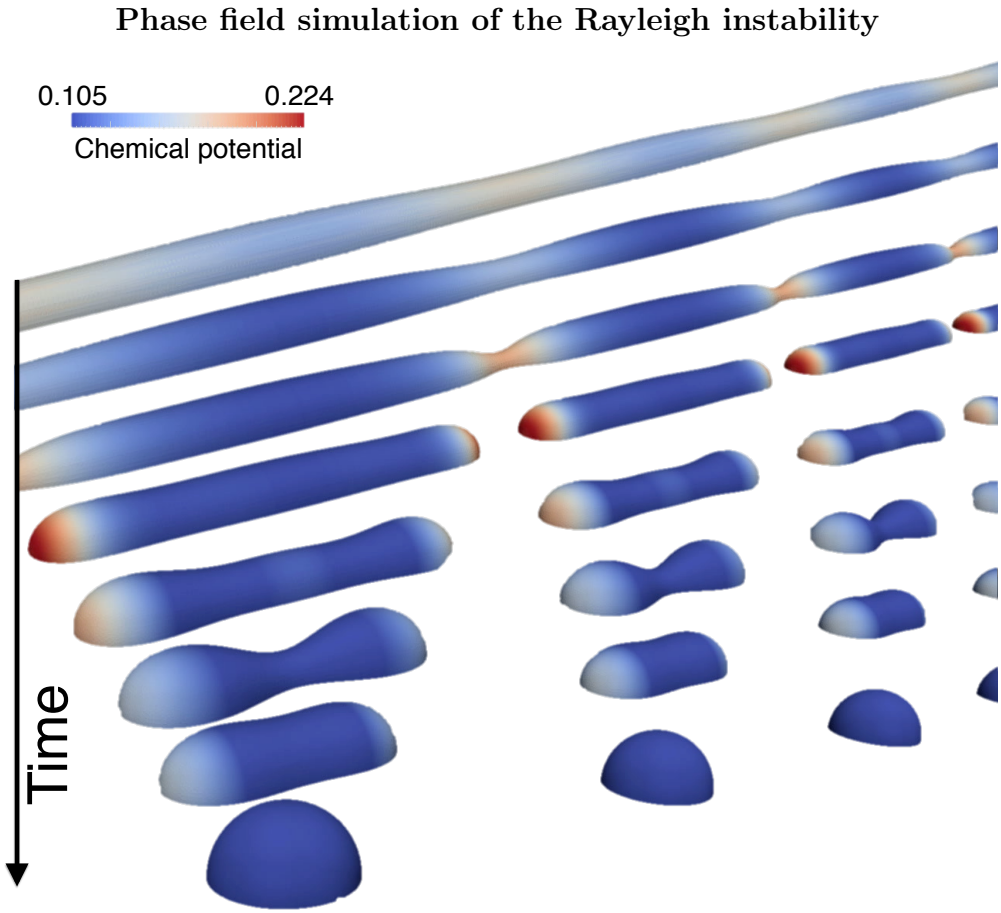

Figure 8-7: A cylinder is initially perturbed and breaks up due to the Rayleigh instability by surface diffusion. The surface is colored by chemical potential. The time between images is not uniform.

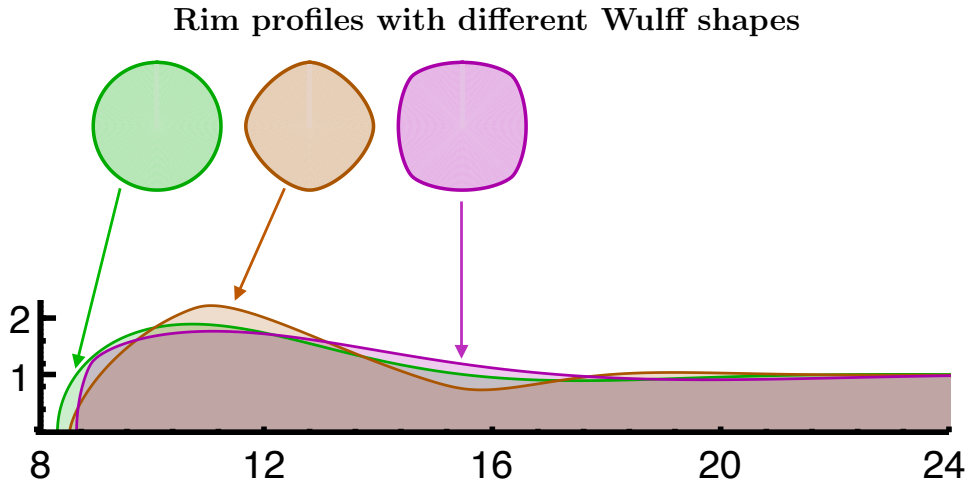

Figure 8-8: A thin film edge at the same dimensionless time for three different Wulff shapes is shown. The green curve is isotropic, the pink curve has a square Wulff shape with anisotropy factor -0.15, and the orange curve has a diamond Wulff shape with anisotropy factor 0.15.

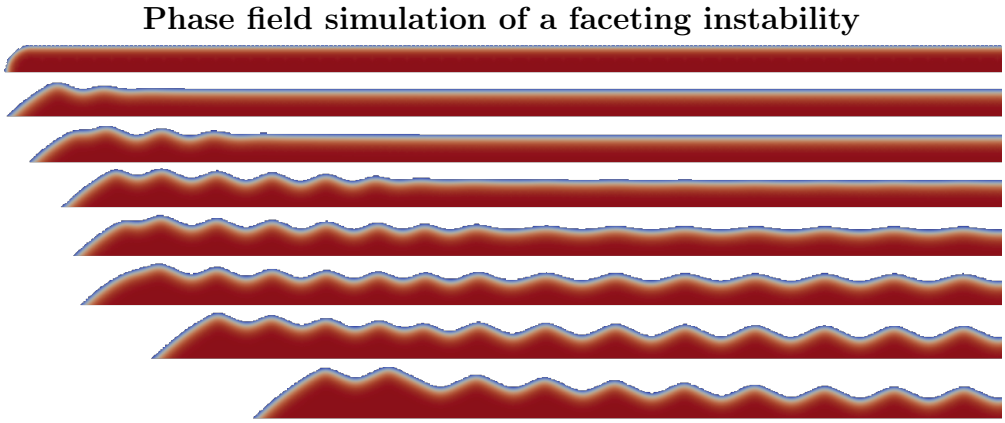

Figure 8-9: A thin film edge with a strongly-anisotropic Wulff shape ($\chi = -0.6$) retracts and undergoes a faceting instability. The facets that form ahead of the retracting rim have a wavelength of 2.04 times the film height, while the facets that form spontaneously have a wavelength of 2.60 times the film height. The film is colored by the value of the phase field variable ϕ to show the interface thickness. The time between frames is not constant.

$\gamma(\theta) + \gamma''(\theta)$. Wavelengths longer than $\lambda_{\text{crit}} = 2\pi\sqrt{C(\theta)/|\gamma(\theta) + \gamma''(\theta)|}$ are unstable, and $\sqrt{2}\lambda_{\text{crit}}$ is the fastest-growing wavelength [26]. While it is extremely difficult to measure the corner energy and stiffness experimentally, these are known in the phase field simulation. For the simulation in Figure 8-9, the critical faceting wavelength is 1.72, and the fastest-growing wavelength is 2.43. The spontaneous instability wavelength is close to (but slightly larger than) the expected wavelength.

8.4.1 Limitations of the phase field approach

Premature pinch-off

In real systems, the interface width is on the order of a few atomic layers, which is usually several orders of magnitude smaller than the body. In the phase field simulation, the interface must have a thickness that can be resolved by the mesh. Even with adaptive grids, to obtain simulation results on reasonable timescales (*e.g.* a few days on several cores), the interface width w should be on the order of 0.1 times the film thickness. This thick interface is problematic for topological changes and near the boundaries of the simulation domain. Two material surfaces which should have no interaction at all begin to interact over a distance of about $2w$, and the film interacts with the domain boundary over a distance w. The large

curvatures that occur during topological changes accelerate merging and breaking of bodies in the simulation, leading to an under-estimation of the time until the topological change.

An example of this limitation occurs in the geometry shown in Figure **??**. When the film thins under the valley to less than about 0.2 of the original film thickness, interactions with the substrate accelerate film thinning. Pinch-off occurs far earlier than it should, compared with explicit interface models **??**. The time to pinch-off depends on the interface width, which is purely an artifact of the method.

Small time step required

The convergence of the phase field simulation is first order as the time step size goes to zero. Furthermore, the interface width and maximum stable time step are linked. This means that the simulation may be numerically stable, but quantitative information which depends on time, such as the retraction rate versus time, or processes that depend on interface width, such as pinch-off, can be unreliable, even with the adaptive time step algorithm. It is possible to do all simulations with sufficiently small time steps and thin interface widths to obtain quantitative information, but each run would take weeks on 4-12 cores. Therefore, it is preferable to obtain qualitative information about dewetting morphologies using a large time step so that each run takes hours or a few days on the same number of cores, but the time scaling in these cases is meaningless. If quantitative information is desired, then it is only practical to run the simulation for a few time steps. For example, simulations which give the growth rates of perturbations to the film surface are attainable because only the initial surface velocities are needed to make a comparison with theoretical growth rates.

8.5 Conclusions

The boundary condition for anisotropic dewetting was previously unknown. Comparison between simulations and the exact solution show that the boundary condition developed in this work successfully reproduces the Winterbottom shape in a phase field simulation and accurately places the triple line.

The phase field method can be used to simulate dewetting with weak and strong anisotropy

in two and three dimensions. Only a few examples are presented here. Despite the limitations of a diffuse-interface model, several dewetting phenomena have been successfully simulated. Future work includes systematic, quantitative studies of dewetting features, including shape instabilities and the influence of anisotropy on shape evolution.

Chapter 9

Conclusions

The models presented in this thesis are interlinked. Thermodynamic study (Chapter 2) provides the framework to understand the final state of dewetting. Quantifying the driving forces during surface diffusion, which is done in every chapter in this work, is only possible with knowledge of the equilibrium state. The polygonal geometry of fully-faceted films (Chapter 7) makes it especially easily to visualize and quantify driving forces and mass flows. The insights gained from the fully-faceted model became core assumptions in the geometric model of edge retraction (Chapter 4), the fingering instability analysis (Chapter 5), and the corner instability model (Chapter 6). The expectations derived from these analytical models determined which geometries to investigate with phase field simulations (Chapter 8). Simulations provide definitive comparisons with experiments, but they are expensive, so iteration between simple models, simulations, and experiments provided an efficient route to study dewetting phenomenology.

In addition, two themes emerge from this work which can be applied to geometries other than thin films:

Processes facilitated by surface diffusion are local. Phenomena which were previously assumed to be driven by long-range mass transport (*e.g.* the fingering [75, 40] and corner [88, 78, 63] instabilities) are better explained by mechanisms which require only local, short-range transport, as shown in Chapters 5 and 6. The hill-and-valley geometry (Chapters 4 and 7) is a hallmark of surface diffusion, a consequence

of its local character, and can be seen on other geometries such as isolated bodies [15], wires or pillars [5], channels [62], and pyramids or microfacets [84, 79].

Isotropic and anisotropic systems behave similarly. Although it is easy to focus on the differences between isotropic and anisotropic systems because they have such different overall behavior (*e.g.*, isotropic dewetting is dominated by periodic pinch-off, while anisotropic dewetting is dominated by corner instabilities), all mechanisms are present in both the isotropic and anisotropic limit, and the only difference is the rate of each mechanism. For example, anisotropic materials have valleys too, but because they are not very deep, pinch-off is so slow (as discussed in Chapters 7 and 8) that other mechanisms have time to dominate instead. When it comes to the edge retraction rate and underlying mass flows, isotropic and anisotropic films are indistinguishable (Chapter 4). Meanwhile, the mechanism of the corner instability is not unique to anisotropic films, but anisotropy enhances the effect (discussed in Chapter 6).

9.1 Edge retraction and valley formation

Chapters 4 and 7 reveal the underlying dynamics of edge retraction. Capillarity drives mass to flow from the triple line towards the advancing side of the rim. The mass within the rim never leaves the rim, and the rim mass originates almost entirely as the material that has been swept up during retraction. The remaining portion of the rim volume is mass rejected from the valley. However, mass from the valley contributes only a few percent of the total rim volume (Chapter 7), and it can be neglected over short time scales.

For fully-faceted materials, it is often reported that there is no valley ahead of the rim (Chapter 7). However, an alternative way of thinking unifies the isotropic and anisotropic cases. Phase field simulations (Chapter 8) show that the valley width increases as the anisotropy strength increases (as long as there is a facet parallel to the substrate). In the limit of perfect anisotropy (Chapter 7), the valley width goes to infinity, so the bulk, flat film acts as the valley and thins over time. The continuum between isotropic and anisotropic materials thus becomes clear: there is always a valley, though its width can become as large as the entire film.

At early times, edge retraction is linear with time, and at late times, the retraction distance goes as time to the 2/5 power. However, for relevant time scales in engineering applications, edge retraction follows an intermediate scaling. This overall behavior is observed for both isotropic and anisotropic materials (Chapters 4 and 7). The linear scaling arises at early times because the rim becomes wider as it retracts, rather than growing taller. The driving force scales with rim height, so retraction proceeds at a constant rate. The 2/5 scaling regime arises from the rim growing in height and width commensurately. The driving force decreases with time, and retraction slows. The transition between linear and 2/5 retraction regimes depends only on the contact angle θ. The larger the contact angle, the earlier the 2/5 scaling sets in. It is possible that a power-law fit for edge retraction gives an exponent slightly less than 2/5 at late times, due to the flux from the valley (Chatper 7).

9.2 Film edge instabilities

There are five mechanisms of film break-up during dewetting: natural hole formation, pinch-off, the fingering instability, the Rayleigh instability, and the corner instability. Capillarity alone cannot explain natural hole formation [55], and it is therefore beyond the scope of this work. However, the remaining mechanisms, or collectively the "edge instabilities," can be explained with capillarity. Edge instabilities dominate dewetting morphologies. Once a hole has formed either artificially or naturally, the distribution of particles produced by dewetting is controlled by these four processes.

The pinch-off mechanism is intimately related to the valley shape. A narrow, deep valley will lead to pinch-off much faster than a broad, shallow valley (Chapter 8). In the limit of a valley which is as broad as the film its self, the pinch-off time becomes much larger than engineering timescales, and so it will not be observable unless the film is small in extent (Chapter 7). Relative to an isotropic film, anisotropic films can have deeper or shallower valleys; however, the usual case is that the top of the film corresponds with a stable facet orientation. In this case, anisotropy leads to broad valleys and increased times to pinch-off (Chapter 8). After pinch-off, the remaining strips of material (which may be straight or curved) break up by a Rayleigh instability (the curved case is discussed in Chapter 3).

The fingering instability in isotropic materials is driven by the divergent retraction instability (defined in Chapter 5). The characteristic wavelength of the fingering instability is much larger than for a Rayleigh instability (Chapter 3), and the distribution of possible wavelengths is much larger. Therefore, it is possible to distinguish between Rayleigh and fingering instabilities by the final particle spacing. However, they often work cooperatively, as the finger spacing determines the particle spacing normal to the retraction direction, while the Rayleigh instability breaks up the fingers themselves and sets the particle spacing parallel to the retraction direction.

Patterning the initial edge morphology to achieve particular finger spacings should be quite easy because of the wide range of perturbation wavelengths that will grow. This is in stark contrast to break-up via a Rayleigh instability, which only tolerates a very narrow range of patterned wavelengths centered around $2\sqrt{2}\pi r$, where r is the radius of rim curvature, because the growth rates of perturbations far from this value are near zero, or negative (Chapter 3).

The corner instability (Chapter 6), which is common in strongly-anisotropic films, is driven by the changing arc-length instability (defined in Chapter 5). It is responsible for the "star-like," "dendritic," or "x"-shaped morphologies routinely observed following anisotropic dewetting. As long as film edges are composed of straight facets, the instability is unavoidable. Each corner or jog on the film edge with negative in-plane curvature is susceptible to it, which explains the dendritic morphology: the instability occurs at all of these points, not just at corners. The mechanism is not restricted to anisotropic films, so corner instabilities are possible for isotropic films too, if a sharp corner is patterned into the film. However, the corner will blunt over time in the absence of anisotropy.

9.3 Outlook

In this work, many of the features of dewetting have been explained. However, questions remain to complete the picture of dewetting dynamics.

It is not clear why some systems undergo a fingering instability and other systems undergo pinch-off. However, it is possible to speculate. At the time of publication, there

are no studies of dewetting on isotropic materials whose kinetics are dominated by surface diffusion (polymer, liquid, and glass films follow different kinetics), so it is impossible to know whether isotropic films undergo pinch-off or a fingering instability first (though phase field simulations in Chapter 8 suggest both cases are possible, depending on the initial perturbation size). Fingering instabilities are only reported experimentally for polycrystalline films or strongly anisotropic single-crystal films. The grain structure of polycrystalline films builds in variations in rim height and mobility from the onset of dewetting, which could act as a large-amplitude perturbation that seeds the fingering instability. The finger periodicity seems to match the grain size, suggesting that the grains act as the seed perturbation [53, 38]. Film stress can cause grain pop-up or subsidence, and variation in height could also vary the retraction rate from grain to grain (see [4]). The stability analysis in Chapter 5 suggests that all but the shortest wavelengths will grow, so it is plausible that the fingering wavelength matches the grain size. However, a connection between finger spacing and grain size has not been definitively shown.

In the case of strongly-anisotropic films, the instability on straight film edges may not be a fingering instability. A periodic corner instability on an edge which is straight (on average) gives the appearance of a fingering instability, but is mechanistically unrelated. Ye *et al.* show that for strongly-anisotropic films, most orientations decompose into kinetically-stable facets [89], leading to a "zig-zag" morphology. A corner instability is expected, based on the mechanism identified in Chapter 6, at each negatively-curved jog along the edge. Furthermore, Leroy *et al.* show that the "fingering" instability occurs in silicon (which is strongly anisotropic) only on unstable edges which undergo the faceting instability [47]. Therefore, the periodicity of the decomposition into kinetically-stable facets determines the periodic corner instability wavelength. The wavelength of the faceting instability is discussed in Chapter 8. If the edge instability on strongly-anisotropic films is in fact a periodic corner instability, then the faceting instability should be investigated to find ways of controlling the spacing between fingers.

In summary, it is possible that the only "true" fingering instability occurs on polycrystalline films, where the grain structure sets the fingering wavelength. In the absence of a large initial perturbation, pinch-off is likely to be the faster mechanism. However, it remains to be

shown how large (or small) the perturbation must be for fingering to overtake pinch-off. On strongly-anisotropic films, the instability mechanism may instead be a faceting instability, followed by corner instabilities.

Bibliography

[1] Abbarchi, M., Naffouti, M., Vial, B., Benkouider, A., Lermusiaux, L., Favre, L., Ronda, A., Bidault, S., Berbezier, I., and Bonod, N. Wafer scale formation of monocrystalline silicon-based mie resonators via silicon-on-insulator dewetting. *ACS Nano 8*, 11 (2014), 11181–11190. PMID: 25365786.

[2] Agrawal, P. M., Rice, B. M., and Thompson, D. L. Predicting trends in rate parameters for self-diffusion on fcc metal surfaces. *Surface Science 515*, 1 (2002), 21–35.

[3] Armelao, L., Barreca, D., Bottaro, G., Gasparotto, A., Gross, S., Maragno, C., and Tondello, E. Recent trends on nanocomposites based on Cu, Ag and Au clusters: A closer look. *Coordination Chemistry Reviews 250*, 11-12 (2006), 1294–1314.

[4] Atiya, G., Chatain, D., Mikhelashvili, V., Eisenstein, G., and Kaplan, W. D. The role of abnormal grain growth on solid-state dewetting kinetics. *Acta materialia 81* (2014), 304–314.

[5] Bergamaschini, R., Salvalaglio, M., and Montalenti, F. The merging of micropillars during annealing. *In preparation* (2015).

[6] Brandon, R., and Bradshaw, F. J. The mobility of the surface atoms of copper and silver evaporated deposits. *Technical Report 66095 Royal Aircraft Establishment* (1966).

[7] Burhanudin, Z. A., Nuryadi, R., Ishikawa, Y., Tabe, M., and Ono, Y. Thermally-induced formation of si wire array on an ultrathin (111) silicon-on-insulator substrate. *Applied Physics Letters 87*, 12 (2005), 121905.

[8] Bussmann, E., Cheynis, F., Leroy, F., Müller, P., and Pierre-Louis, O. Dynamics of solid thin-film dewetting in the silicon-on-insulator system. *New Journal of Physics 13*, 4 (2011), 043017.

[9] Cahn, J. Thermodynamics of solid and fluid surfaces. *Interfacial Segregation ASM Seminar Series, ASM international* (1978), 3–23.

[10] Cahn, J., and Carter, W. Crystal shapes and phase equilibria: A common mathematical basis. In *Metallurgical and Materials Transactions a-Physical Metallurgy and Materials Science* (1996), pp. 1431–1440.

[11] Cahn, J., Elliott, C. M., and Novick-Cohen, A. The Cahn–Hilliard equation with a concentration dependent mobility: motion by minus the Laplacian of the mean curvature. *European Journal of Applied Mathematics 7*, 03 (1996).

[12] Cahn, J., and HANDWERKER, C. Equilibrium Geometries of Anisotropic Surfaces and Interfaces. In *Materials Science and Engineering a-Structural Materials Properties Microstructure and Processing* (1993), pp. 83–95.

[13] Cahn, J., and Hoffman, D. A vector thermodlnamics for anisotropic surfaces—II. Curved and faceted surfaces. *Acta Metallurgica 22*, 10 (1974), 1205–1214.

[14] Carter, W. The Forces and Behavior of Fluids Constrained by Solids. *Acta Metallurgica 36*, 8 (1988), 2283–2292.

[15] Carter, W., Roosen, A., Cahn, J., and Taylor, J. Shape evolution by surface diffusion and surface attachment limited kinetics on completely faceted surfaces. *Acta metallurgica et materialia 43*, 12 (1995), 4309–4323.

[16] Chatain, D., and Galy, D. Interfaces between Pb grains and Cu surfaces. *Journal of Materials Science 41*, 23 (2006), 7769–7774.

[17] Chen, J.-H., Lei, T.-F., Landheer, D., Wu, X., Liu, J., and Chao, T.-S. Si nanocrystal memory devices self-assembled by in situ rapid thermal annealing of ultra-thin a-si on sio2. *Electrochemical and Solid-State Letters 10*, 10 (2007), H302–H304.

[18] Cheynis, F., Bussmann, E., Leroy, F., Passanante, T., and Müller, P. Dewetting dynamics of silicon-on-insulator thin films. *Physical Review B 84*, 24 (2011), 245439.

[19] Chhowalla, M., Teo, K. B. K., Ducati, C., Rupesinghe, N. L., Amaratunga, G. A. J., Ferrari, A. C., Roy, D., Robertson, J., and Milne, W. I. Growth process conditions of vertically aligned carbon nanotubes using plasma enhanced chemical vapor deposition. *Journal of Applied Physics 90*, 10 (2001), 5308.

[20] Choi, W. K., Liew, T. H., Chew, H. G., Zheng, F., Thompson, C. V., Wang, Y., Hong, M. H., Wang, X. D., Li, L., and Yun, J. A Combined Top-Down and Bottom-Up Approach for Precise Placement of Metal Nanoparticles on Silicon. *Small 4*, 3 (2008), 330–333.

[21] Colli, A., Fasoli, A., Beecher, P., Servati, P., Pisana, S., Fu, Y., Flewitt, A., Milne, W., Robertson, J., Ducati, C., et al. Thermal and chemical vapor deposition of si nanowires: Shape control, dispersion, and electrical properties. *Journal of Applied Physics 102*, 3 (2007), 034302.

[22] Dahmen, U., Hagège, S., Faudot, F., Radetic, T., and Johnson, E. Observations of interface premelting at grain-boundary precipitates of Pb in Al. *Philosophical Magazine 84*, 25-26 (2004), 2651–2662.

[23] Danielson, D. T. Anisotropic Dewetting in Ultra-Thin Single-Crystal Silicon-on-Insulator Films. *Ph.D. Thesis, MIT* (2008), 1–156.

[24] Danielson, D. T., Sparacin, D. K., Michel, J., and Kimerling, L. C. Surface-energy-driven dewetting theory of silicon-on-insulator agglomeration. *Journal of Applied Physics 100*, 8 (2006), 083507.

[25] de Mongeot, F. B., Zhu, W., Molle, A., Buzio, R., Boragno, C., Valbusa, U., Wang, E., and Zhang, Z. Nanocrystal formation and faceting instability in al (110) homoepitaxy: true upward adatom diffusion at step edges and island corners. *Physical review letters 91*, 1 (2003), 016102.

[26] Di Carlo, A., Gurtin, M. E., and Podio-Guidugli, P. A regularized equation for anisotropic motion-by-curvature. *SIAM Journal of Applied Mathematics 52*, 4 (1992), 1111âĂŞ1119.

[27] Dornel, E., Barbé, J.-C., de Crécy, F., Lacolle, G., and Eymery, J. Surface diffusion dewetting of thin solid films: Numerical method and application to SiÃćÂĹÂŢ-SiO2. *Physical Review B 73*, 11 (2006).

[28] Dufay, M., and Pierre-Louis, O. Anisotropy and Coarsening in the Instability of Solid Dewetting Fronts. *Physical Review Letters 106*, 10 (2011).

[29] Fan, Y., Nuryadi, R., Burhanudin, Z. A., and Tabe, M. Thermal Agglomeration of Ultrathin Silicon-on-Insulator Layers: Crystalline Orientation Dependence. *Japanese Journal of Applied Physics 47*, 3 (2008), 1461–1464.

[30] Giermann, A., and Thompson, C. Requirements for graphoepitaxial alignment through solid-state dewetting of au films. *Journal of Applied Physics 109*, 8 (2011), 083520.

[31] Giorgi, E. D. *Some remarks on gamma-convergence and least squares methods*, vol. 5. Birkhauser, Boston, 1991, ch. Chapter, p. 135âĂŤ142.

[32] HERRING, C. Some Theorems on the Free Energies of Crystal Surfaces. *Physical Review 82*, 1 (1951), 87–93.

[33] Herring, C. *Structure and Properties of Solid Surfaces*. The University of Chicago Press, Chicago, 1952.

[34] Hyun Kim, G., Zucker, R. V., Ye, J., Craig Carter, W., and Thompson, C. V. Quantitative analysis of anisotropic edge retraction by solid-state dewetting of thin single crystal films. *Journal of Applied Physics 113*, 4 (2013), 043512.

[35] Jacqmin, D. Contact-line dynamics of a diffuse fluid interface. *Journal of Fluid Mechanics 402* (2000), 57–88.

[36] Jiang, W., Bao, W., Thompson, C. V., and Srolovitz, D. J. Phase field approach for simulating solid-state dewetting problems. *Acta materialia 60*, 15 (2012), 5578–5592.

[37] Jiran, E., and Thompson, C. Capillary instabilities in thin films. *Journal of electronic materials 19*, 11 (1990), 1153–1160.

[38] Jiran, E., and Thompson, C. Capillary instabilities in thin, continuous films. *Thin Solid Films 208*, 1 (1992), 23–28.

[39] Johnson, E., Johansen, A., Hinderberger, S., Xiao, S., and Dahmen, U. Structure and morphology of nanosized lead inclusions in aluminum grain boundaries. *Interface Science 3*, 4 (1996), 279–288.

[40] Kan, W., and Wong, H. Fingering instability of a retracting solid film edge. *Journal of Applied Physics 97*, 4 (2005), 043515.

[41] Kaplan, W. D., Chatain, D., Wynblatt, P., and Carter, W. C. A review of wetting versus adsorption, complexions, and related phenomena: the rosetta stone of wetting. *Journal of Materials Science 48*, 17 (2013), 5681–5717.

[42] Karma, A., and Rappel, W.-J. Quantitative phase-field modeling of dendritic growth in two and three dimensions. *Physical review E 57*, 4 (1998), 4323.

[43] Klinger, L., Amram, D., and Rabkin, E. Kinetics of a retracting solid film edge: The case of high surface anisotropy. *Scripta Materialia 64*, 10 (2011), 962–965.

[44] Kobayashi, R. Modeling and numerical simulations of dendritic crystal growth. *Physica D: Nonlinear Phenomena 63*, 3 (1993), 410–423.

[45] Lee, J., and Aaronson, H. Influence of faceting upon the equilibrium shape of nuclei at grain boundaries–I. Two-dimensions. *Acta Metallurgica 23*, 7 (1975), 799–808.

[46] Lee, J. K., Aaronson, H., and Russell, K. On the equilibrium shape for a non-centro-symmetric γ-plot. *Surface Science 51*, 1 (1975), 302–304.

[47] Leroy, F., Cheynis, F., Passanante, T., and Müller, P. Dynamics, anisotropy, and stability of silicon-on-insulator dewetting fronts. *Physical Review B 85*, 19 (2012), 195414.

[48] Maiya, P., and Blakely, J. Surface self-diffusion and surface energy of nickel. *Journal of Applied Physics 38*, 2 (1967), 698–704.

[49] McCallum, M., Voorhees, P., Miksis, M., Davis, S., and Wong, H. Capillary instabilities in solid thin films: Lines. *Journal of Applied Physics 79*, 10 (1996), 7604–7611.

[50] Mizsei, J. Activating technology of SnO 2 layers by metal particles from ultrathin metal films. *Sensors and Actuators B: Chemical 16*, 1 (1993), 328–333.

[51] Modica, L., and Mortola, S. Il limite nella γ-convergenza di una famiglia di funzionali ellittici. *Boll. Un. Mat. Ital. A (5) 14*, 3 (1977), 526–529.

[52] Moore, K., Zhang, D., and Cantor, B. Solidification of pb particles embedded in al. *Acta Metallurgica et Materialia 38*, 7 (1990), 1327–1342.

[53] Muller, C. M., and Spolenak, R. Microstructure evolution during dewetting in thin Au films. *Acta materialia 58*, 18 (2010), 6035–6045.

[54] Mullins, W. Theory of thermal grooving. *Journal of Applied Physics 28*, 3 (1957), 333–339.

[55] Mullins, W. Flattening of a nearly plane solid surface due to capillarity. *Journal of Applied Physics 30*, 1 (1959), 77–83.

[56] Mullins, W., and Sekerka, R. F. Stability of a Planar Interface During Solidification of a Dilute Binary Alloy. *Journal of Applied Physics 35*, 2 (1964), 444.

[57] Nessim, G. D., Hart, A. J., Kim, J. S., Acquaviva, D., Oh, J., Morgan, C. D., Seita, M., Leib, J. S., and Thompson, C. V. Tuning of vertically-aligned carbon nanotube diameter and areal density through catalyst pre-treatment. *Nano Letters 8*, 11 (2008), 3587–3593.

[58] Nichols, F. A., and Mullins, W. Surface- (Interface-) and Volume-Diffusion Contributions to Morphological Changes Driven by Capillarity. *Transactions of the Metallurgical Society of AIME 233* (1965), 1840–1848.

[59] Nichols, F. A., and Mullins, W. Surface- (Interface-) and Volume-Diffusion Contributions to Morphological Changes Driven by Capillarity. *Transactions of the Metallurgical Society of AIME 233* (1965), 1840–1848.

[60] Nuryadi, R., Ishikawa, Y., and Tabe, M. Formation and ordering of self-assembled Si islands by ultrahigh vacuum annealing of ultrathin bonded silicon-on-insulator structure. *Applied surface science 159* (2000), 121–126.

[61] Pierre-Louis, O., Chame, A., and Saito, Y. Dewetting of Ultrathin Solid Films. *Physical Review Letters 103*, 19 (2009).

[62] Powers, J., and Glaeser, A. Orientation Effects on the HighÃćÂĂÂŘTemperature Morphological Evolution of Pore Channels in Sapphire. *Journal of the American Ceramic Society 83*, 9 (2000), 2297–2304.

[63] Rabkin, E., Amram, D., and Alster, E. Solid state dewetting and stress relaxation in a thin single crystalline Ni film on sapphire. *Acta materialia 74*, C (2014), 30–38.

[64] Randolph, S., Fowlkes, J., Melechko, A., Klein, K., Meyer III, H., Simpson, M., and Rack, P. Controlling thin film structure for the dewetting of catalyst nanoparticle arrays for subsequent carbon nanofiber growth. *Nanotechnology 18*, 46 (2007), 465304.

[65] Rath, S., Heilig, M., Port, H., and Wrachtrup, J. Periodic organic nanodot patterns for optical memory. *Nano letters 7*, 12 (2007), 3845–3848.

[66] Rätz, A., Ribalta, A., and Voigt, A. Surface evolution of elastically stressed films under deposition by a diffuse interface model. *Journal of Computational Physics 214*, 1 (2006), 187–208.

[67] Rayleigh, L. On the instability of jets. *Procedings of the London mathematical society 10* (1878), 4–13.

[68] Roosen, A., McCormack, R., and Carter, W. Wulffman: A tool for the calculation and display of crystal shapes. *Computational materials science 11*, 1 (1998), 16–26.

[69] Salvalaglio, M., Backofen, R., Bergamaschini, R., Montalenti, F., and Voigt, A. Faceting of equilibrium and metastable nanostructures: a phase-field model of surface diffusion tackling realistic shapes. *Submitted, Crystal Growth and Design* (2015).

[70] Schmidt, V., Wittemann, J. V., Senz, S., and Gösele, U. Silicon nanowires: a review on aspects of their growth and their electrical properties. *Advanced Materials 21*, 25-26 (2009), 2681–2702.

[71] Seo, S., Euaruksakul, C., Savage, D., Lagally, M., and Evans, P. Nanostructure formation in the initial roughening of a thin silicon sheet. *Physical Review B 81*, 4 (2010), 041302.

[72] Siem, E., and Johnson, E. Melting of embedded anisotropic particles: PbIn inclusions in Al. *Philosophical Magazine 85*, 12 (2005), 1273–1290.

[73] Siem, E. J., Carter, W. C., and Chatain, D. The equilibrium shape of anisotropic interfacial particles. *Philosophical Magazine 84*, 10 (2004), 991–1010.

[74] Srolovitz, D., and Safran, S. Capillary instabilities in thin films. I. Energetics. *Journal of Applied Physics 60*, 1 (1986), 247–254.

[75] Srolovitz, D., and Safran, S. Capillary instabilities in thin films. II. Kinetics. *Journal of Applied Physics 60*, 1 (1986), 255–260.

[76] Sutter, P., Ernst, W., Choi, Y., and Sutter, E. Mechanisms of thermally induced dewetting of ultrathin silicon-on-insulator. *Applied physics letters 88*, 14 (2006), 141924.

[77] Taylor, J. II–mean curvature and weighted mean curvature. *Acta metallurgica et materialia 40*, 7 (1992), 1475–1485.

[78] Thompson, C. V. Solid-State Dewetting of Thin Films. *Annual Review of Materials Research 42*, 1 (2012), 399–434.

[79] Torabi, S., Lowengrub, J., Voigt, A., and Wise, S. A new phase-field model for strongly anisotropic systems. *Proceedings of the Royal Society A: Mathematical, Physical and Engineering Sciences 465*, 2105 (2009), 1337–1359.

[80] Vey, S., and Voigt, A. Amdis: adaptive multidimensional simulations. *Computing and Visualization in Science 10*, 1 (2007), 57–67.

[81] Vitos, L., Ruban, A., Skriver, H. L., and Kollar, J. The surface energy of metals. *Surface Science 411*, 1 (1998), 186–202.

[82] Weissmuller, J. *Thermodynamics of nanocrystalline solids*. Kluwer Academic Publishers, New York, 2002.

[83] Winterbottom, W. Equilibrium shape of a small particle in contact with a foreign substrate. *Acta Metallurgica 15*, 2 (1967), 303–310.

[84] Wise, S., Kim, J., and Lowengrub, J. Solving the regularized, strongly anisotropic Cahn-Hilliard equation by an adaptive nonlinear multigrid method. *Journal of Computational Physics 226*, 1 (2007), 414–446.

[85] Wong, H., Voorhees, P., Miksis, M., and Davis, S. Periodic mass shedding of a retracting solid film step. *Acta materialia 48*, 8 (2000), 1719–1728.

[86] Wulff, G. *Zur frage der geschwindigkeit des wachstums und der auflösung der kristallflächen*, vol. 34. Zeitschrift fur Kristallographie, 1901.

[87] Yang, S., Cao, B., Kong, L., and Wang, Z. Template-directed dewetting of a gold membrane to fabricate highly sers-active substrates. *Journal of Materials Chemistry 21*, 36 (2011), 14031–14035.

[88] Ye, J., and Thompson, C. V. Regular pattern formation through the retraction and pinch-off of edges during solid-state dewetting of patterned single crystal films. *Physical Review B 82*, 19 (2010), 193408.

[89] Ye, J., and Thompson, C. V. Anisotropic edge retraction and hole growth during solid-state dewetting of single crystal nickel thin films. *Acta materialia* (2011).

[90] Ye, J., and Thompson, C. V. Templated Solid-State Dewetting to Controllably Produce Complex Patterns. *Advanced Materials 23*, 13 (2011), 1567–1571.

[91] Yue, P., Zhou, C., and Feng, J. J. Sharp-interface limit of the cahn–hilliard model for moving contact lines. *Journal of Fluid Mechanics 645* (2010), 279–294.

[92] Yun, J., Wang, R., Choi, W., Thong, J., Thompson, C., Zhu, M., Foo, Y., and Hong, M. Field emission from a large area of vertically-aligned carbon nanofibers with nanoscale tips and controlled spatial geometry. *Carbon 48*, 5 (2010), 1362–1368.

[93] Zhang, W., and Gladwell, I. Evolution of two-dimensional crystal morphologies by surface diffusion with anisotropic surface free energies. *Computational materials science 27*, 4 (2003), 461–470.

[94] Zucker, R. V., Chatain, D., Dahmen, U., Hagège, S., and Carter, W. C. New software tools for the calculation and display of isolated and attached interfacial-energy minimizing particle shapes. *Journal of Materials Science 47*, 24 (2012), 8290–8302.

[95] Zucker, R. V., Kim, G. H., Carter, W. C., and Thompson, C. V. The mechanism of corner instabilities in single-crystal thin films during dewetting. *In preparation* (2015).

[96] Zucker, R. V., Kim, G. H., Craig Carter, W., and Thompson, C. V. A model for solid-state dewetting of a fully-faceted thin film. *Comptes Rendus Physique 14*, 7 (2013), 564–577.